

**Development and application of helium-filled soap bubbles
For large-scale PIV experiments in aerodynamics**

Caridi, Giuseppe Carlo Alp

DOI

[10.4233/uuid:effc65f6-34df-4eac-8ad9-3fdb22a294dc](https://doi.org/10.4233/uuid:effc65f6-34df-4eac-8ad9-3fdb22a294dc)

Publication date

2018

Document Version

Final published version

Citation (APA)

Caridi, G. C. A. (2018). *Development and application of helium-filled soap bubbles: For large-scale PIV experiments in aerodynamics*. [Dissertation (TU Delft), Delft University of Technology]. <https://doi.org/10.4233/uuid:effc65f6-34df-4eac-8ad9-3fdb22a294dc>

Important note

To cite this publication, please use the final published version (if applicable).
Please check the document version above.

Copyright

Other than for strictly personal use, it is not permitted to download, forward or distribute the text or part of it, without the consent of the author(s) and/or copyright holder(s), unless the work is under an open content license such as Creative Commons.

Takedown policy

Please contact us and provide details if you believe this document breaches copyrights.
We will remove access to the work immediately and investigate your claim.

**DEVELOPMENT AND APPLICATION OF
HELIUM-FILLED SOAP BUBBLES**

For large-scale PIV experiments in aerodynamics

DEVELOPMENT AND APPLICATION OF HELIUM-FILLED SOAP BUBBLES

For large-scale PIV experiments in aerodynamics

Dissertation

for the purpose of obtaining the degree of doctor
at Delft University of Technology
by the authority of the Rector Magnificus prof.dr.ir. T.H.J.J. van der Hagen
chair of the Board for Doctorates
to be defended publicly on
Wednesday 14 March 2018 at 12:30 o'clock

by

Giuseppe Carlo Alp CARIDI

Master of Science in Energy and Nuclear Engineering,
Polytechnic University of Turin, Italy,
Born in Nairobi, Kenya

This dissertation has been approved by the promotor and the copromotor.

Composition of the doctoral committee:

Rector Magnificus,	chairperson
Prof. dr. F. Scarano,	Delft University of Technology, promotor
Dr. A. Sciacchitano,	Delft University of Technology, copromotor

Independent members:

Prof. dr. ir. W.S.J. Uijtewaal,	Delft University of Technology
Prof. dr. ir. J.P.A.J. van Beeck,	von Karman Institute for Fluid Dynamics, Belgium
Prof. dr. T. Rösigen,	Eidgenössische Technische Hochschule Zürich, Switzerland
Dr. ir. C.J. Simão Ferreira,	Delft University of Technology
U. Dierksheide, M.Sc.	LaVision GmbH, Germany
Prof. dr. S. Hickel,	Delft University of Technology, reserve member



Keywords: HFSB, air-flow seeding, large-scale PIV, Tomo-PIV

Printed by: Rijnja Repro Delft

Front & Back: Cover picture by G.C.A.

Copyright © 2018 by G.C.A. Caridi

ISBN: 978-94-6366-015-0

An electronic version of this dissertation is available at

<http://repository.tudelft.nl/>.

Digital data plotted is available at

<http://doi.org/10.4121/uuid:00da52c3-9536-436f-811d-e9b42ac83073>

*Don't ever over-analyse your results.
Don't ever try to find your own secret or the one which you admire.
One does not try to catch soap bubbles.
One enjoys them in flight and is grateful for their fluid existence*

Ernst Haas

SUMMARY

A new type of tracer is making its entry in the scenario of wind-tunnel measurements: helium-filled soap bubbles (HFSB). The present work discusses the main fluid-dynamic and optical properties of HFSB to evaluate their use for quantitative measurements in aerodynamic experiments.

In the past three decades, particle image velocimetry (PIV) has become a standard measuring technique in experimental fluid mechanics. Advances in both hardware components and software analysis have allowed achieving many milestones in flow diagnostics, mainly time-resolved and instantaneous volumetric measurements. In particular, the extension to the third dimension in space, i.e. tomographic PIV and 3D particle tracking velocimetry (PTV), has been used to provide quantitative visualizations of the coherent structures occurring in various turbulent flows and have provided insight in the spatial organization of the turbulent motions at different scales. The extension of the aforementioned techniques towards industrial practice in wind tunnel testing requires the development of a more efficient approach in terms of scaling and versatility.

The present dissertation tackles the upscaling of PIV experiments towards industrial wind tunnels with the use of HFSB as tracing particles. The reasons and motivations behind this choice are addressed in the first chapter and followed by a description of the state-of-the-art of PIV. The second chapter aims at familiarising the reader with the working principles of PIV, which will be later recalled when presenting the advances towards large-scale experiments. Information on the mechanical behaviour of tracer particles and on the underlying physics are discussed in the third chapter, where also the case of HFSB is

examined for use during quantitative measurements in the low-speed flow regime.

The problem of seeding in wind tunnels is discussed in chapter 4, where a system for the injection of HFSB in a large wind tunnel is presented. Here, the relationship between HFSB production rate and the resulting spatial concentration and dynamic spatial range (DSR) are discussed. Specific experiments that examine the tracing fidelity of sub-millimetre HFSB tracers are presented in chapter 5. The behaviour of HFSB is compared to micro-size droplets, yielding a characteristic response time in the range of 10 μ s. The latter milestone opens up to the applicability of HFSB tracers for quantitative velocimetry in wind tunnel flows. In chapter 6, a specific case of interest is presented whereby HFSB tracers are used to measure the flow velocity within steady vortices such as those released at the tip of wings. A dedicated experiment shows that the neutrally or slightly buoyant HFSB return a rather homogeneous spatial concentration within the core of vortices, solving the long-standing issue encountered for small heavy tracers, such as fog droplets, that are systematically ejected from highly vortical regions.

An analysis of the light scattering by HFSB was conducted with theoretical and experimental approaches, as described in chapter 7. The light intensity scattered by the HFSB is characterised by two source points: the *glare points*. The overall scattered light appears to be 10^4 - 10^5 times more intense with respect to the oil-based micro-size droplets. This information is used to retrieve the maximum size of the measurement volume for a given light source.

Chapter 8 closes this dissertation presenting a survey of all the experiments that have been conducted during this PhD research. The scale of experiments varies from the more academic case of a circular cylinder up to the one of a ship model installed in one of the large industrial wind tunnels operated at the German-Dutch Wind Tunnels

laboratories (DNW), going through the visualization and quantification of large structures in the rotor region of a vertical axis wind turbine (VAWT).

SAMENVATTING

Een nieuw soort tracer doet zijn intrede in de wereld van windtunnel metingen: met helium gevulde zeepbellen (HFSB). Het werk in deze dissertatie bediscussieert de belangrijkste vloeistof-dynamische en optische eigenschappen van HFSB, om de potentie te onderzoeken van HFSB voor kwantitatieve metingen in het gebied van experimentele aerodynamica.

In de afgelopen drie decennia is particle image velocimetry (PIV) een standaard meettechniek geworden in het veld van experimentele stromingsmechanica. Ontwikkelingen van zowel hardwarecomponenten als software analysetechnieken hebben veel mijlpalen voor stromingsdiagnostiek mogelijk gemaakt, vooral voor instantane en tijdopgeloste volumetrische metingen. In het bijzonder, de uitbreiding naar de derde ruimtelijke dimensie, i.e. tomographic PIV en 3D particle tracking velocimetry (PTV), heeft kwantitatieve visualisatie van coherente structuren in verschillende turbulente stromingen mogelijk gemaakt, en heeft inzicht gegeven in de ruimtelijke organisatie van turbulente bewegingen op verschillende schalen. De uitbreiding van de hierboven genoemde technieken voor toepassingen in windtunnel metingen in de industrie vereist de ontwikkeling van een meer efficiënte benadering in termen van opschaling en versatiliteit.

Deze dissertatie pakt het probleem van opschaling van PIV experimenten naar industriële windtunnels aan, gebruik makend van HFSB als tracers. De motivatie voor deze keuze wordt in het eerste hoofdstuk behandeld, gevolgd door een beschrijving van de state-of-the-art van PIV. Het tweede hoofdstuk behandelt de werkingsprincipes van PIV, welke later worden gebruikt bij de presentatie van de stappen die gezet zijn naar grote-schaal experimenten. Achtergrondinformatie over het mechanische gedrag van tracer deeltjes en de onderliggende

fysica worden beschreven in het derde hoofdstuk, waarin ook het geval van HFSB wordt bekeken voor gebruik tijdens kwantitatieve metingen in het lage-snelheid stromingsregime.

Het probleem van generatie en distributie van tracers in windtunnels wordt bediscussieerd in hoofdstuk 4, waarin ook een systeem voor injectie van HFSB in een grote windtunnel gepresenteerd wordt. De relatie tussen de productiesnelheid van HFSB en de resulterende ruimtelijke concentratie en het dynamisch ruimtelijk bereik (DSR) wordt beschreven. Specifieke experimenten die de getrouwheid van sub-millimeter HFSB aan de luchtstroom onderzoeken worden gepresenteerd in hoofdstuk 5. Het gedrag van HFSB wordt vergeleken met druppels van micro-grootte, wat laat zien dat de HFSB een karakteristieke responstijdschaal in de range van 10 μ s hebben. Deze mijlpaal opent deuren voor toepasbaarheid van HFSB tracers voor kwantitatieve luchtstroommetingen in wind tunnel stromingen. In hoofdstuk 6 wordt een specifiek geval gepresenteerd, waar HFSB tracers gebruikt worden om de stromingssnelheid te meten binnen gestage wervelingen, zoals bijvoorbeeld de wervelingen die ontstaan aan de tip van een vleugel. Een specifiek experiment laat zien dat de HFSB met neutraal of licht drijfvermogen een ongeveer homogene ruimtelijke concentratie binnen de wervelkern aannemen, wat een oplossing is voor het reeds lang bestaande probleem van kleine en zware tracers (zoals mist druppels) die systematisch uit de kern gecentrifugeerd worden.

Een theoretische en experimentele analyse van de lichtverstrooiing door HFSB is uitgevoerd en beschreven in hoofdstuk 7. De intensiteit van de lichtverstrooiing door de HFSB wordt gekarakteriseerd door twee bronpunten: de schitterpunten. De globale lichtverstrooiing van HFSB blijkt 104-105 keer meer intens te zijn dan op olie gebaseerde druppels van micro-grootte. Met deze informatie wordt vervolgens de

maximale grootte van het meetvolume bepaald, voor een gegeven lichtbron.

Hoofdstuk 8 presenteert tot slot een overzicht van alle experimenten die uitgevoerd zijn tijdens dit PhD onderzoek. De schaal van de experimenten varieert van de meer academische case van een ronde cylinder tot aan de schaal van het model van een boot geïnstalleerd in een van de grote industriële windtunnels die beheerd worden door de Duits-Nederlandse windtunnel laboratoria (DNW), door de visualisatie en kwantificering van grote structuren in het rotorgebied van een verticale as windturbine (VAWT).

TABLE OF CONTENTS

SUMMARY	i
SAMENVATTING.....	v
1 INTRODUCTION.....	1
1.1 Background.....	1
1.2 PIV for large-scale applications.....	3
1.3 Seeding distribution in vortex flows.....	7
1.4 Motivation and objectives	9
1.5 Structure of the thesis	9
2 PARTICLE IMAGE VELOCIMETRY	11
2.1 Introduction	11
2.2 Working principle of PIV	11
2.3 Digital image recording.....	13
2.4 Illumination devices and techniques.....	14
2.4.1 Light source	14
2.4.2 Timing	15
2.4.3 Light Sheet.....	17
2.5 Requirements for seeding particles.....	17
2.6 Particle imaging.....	18
2.7 Image processing	20
2.8 Spatial resolution and dynamic range.....	21

2.9	Stereoscopic PIV	23
2.10	Tomographic PIV and 3D PTV	25
2.10.1	Working principle of tomographic PIV	25
2.10.2	Illumination	26
2.10.3	Imaging	27
2.10.4	Tomographic reconstruction and 3D vector fields	27
3	SEEDING PARTICLES	31
3.1	Introduction	31
3.2	Dynamic behaviour	32
3.2.1	Equation of motion	34
3.3	Characteristic time	36
3.4	Optical behaviour	37
3.5	Common seeding particles for aerodynamics	43
3.6	HFSB	43
3.6.1	Optical properties	45
4	HFSB SEEDING IN WIND TUNNELS	47
4.1	Introduction	47
4.2	Bubble generator system	48
4.3	Production regimes	50
4.4	Use of HFSB in wind tunnels: Production rate and DSR	52
4.5	HFSB injection in wind tunnels	59
5	DYNAMIC BEHAVIOUR OF HFSB	65
5.1	Introduction	65

5.2	Experimental apparatus and procedure.....	67
5.3	Velocity measurements.....	69
5.4	Aerodynamic behaviour of HFSB	71
6	HFSB FOR VORTEX CORE VELOCIMETRY	77
6.1	Introduction	77
6.2	Particle dynamics in a vortex.....	80
6.2.1	Pressure distribution on HFSB of finite size	85
6.3	Experimental apparatus and measurement procedure	87
6.4	Flow Seeding	90
6.5	Tracers visualization within leading-edge vortex.....	91
6.6	Velocity field in the vortex region.....	94
6.7	Discussion.....	98
7	OPTICAL CHARACTERIZATION OF HFSB	101
7.1	Introduction	101
7.2	Adrian’s formulation based on Mie theory.....	102
7.3	Ray-tracing model for HFSB.....	103
7.3.1	Numerical Assessment	107
7.4	Experimental approach.....	108
7.4.1	Experimental apparatus and setup	109
7.4.2	Image processing	110
7.4.3	Results and comparison with the ray-tracing.....	111
7.5	Implications on the measurement volume size in PIV experiments.....	114
8	USE OF HFSB IN LARGE-SCALE MEASUREMENTS	117

8.1	Introduction	117
8.2	Circular cylinder wake flow	118
8.2.1	Experimental setup	118
8.2.2	Instantaneous velocity field	121
8.3	Measurements in the rotor region of VAWT	123
8.3.1	Experimental setup	124
8.3.2	Results	129
8.4	Flow around a frigate.....	135
8.4.1	Experimental setup	135
8.4.2	Results	137
8.5	Lessons learned from experiments	139
9	CONCLUSIONS.....	143
9.1	Seeding system for large scale measurements.....	143
9.2	Dynamic behaviour of HFSB	144
9.3	Optical behaviour of HFSB	145
9.4	Perspectives	146
	REFERENCES	149
	ACKNOWLEDGEMENTS	158
	CURRICULUM VITAE.....	161
	LIST OF PUBLICATIONS	162

1

INTRODUCTION

1.1 Background

Aerodynamics research plays a fundamental role in the design and development of aircraft, ground vehicles, and wind turbines, among many other systems. The never-ending quest for higher efficiency has led to an ever increasing design complexity of innovative systems; as a consequence, in-depth understanding of the flow physics is required already in the design phase. In the last decades, the motto of the aerospace industry moved from “faster, higher, farther” to “cheaper, lighter, quieter (more silent)”. In other terms, the aerodynamic research is focusing on more complex and detailed phenomena that need more accurate predictions. Such progress in aerodynamics involves more wind tunnel testing and CFD calculations than theoretical analysis.

Given the scale of many industrial applications in the low-speed aerodynamic regimes, the flow is usually characterized by high Reynolds number (10^5 - 10^7). In flows pertaining to these values, numerical investigations involve high computational costs. The most common approach is to perform Reynolds Averaged Navier-Stokes simulations (RANS), which however depends on the chosen turbulence model. High-fidelity computations such as Large-Eddy or Direct Numerical Simulations (LES, DNS) involve less modelling, but they

become rapidly unaffordable when the system complexity and Reynolds number increase. For these reasons, wind tunnel testing still remains an important resource for aerodynamic investigations at large scales. In industrial wind tunnels, the most common measuring techniques involve direct force measurements by balance or surface pressure measurements through tiny orifices (Figure 1.1). Although the two techniques provide reliable measurements and are considered the state-of-the-art for wind tunnel measurements in industrial facilities, they provide little to no-information about the flow field around the models (e.g. flow separation, vortices, flow unsteadiness, turbulence).

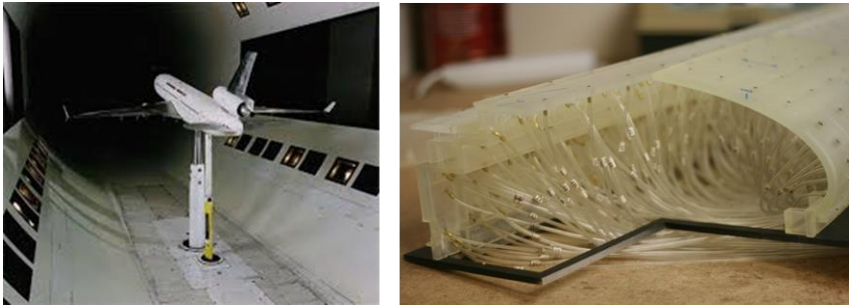


Figure 1.1 - Force balance measurement of an aircraft model (left). Taps and tubing for surface pressure distribution around the scaled model of an architectural building (right).

In the past decades, Particle Image Velocimetry (PIV) has become one of the most used measurement techniques for flow diagnostic in wind tunnels. This optical technique is used to visualize the velocity field in a two- or three-dimensional domain by measuring the displacement of small tracers that follow the fluid motion (Figure 1.2). The working principle of the PIV technique and the description of the main experimental components will be explained in chapter 2. Due to its advantages, PIV has the potential to enable in-depth understanding of the flow phenomena even for rather complex flow problems and at high

Reynolds numbers. However, the application of PIV for large-scale flow diagnostics remains still limited due to a number of problems which will be presented in the following section.

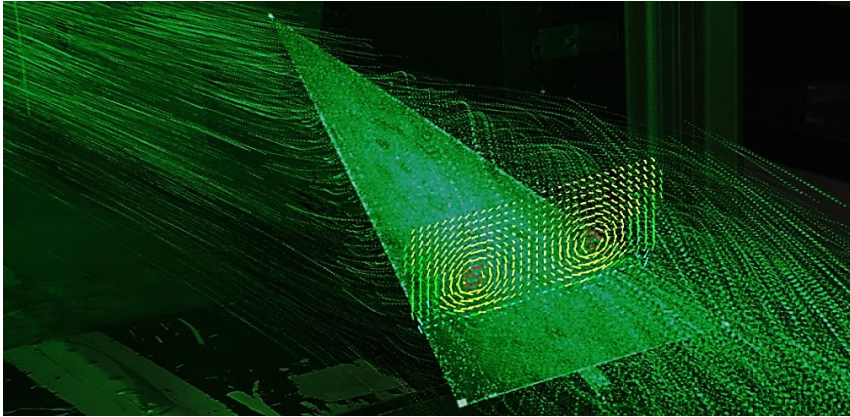


Figure 1.2 - Seeded airflow passing over a delta wing. Velocity vector field obtained from PIV measurement in a plane at 80% of the chord (experiment described in chapter 6).

1.2 PIV for large-scale applications

Aerodynamic investigation and testing for industrial research and development often require large-scale wind tunnel measurements, where the use of PIV is widely recognized as a challenge. The main factor limiting the upscaling of PIV to macroscopic dimensions is the detectability of the tracing particles, which are usually illuminated by pulses of laser light. The light intensity within the illuminated region is inversely proportional to the cross-sectional area of the latter. As a consequence, the increase of the measurement domain reduces the light scattered by the particles and collected by the camera sensors. For this

reason, PIV has been often limited to fields of view of $50 \times 50 \text{ cm}^2$ both for aeronautical and automotive applications (Kompenhans *et al.*, 2000; Beaudoin and Aider 2008). For larger measurement domains, e.g. domains exceeding the square meter, it is common to use a PIV procedure whereby several parts are measured separately and patched together to form a larger view of the velocity field (Carmer *et al.*, 2008, Tescione *et al.*, 2014, among others). The latter approach typically requires a careful and patient control of the system that scans the positions and it involves rather large measurement campaigns. An example of the above type of analysis is shown in Figure 1.3. As a result, this approach is often unpractical for industrial wind tunnel experiments due to the time constrains and high operational costs of the facilities.

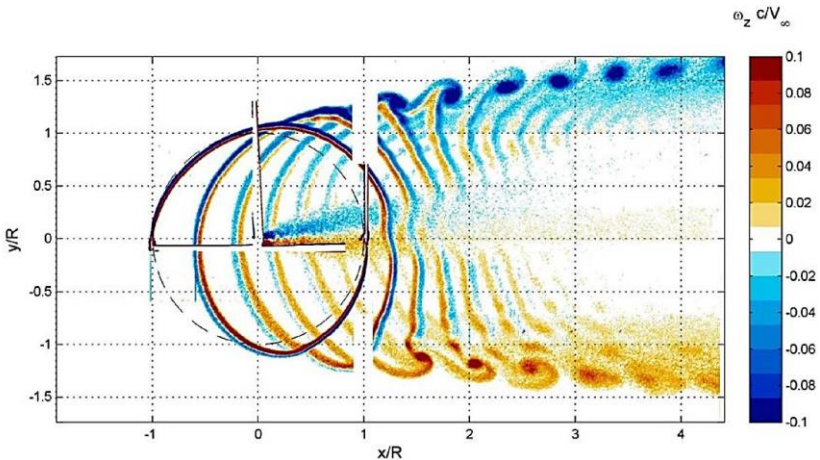


Figure 1.3 - Contour of normalized average vorticity in the wake of a vertical axis wind turbine with 1 m diameter. The result is obtained after patching 32 individual fields of views (Tescione *et al.*, 2014).

The problem is even more constraining for experiments requiring three-dimensional measurements. The imaging of the tracer particles in a tomographic PIV experiment is conducted at illumination intensity

typically an order of magnitude smaller than the one of planar PIV due to the expansion of the laser beam over a large cross section. In addition, a small optical aperture of the camera is needed to ensure focused particles along the whole measurement depth, thus reducing even more the amount of light collected by the sensor. For these reasons, three-dimensional measurements cannot be performed in large-scale domains with both conventional particles and light sources. The extension to volumetric measurements at a size relevant to industrial testing requires physical breakthroughs and exploration of alternative solutions.

From a literature survey, one can sample the evolution of 3D-PIV experiments in the past decade. The first measurement of Elsinga *et al.* (2006) was conducted over a volume of 13 cm^3 , a similar volume was achieved already with high-speed tomo-PIV by Schröder *et al.* (2008). Experiments in supersonic flows were conducted by Humble *et al.* (2009) in volumes of the order of 30 cm^3 . Violato *et al.* (2011) and Ghaemi and Scarano (2011) performed measurements in air flows over a volume not exceeding 20 cm^3 . Slightly larger measurement volumes were reported by Schröder *et al.* (2011) and Atkinson *et al.* (2011), however, not exceeding 50 cm^3 . To date, the largest investigated volume was reported by Fukuchi (2012) who measured over $16 \times 22 \times 8 \text{ cm}^3$ (approximately 2 litres), although results with an acceptable reconstruction signal-to-noise ratio were obtained up to a volume depth of 5 cm. In all of the above, laser illumination has been employed as the only available device able to produce high energy pulses of collimated and monochromatic light. In addition, LED illumination systems for 3D-PIV has recently been explored (Willert *et al.*, 2010).

A possible solution for large-scale PIV measurements is the use of tracer particles of larger diameter, which scatter more light and therefore can be visible even with lower illumination. However, when using liquid droplets, the tracing fidelity rapidly degrades by increasing

their size posing a fundamental limitation to this approach. Instead, when the particle tracers have a density approaching the one of the working fluid, the tracing fidelity can be maintained at larger tracer sizes (Melling 1997). For air flows, neutrally buoyant particles can be obtained by helium-filled soap bubbles (HFSB), for which the scattering light intensity is several orders of magnitude higher than micro-size droplets, as it will be shown in chapter 7.

Table 1.1 Size of the measurement domain obtained in PIV experiments.

Reference	Measurement Volume [cm ³]
Elsinga <i>et al.</i> (2006)	13
Schröder <i>et al.</i> (2008)	16
Humble <i>et al.</i> (2009)	28
Violato <i>et al.</i> (2011)	8
Ghaemi and Scarano (2011)	18
Schröder <i>et al.</i> (2011)	64
Atkinson <i>et al.</i> (2011)	35
Fukuchi (2012)	2800

In the past, HFSB seeding for PIV measurements was mainly applied in indoor air conditioning and ventilation. Some of the first examples of these applications are described in the work of Müller *et al.* (1997) and Zhao *et al.* (1999). More recently, Bosbach *et al.* (2009) realized a large-scale planar PIV experiment with a field-of-view up to 7 m² using HFSB to investigate the convective flow within full-scale aircraft cabin. Moreover, Kühn *et al.* (2011) performed a large-scale tomo-PIV measurement of the flow field in a convection cell of 75×45×16.5 cm³ (65 litres) using HFSB. One of the first applications of HFSB in industrial wind tunnels is described in the work of Machacek (2003) who has performed a 3D reconstruction of the path lines at low seeding concentration. However, the use of HFSB in wind tunnel experiments

was hampered by the lack of information about their tracing fidelity and the impossibility to obtain homogeneous seeding density with the current technology of HFSB generations. These questions are addressed in the present thesis, where the tracing accuracy of HFSB is investigated in details. Moreover, the fundamental principles of HFSB seeding in wind tunnels are discussed and possible techniques to increase seeding concentration are presented.

The present thesis includes three aerodynamic applications: the first one is the wake of a circular cylinder at moderate Reynolds number. The second application is the analysis of flow developing over the landing deck of a frigate at $Re = 8 \times 10^4$. Finally, an experiment is conducted that characterizes a fully three-dimensional flow developing around a horizontal axis wind turbine (VAWT) at $Re = 1.7 \times 10^5$, based on chord length and the tangential velocity of the blades. The flow regime is characterised by vortices periodically emanating from the blade tip.

1.3 Seeding distribution in vortex flows

The analysis of the flow features in aerodynamics often involves the study of vortices released or interacting with the model. PIV has been widely used to study vortex dominated flows due to its ability to determine the velocity and vorticity distribution in a cross-section of the vortex. Moreover, being non-intrusive (Raffel *et al.*, 2007; Westerweel *et al.*, 2013) PIV is well suited for the study of vortices emanating from rotating blades.

In many PIV measurements conducted in vortical flows, such as the wakes of rotors, delta wings, and jet flows, the systematic effect of a drifting (centrifugal) force is observed leading to a pronounced lack of tracers in the core of a vortex, as it is shown in Figure 1.4. In particular,

Figure 1.4-a shows a raw image of the experiment of Hong *et al.* (2014) conducted in the wake of a real wind turbine (2.5 MW) in a field of view of $36 \times 36 \text{ m}^2$ using natural snowfall as seeding. The behaviour of the tracers, in this case, leads to a quick depletion of particles in the vortex core.

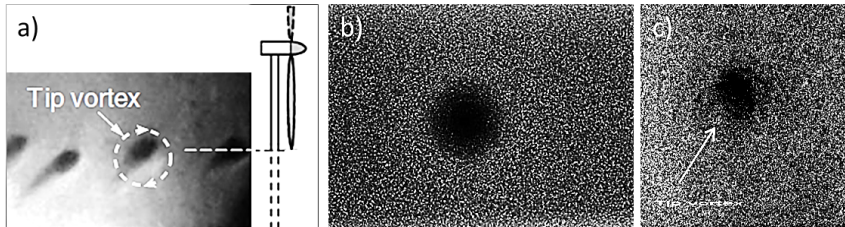


Figure 1.4 - The distribution of seed particles in the vortex core: a) Hong *et al.*, 2014; b) Stanislas *et al.*, 2003; c) Raffel *et al.*, 2004.

The second example (Figure 1.4-b) is a well-known case often reported in literature (1st international PIV Challenge, Stanislas *et al.* 2003). The latter cases and the one shown in Figure 1.4-c (Raffel *et al.*, 2004) are all related to vortices produced at the tip of airfoil: a) wind turbine blade; b) aircraft wing; c) helicopter rotor. In these examples, conventional micro-droplets are used and are ejected from the core region.

The use of smaller particles can mitigate the problem of the radial drift. However, the amount of light scattered, and consequently the detectability, rapidly decays by decreasing the particle diameter (Adrian and Yao, 1985; Lecuona *et al.*, 2002). Another solution to increase the seeding concentration in the vortex core is the use of neutrally buoyant particles. This condition can be easily satisfied for water flows, but in air flows, the only tracers that approach neutral buoyancy are the HFSB. Even if this topic is documented in the literature, the application of HFSB in vortical flows in wind tunnels is still missing.

1.4 Motivation and objectives

This thesis recognizes the potential of HFSB for large-scale measurements in wind tunnels. However, the use of these relatively new tracers for aerodynamic applications poses several open questions:

- What is the capability of HFSB to follow the flow? And how can this property be quantified by experiments?
- What is the optical-scattering behaviour of HFSB? And what is the extent of the measurement volume that can be obtained with the use of HFSB and conventional light sources?
- How can HFSB tracers respond to open problems encountered with conventional tracers such as particles depletion from regions with high centrifugal forces?
- What is the performance of PIV systems operating at large scale, making use of HFSB? How can someone estimate dynamic spatial range and dynamic velocity range for these experiments?

The following chapters address all of the above questions, with a final demonstration of the use of HFSB in an industrial (large-scale) wind tunnel.

1.5 Structure of the thesis

The initial part of the thesis provides a summary of the thesis scope describing the reasons and the motivations of using HFSB as tracing particles.

Chapter 2 summarizes the working principles of PIV measurement technique. Those principles will be recalled in the following chapters when the developments of large-scale PIV measurements are presented.

Chapter 3 describes the mechanical and optical behaviour of the seeding particles for PIV measurements.

Chapter 4 focuses on the development of PIV seeding for wind tunnel experiments with HFSB. Here, the relationship between HFSB production rate, resulting concentration and dynamic spatial range (DSR) is discussed. The chapter includes the description of a new system for the injection of HFSB in a large wind tunnel.

Chapter 5 presents the experimental procedure to quantify the flow-tracing capability of HFSB. The behaviour of HFSB is compared with micro-size droplets, yielding a characteristic response time scale in the range of 10 μ s. This is a milestone which opens the applicability of HFSB tracers for quantitative velocimetry in wind tunnel flows.

In chapter 6, a specific application of HFSB in vortical flows is presented. A dedicated experiment shows that the neutrally or slightly buoyant HFSB returns a rather homogeneous spatial concentration within the core of vortices, solving the long-standing issue encountered for small heavy tracers systematically ejected from the core region.

Chapter 7 analyses the light scattered by HFSB with theoretical and experimental approaches. The overall scattered light appears to be 10^4 - 10^5 times more intense with respect to the oil-based micro-size droplets. This information is used to retrieve the maximum size of the measurement volume for a given light source.

Chapter 8 describes applications realised using HFSB for tomo-PIV experiments in large-scale wind-tunnels

Chapter 9 summarizes the conclusion of the thesis and provides a short highlight on current trends and perspectives for future investigation and developments.

2

PARTICLE IMAGE VELOCIMETRY

2.1 Introduction

In this chapter, the main features of particle image velocimetry (PIV) are presented. First, the working principle of the technique is discussed including the description of the main experimental subsystems. Then, the determination of the velocity field from the image acquisition is illustrated. The discussion on the technique is finally extended to three-dimensional measurements with the description of tomographic PIV.

2.2 Working principle of PIV

Particle image velocimetry is an optical flow measurement technique based on the evaluation of the displacement of tracing particles between subsequent image frames recorded by an imaging system (Adrian, 1991; Raffel *et al.*, 2013). For purposes of introduction, in this section the working principle of a planar PIV system is presented. Figure 2.1 illustrates a typical PIV setup in a wind tunnel. Small seeding particles are inserted in the flow and transported by the fluid. It is assumed that the seeding particles faithfully follow the motion of the local fluid elements. A thin light sheet, generated by a pulsed light source, illuminates the seeding particles in two consecutive instants, t and t' .

The time delay between the light pulses depends on the flow velocity and magnification at imaging. The light scattered by the particles is recorded by the camera in two subsequent image frames. The digital recording system, composed usually by cameras with CCD or CMOS sensor, must have optical access to the measurement plane inside the test section. The images are divided into interrogation windows (IW) in which the light intensity distribution is used to detect and localize the particles. The tracers appear as white peaks over a black background. Thereafter, a spatial correlation analysis is applied to each interrogation window in order to determine the average in-plane displacement of the particle ensemble. The particles velocity is obtained by dividing the particles displacement by the time separation between the recordings and the optical magnification factor.

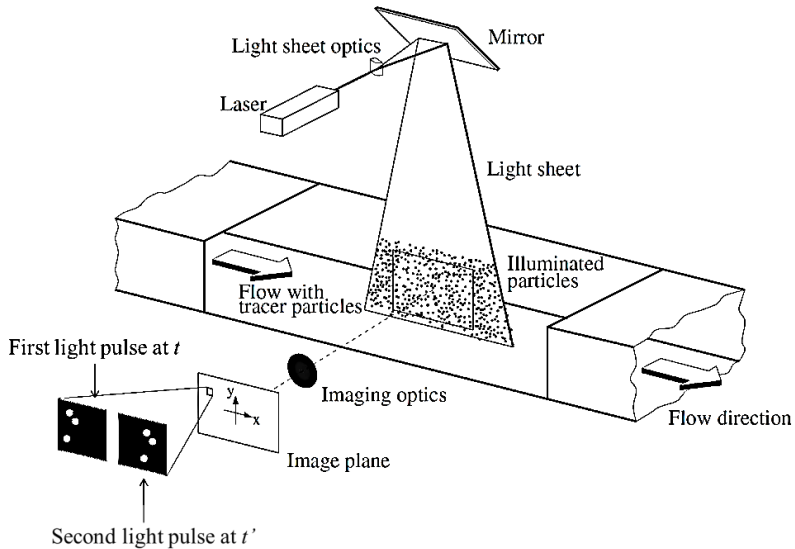


Figure 2.1 - Setup of 2D PIV setup in a wind tunnel (Raffel *et al.*, 2013).

The possibility to simultaneously measure instantaneous velocity vectors at many locations (as many as the number of IW) is one of the main features that promoted the use of PIV in many applications from microfluidics to the aerospace sector (Raffel *et al.*, 2013). The resulting vector field has typically 10^3 - 10^5 grid points and it can be used to compute quantities based on the velocity gradient as vorticity and rate of strain. The resolution of the measurement allows the detection of spatial coherent structures even in unsteady flows. As a result, PIV provides a powerful approach for turbulence interpretation in terms of structural elements (Adrian *et al.*, 2000). As it is shown in Figure 2.1, the technique does not employ probes inside the test section and, for this reason; PIV is considered a non-intrusive technique. The seeding particles are usually introduced in the flow upstream the test section. Considering relative small seeding concentration, typically 1-5 particles/mm³, and size of the tracers, 1-5 μm (Raffel *et al.*, 2013), it can be demonstrated that the presence of the particles does not affect the flow behaviour.

2.3 Digital image recording

PIV experiments typically involve digital image recording systems. The most common ones are the charge coupled devices, or CCD. The rapid development of camera technology has brought to the development of CMOS (Complementary Metal Oxide Semiconductor) sensors with an improved signal-to-noise ratio and resolution. Since more than a decade, the latter are more and more frequently used for high-speed recordings. The sensors are formed by a rectangular array of photosensitive elements called pixels. The latter convert the incoming light (photons) into electric charge, which is then read and converted into a digital signal. Pixel size can vary approximately from $5 \times 5 \mu\text{m}^2$

(for CCD sensors) to $20 \times 20 \mu\text{m}^2$ (for CMOS sensors). The optically sensitive area can be only a fraction of the entire area of the pixel, due to the presence of other components like metal conductors or charge storing devices.

CCD sensors typically operate at a rate from few Hertz to 50 Hz. The acquisition rate is limited by the readout process with analog-to-digital conversion. On the other hand, CMOS sensors have a different readout architecture enabling imaging rates up to the order of 10 kHz.

2.4 Illumination devices and techniques

One of the main characteristics of the PIV technique is the planar illumination. In this section, the requirements for illuminating the measurement domain are discussed in terms of light source, the light sheet shape and the pulse timing.

2.4.1 Light source

PIV experiments require a source of illumination, which can be easily shaped into a thin light sheet for planar measurements, or into a well-defined volumetric domain for 3D measurements. Lasers are widely used because they produce a highly collimated light beam that can be easily transmitted with mirrors and shaped into a sheet with lenses. Another distinctive feature of lasers is their ability to emit light within a short pulse and a narrow wavelength range. Most PIV lasers operate around the green light (528 and 532 nm).

Semiconductor lasers are the most used in PIV experiments. The Nd:YAG (neodymium-doped yttrium aluminium garnet; $\text{Nd:Y}_3\text{Al}_5\text{O}_{12}$) or Nd:YLF (Neodymium-doped yttrium lithium fluoride; Nd:LiYF_4) being the most popular. The reader can refer to Raffel *et al.* (2013) for a

comprehensive description of these devices. For the purpose of designing PIV experiments, only some considerations are presented in this section. Flashlamp pumped Nd:YAG lasers can provide high-energy pulses (50 to 500 mJ) at typical rate of 10 Hz. Instead, diode-pumped Nd:YLF lasers offer a good level of energy (10 to 50 mJ) at high-repetition rate (1 to 10 kHz).

2.4.2 *Timing*

The illumination is characterized by the interval of time between the pulses, $\Delta t = t' - t$ (pulse separation), and the duration of the light pulses δt (pulse width). The first determines the displacement of the particles between two successive images of a pair and it is chosen accordingly to the flow condition and the magnification of the imaging system. Typically, Δt is selected in such a way that a particle image displacement of about 10 pixels occurs in the free-stream. The tracer, for a given velocity and magnification, can be recorded as a streaks or a sharp dot depending on the δt . Usually, the pulse width must be short enough to “freeze” the motion of the particles, so that they are imaged as dots. The pulse width, for a flash lamp pumped Nd:YAG laser is of the order of ten nanoseconds, whereas the pulse of diode-pumped Nd:YLF lasers can vary between 70 and 150 ns.

In PIV experiments, the laser illumination has to be synchronized with the camera exposures. The timing arrangement of the recording system is limited by the performance of the components. The limitations are mainly ascribed to the type and architecture of digital sensor and to the repetition rates of both camera and light source. This section will consider only two examples of timing schemas, in particular, the ones applied during the experiments in the present research. The reader is referred to Raffel *et al.* (2013) for a broader discussion on different timing modes. Figure 2.2 shows two typical

timing diagrams for a PIV system. The *dual-frame* configuration, or *frame straddling*, represents the most used recording arrangement in PIV experiments. The timing system triggers the recording of a frame pair with the camera. At the same time, two light pulses are generated so that the first occurs in the first frame and the second in the consecutive frame. The recording period of the second frame (~ 33 ms) is usually much longer than the first frame. The minimum time interval between the first and second frame is usually of the order of $1 \mu\text{s}$. The data acquired during the first frame is transferred to a dedicated buffer memory (shift register), during the second exposure.

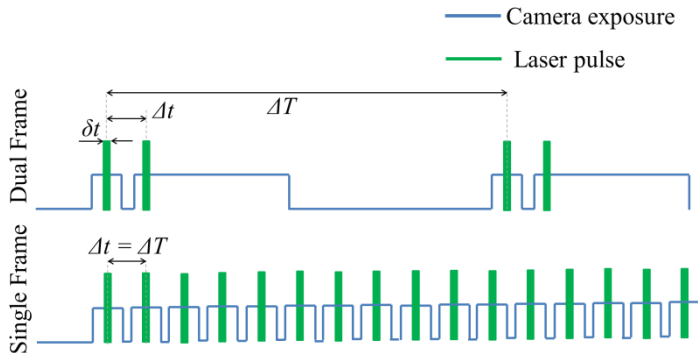


Figure 2.2 - Timing diagram for laser and cameras in PIV experiments.

The *single-frame* mode, or *continuous mode*, is typically used to acquire data for time-resolved measurements thanks to the periodic exposure cycles. In experiments where the velocity attains values between 10 and 100 m/s the continuous mode is only possible using CMOS sensor and diode-pumped lasers that operate at frequency of several kilohertz.

2.4.3 Light Sheet

A collimated monochromatic light beam is usually emitted by lasers with a diameter that ranges from 3 to 10 mm and it has to be shaped into a thin light sheet. A combination of cylindrical and spherical lenses is used to shape, to focus or to diverge the light beam. The thickness of the laser sheet in the region of interest, along with the laser pulse separation, has to be set in order to avoid excessive loss-of-pairs due to out-of-plane particles motions. The sheet thickness typically varies between 1 and 5 mm. A typical two-lens arrangement needed to form a light sheet is illustrated in Figure 2.3.

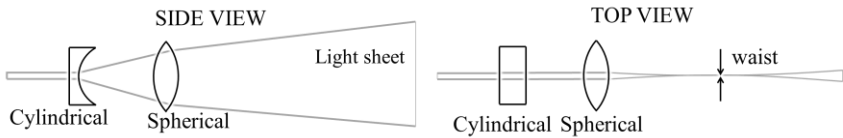


Figure 2.3 - Light sheet formation using a cylindrical and a spherical lens.

The point where the laser beam reaches the minimum diameter is called waist (top view of Figure 2.3). The properties of the light sheet in the waist region are discussed in more details in the literature (Durst and Stevenson, 1979, among others).

2.5 Requirements for seeding particles

The measurements conducted with particle image based velocimetry techniques, as PIV and PTV, determine the displacement of the particles. For this reason they are considered indirect measurements of the fluid velocity. Therefore, the accuracy of the measurement strongly depends on the properties of the particles. An ideal tracer travels with the same velocity as the surrounding fluid. Moreover, the particle is

detected by the imaging system as a bright isolated spot. In literature, it is usually mentioned that the choice of seeding particles for PIV experiments is always a compromise (Melling, 1997): the particles should be small enough to follow the fluid and large enough to scatter sufficient light to be detected. As a result, the suitability of a seeding tracer for a given experiment is based upon both mechanical and optical properties. A deeper discussion about these properties is addressed in chapter 3, where it is described how to analyse and quantify these properties.

2.6 Particle imaging

In this section the imaging of the seeding particles through a camera is described and the main parameters governing this process are introduced. A simplified illustration is given in Figure 2.4.

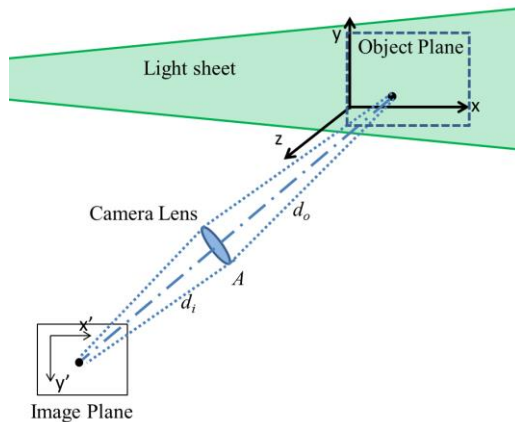


Figure 2.4 - Optical arrangement of the PIV system.

The magnification factor of an imaging system is defined as the ratio between the image-lens distance, d_i , and object-lens distance, d_o :

$$M = \frac{d_i}{d_o} \quad (2.1)$$

The focal length of the objective f is related to image and object distance by the thin lens equation:

$$\frac{1}{f} = \frac{1}{d_i} + \frac{1}{d_o} \quad (2.2)$$

The particle image size, d_τ , is determined by different contributions (Raffel *et al.*, 2013). The first is due to the geometrical projection from the object plane to the image plane, which depends on the magnification factor M : $d_{geom} = M d_p$. The second contribution considers the effect of diffraction due to the optical response of the lens, which generates an Airy pattern on the image plane. Considering the first zero of this distribution, the equivalent diameter associated to the diffraction can be defined as (Raffel *et al.*, 2013):

$$d_{diff} = 2.44 f_\# (1 + M) \lambda \quad (2.3)$$

$$d_\tau = (M^2 d_p^2 + d_{diff}^2)^{1/2} \quad (2.4)$$

Equation (2.4) applies under the hypothesis of in-focus particles when the depth of focus δZ is equal to or larger than the size of the illuminated volume along the viewing direction ΔZ . As indicated by Soft (1986) the depth of focus is given by:

$$\delta Z = 4.88 \left(\frac{1 + M}{M} \right)^2 f_\#^2 \lambda \quad (2.5)$$

where $f_\#$ is the numerical aperture of the camera (ratio between focal length and aperture). Equation (2.5) states that the depth of focus depends on the optical setup of the imaging system, namely the

magnification factor and camera aperture, and on the wavelength of the light λ .

2.7 Image processing

In this section, the mathematical background to retrieve two-dimensional vector fields from a two-frames recording is described. The recorded images are divided into small regions (usually based on a square kernel of say 32×32 pixels), named interrogation windows (IW). The dimensions of the latter determine the spatial resolution of the measurement. Each IW can be defined by a two-dimensional intensity function in two instants: $I_a(\mathbf{x})$ and $I_b(\mathbf{x})$, where $\mathbf{x} = (x, y)$ and the subscripts a and b indicate the time instants t and $t' = t + \Delta t$, respectively. The displacement of the ensemble of particles is indicated with $\Delta \mathbf{x}$ and it is computed via the statistical operator of *cross-correlation* R between I_a and I_b :

$$R(\Delta \mathbf{x}) = \int I_a(\mathbf{x}) I_b(\mathbf{x} + \Delta \mathbf{x}) d\mathbf{x} \quad (2.6)$$

The average particle image displacement in the interrogation window is the value $\Delta \mathbf{x}$ that maximizes R (Figure 2.5). Iterative approaches make use of interrogation window shift or deformation (Westerweel *et al.*, 1997; Scarano, 2001). The latter improves both robustness and accuracy of the displacement estimate, in particular in presence of an in-plane velocity gradient. One method to estimate the cross-correlation quality (signal strength) is by means of signal-to-noise ratio (SNR). The latter can be defined as the ratio between the primary peak and second tallest peak (Keane and Adrian, 1990). A measurement is considered

valid if the SNR is higher than a threshold level which is often assumed to be in the range between 1.2 and 1.5.

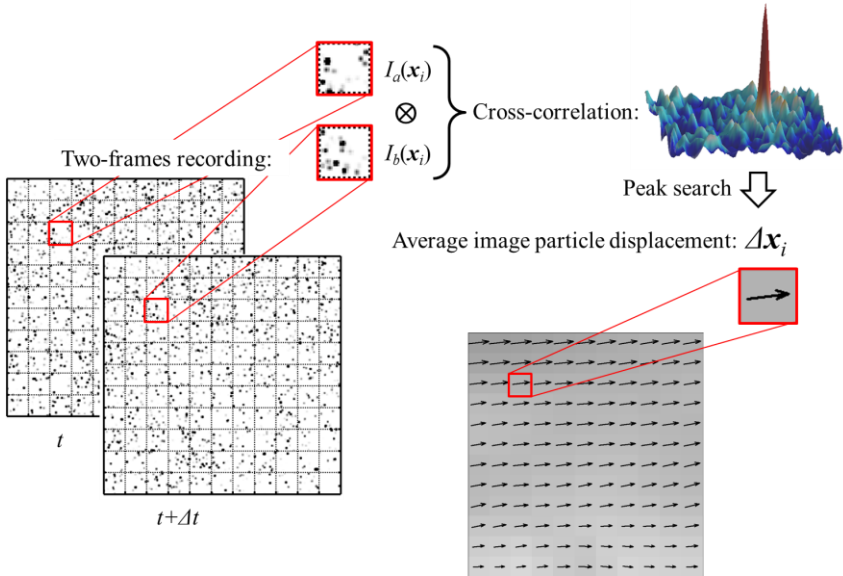


Figure 2.5 - Determination of the particle image displacement via cross-correlation.

2.8 Spatial resolution and dynamic range

The resulting velocity field is characterized by a finite number of vectors inside the field of view. The distance between adjacent independent vectors defines the spatial resolution of the PIV measurement. Following the approach of Adrian (1997), the *dynamic spatial range* DSR is defined as the ratio between the largest and the smallest resolvable spatial wavelength. Westerweel *et al.* (2013) have defined the dynamic spatial range as the ratio between the length of the

field of view L and the particle tracer displacement Δx . Further studies on the spatial resolution of PIV (Kähler *et al.*, 2012) suggest referring to the (linear) size of the interrogation window l_I instead of the particle tracer displacement. This is justified by the fact that the measurement of spatial resolution is directly connected with the size of the interrogation window, which becomes independent of the pulse separation time when multi-pass interrogation methods are used.

$$DSR = \frac{L}{l_I} \quad (2.7)$$

In simpler terms, the DSR can be seen as the number of independent vectors along a relevant direction of the field of view. As a result, the DSR indicates the ability of the PIV system to detect small-scale variations embedded in large-scale motions. For a given particle image number density N_I , defined as the number of particle images per interrogation window (Keane and Adrian, 1990), the interrogation window depends on the seeding concentration C and thickness of the laser sheet ΔZ as follows:

$$l_I = \sqrt{\frac{N_I}{C \Delta Z}} \quad (2.8)$$

Substituting equation (2.8) into equation (2.7) yields:

$$DSR = L \sqrt{\frac{C \Delta Z}{N_I}} \quad (2.9)$$

The linear size of the measurement domain (L) is typically determined by the geometry of the object immersed in the flow and by the specific flow features of interest. The particle image density N_I is chosen in

order to maximize the spatial resolution and the number of particle image pairs for the cross-correlation analysis. As a consequence, the concentration is the parameter most easily varied to achieve the desired *DSR*.

The ratio between the largest measurable displacement Δx_{max} and smallest displacement $\sigma_{\Delta x}$ defines the *dynamic velocity range DVR*:

$$DVR = \frac{\Delta x_{max}}{\sigma_{\Delta x}} \quad (2.10)$$

Typical values of *DVR* may range in the order of 100 or higher according to Hain and Kähler (2007). Stanislas *et al.* (2008) have reported that CMOS cameras used for high-speed measurements offer a lower *DVR* in relation to the weaker illumination and the lower image quality affect.

2.9 Stereoscopic PIV

Stereoscopic PIV reproduces the fundamental principle of human eye-sight: stereo vision. The use of two cameras to record simultaneously distinct views of the same region of interest is similar to the binocular vision, which allows to distinguish between near and far objects. Arroyo and Greated (1991) combined for the first time particle image velocimetry and stereoscopy; further developments of the technique are presented in the works of Willert (1997) and Prasad (2000). Stereoscopic PIV, or stereo PIV, provides three components of velocity vectors in a two-dimensional measurement domain. The use of two views of the illuminated plane gives sufficient information to extract the out-of-plane motion of the tracers, as it is shown in Figure 2.6. Moreover, stereo PIV definitively eliminates the perspective error

that can contaminate planar PIV measurements, if the camera objective (i.e. the line of sight) is not perfectly perpendicular to the light sheet.

Stereoscopic PIV requires an experimental setup similar to planar PIV, which makes its implementation straightforward. The main optical complexity of the setup is the alignment of the objective adapter of the off-axis cameras in order to fulfil the Scheimpflug condition (Prasad and Jensen, 1995). Figure 2.6 shows that lens-, object- and image-plane must intersect each other along a common line for the particle images to be properly focused over the entire illuminated plane. The angular displacement of the cameras makes the calibration procedure more important due to the change of magnification in the domain. The most accurate determination of the out-of-plane displacement (i.e. velocity) is accomplished when there is 90° between the two cameras. In case of restricted optical access, smaller angles can be used at the cost of a somewhat reduced accuracy.

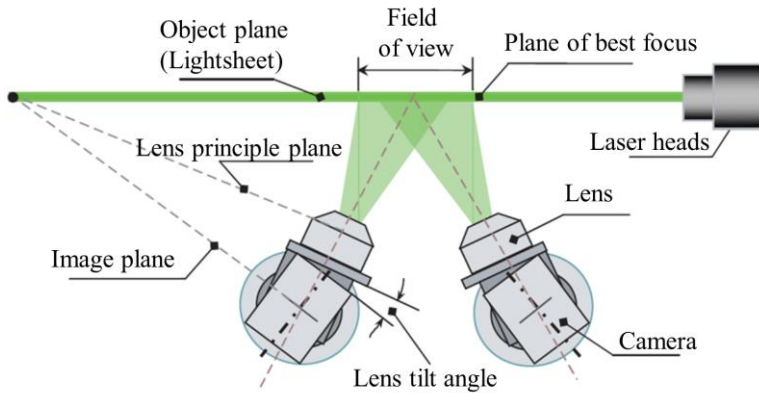


Figure 2.6 - Schematic of the optical configuration for stereoscopic PIV (Liu *et al.*, 2006).

2.10 Tomographic PIV and 3D PTV

Unsteady three-dimensional flow fields are of increasing importance in industrial applications as well as fundamental studies. The flow features exhibited in several 3D regimes usually involve the presence of vortices and their interaction, flow separation and complex streamline topology, which require three-dimensional measurements for a least ambiguous interpretation of the flow phenomena. Different approaches have been adopted to retrieve instantaneous 3D vector fields using particle-based techniques and an overview is presented in the work of Raffel *et al.* (2013). One of the most recent and advanced 3D techniques is tomographic PIV introduced by Elsinga *et al.* (2006). Another technique is the 3D particle tracking velocimetry, 3D-PTV (Maas *et al.*, 1993). The working principles of Tomo-PIV and 3D-PTV will be presented in this section. Both techniques have the same experimental setup in terms of illumination and imaging system, which will be discussed in the following section.

2.10.1 Working principle of tomographic PIV

The technique get its name from the tomographic reconstruction algorithm, which is a mathematical procedure used to reconstruct a three-dimensional field using a finite number of projections. In Tomo-PIV measurements, the projections consist of image frames acquired by multiple cameras with different viewing directions of the same measurement volume, as it is shown in Figure 2.7. The tomographic reconstruction algorithm will result in a three-dimensional light intensity distribution (objects) which is used for 3D spatial cross-correlation interrogation. The instantaneous three-component velocity vector field over the measurement volume is the final outcome.

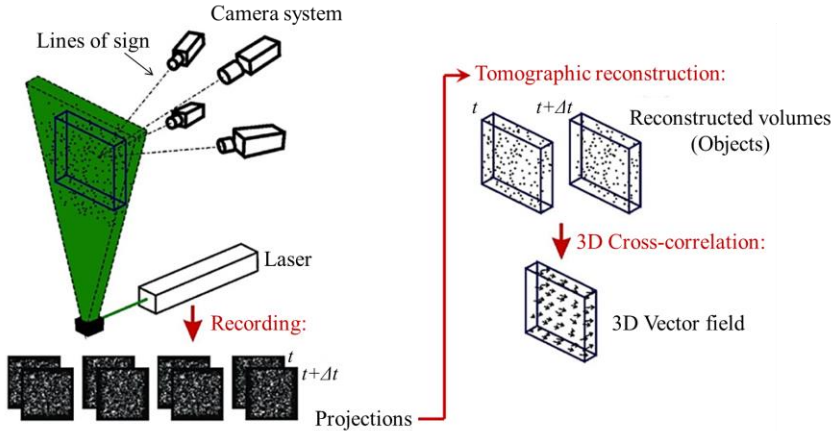


Figure 2.7 - Working Principle of tomo-PIV (Elsinga *et al.*, 2006).

2.10.2 Illumination

The measurement domain is normally illuminated with laser light, as in planar PIV. The laser beam can be expanded with the use of cylindrical and spherical lenses in order to cover the entire volume of interest with a similar procedure as that described in section 2.3.3. Two different effects should be considered in Tomo-PIV illumination. First, the intensity of the laser beam is inversely proportional to the thickness of the beam itself. Second, a large camera aperture is required to image in-focus all the tracers across the domain, which further reduces the amount of light reaching the sensor. As a result, the need for a larger illumination requires laser beams of higher intensity than the ones used in 2D-PIV. Different techniques are adopted to increase the light intensity recorded by the imaging system. One of these is the multi-pass technique introduced by Schröder *et al.* (2008) and Ghaemi and Scarano (2010) which exploits two high-reflecting mirrors placed at the side of the measurement domain. The laser beam is therefore reflected

back and forth within the mirrors multiple times increasing the light amplification effect in the measurement volume. Another way to increase the light scattered into the cameras is to use relatively larger particle tracers. The last choice needs to be compromised with the need of tracers with good tracking fidelity. This issue has been the main reason to study HFSB which can fulfil both the requirements of light scattering and tracing fidelity, due to the larger size and the neutral buoyancy condition, as it is described in chapter 3.

2.10.3 *Imaging*

In Tomo-PIV experiments, the arrangement of the cameras normally requires the fulfilment of the Scheimpflug condition as in stereoscopic PIV, especially when the width and the height are larger than the depth of the measurement volume. As mentioned before, it is important to maintain the particles in-focus along the entire depth in the domain of interest. In order to verify the latter condition, the optical focal depth δZ can be estimated with equation (2.5) and the numerical aperture $f_{\#}$ can be optimized accordingly.

2.10.4 *Tomographic reconstruction and 3D vector fields*

The recorded images of the cameras define the 2D intensity distributions $I(x',y')$. These scattering fields are used to retrieve a 3D field in the physical space $E(x,y,z)$ using the following inverse problem

$$\sum_{j \in N_i} w_{i,j} E(x_j, y_j, z_j) = I(x'_i, y'_i) \quad (2.11)$$

where i identifies the i^{th} pixel and N_i the number of voxels along the line-of-sight (*LOS*) of the pixel which contributes to its intensity. The

value w defines the weight of the contribution of the j^{th} voxel to the i^{th} pixel intensity and depends on the distance d between the voxel and the line-of-sight. Different procedures to calculate w are described by Thomas *et al.* (2010). Figure 2.8 shows an illustration of the projection model for tomographic reconstruction.

The MART (multiplicative algebraic reconstruction technique) algorithm introduced by Herman and Lent (1976) has become the most used one for the reconstruction of the signal from Tomo-PIV images.

The non-uniqueness of the solution of the under-determined algebraic problem of equation (2.11) results in the generation of *ghost particles*. The latter consist of spurious intensity peaks appearing in the reconstructed intensity field together with real particles. As spurious peaks, the ghost particles do not follow the flow and they can contribute to the generation of outliers during the cross-correlation analysis. A detailed description of the *ghost particles* behavior can be found in the work of Elsinga *et al.* (2011).

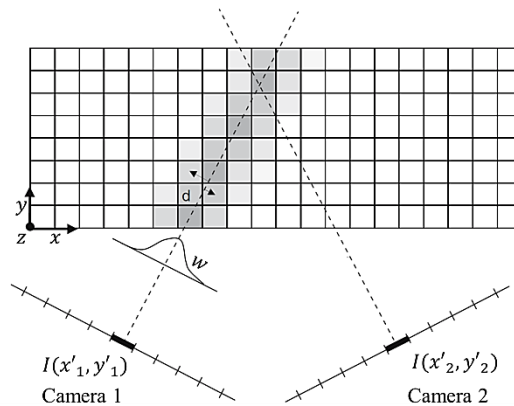


Figure 2.8 - Two-dimensional sketch of the projection model for tomographic reconstruction; dashed lines indicate the lines-of-sight of pixels. Voxels are color-coded depending on the value of w and their distance from the LOS is indicated with d (Elsinga *et al.*, 2006).

The final outcome of the reconstruction can be analysed by 3D spatial cross-correlation yielding 3D velocity fields characterized by homogeneous vector grid. The correlation analysis for tomographic PIV is extended from pixel to voxel-based object. Some of the correlation techniques, used in 2D PIV, can be used for 3D data such iterative process and window deformation.

The reconstructed objects can be used also to determine the particle motion following individual tracers with a Lagrangian approach in the so called Tomo-PTV technique. The latter is similar to the 3D PTV and allows the evaluation of full particle trajectories in time-resolved measurements which yield a higher precision on the material derivative estimate (Novara and Scarano, 2013). The advantage of Tomo-PTV, with respect to the standard 3D PTV, is related to the higher image seeding density allowed for a correct particle triangulation, and, therefore, a higher vector field resolution.

The information provided by the particle tracking algorithms is sparse and it is not suitable for the evaluation of vorticity or pressure fields. Different techniques are used to interpolate PTV data onto a structured grid such linear and adaptive Gaussian windowing (Agüí and Jiménez, 1987). A more advanced technique named vortex-in-cell plus, VIC+ (Schneiders and Scarano, 2017), employs both the instantaneous velocity and the velocity material derivative of the sparse tracer particles to reconstruct the instantaneous velocity field.

3

SEEDING PARTICLES

3.1 Introduction

As mentioned in chapter 2, there are two fundamental aspects to be considered in the choice of seeding particles for a PIV experiment. The first is the dynamic behaviour, which depends on the mechanical properties of the tracers as well as determining the tracing fidelity of the particle flowing within the fluid. Secondly, the optical properties and the ability to scatter enough light to the cameras. The latter is essential to form bright images of particles. As a consequence, the selection criterion relies on a compromise between the two previous aspects. In this chapter, I illustrate the procedure to separately examine these properties. The choice among these often conflicting requirements is not discussed here as it often stems from the requirements of the specific experiment. The main parameters to estimate and quantify the tracing fidelity are introduced, namely the particle relaxation time and Stokes number. The fundamental aspects of light-particle interaction are also treated taking into account the properties that mostly affect the intensity of light scattering.

3.2 Dynamic behaviour

The motion of seeding particles immersed in the fluid flow results from the mutual exchange of forces. The particle trajectory can be modelled using the equation of motion (Newton's second law) provided that all relevant forces are known. The latter depend on the properties of the tracers, the fluid, and the flow. One of the main parameters that describe the aerodynamic behaviour of a spherical particle immersed in a flow is the particle Reynolds number defined as

$$\text{Re}_p = \frac{|U_f - U_p| d_p}{\nu_f} \quad (3.1)$$

where d_p is the particle diameter and ν_f the fluid kinematic viscosity. The relative velocity of the particle with respect to the fluid $U_f - U_p$ is named slip velocity U_{slip} (Figure 3.1). The particle Reynolds number determines the flow regime around the tracer and in turn, its drag and the slip velocity.

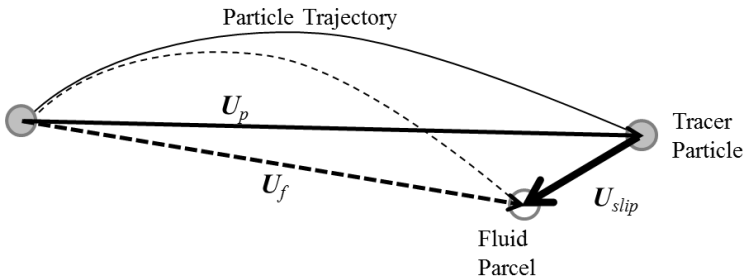


Figure 3.1 - Relative motion of a tracing particle.

Two regimes are considered for the tracer dynamics. Maxey and Riley (1983) developed the equation of motion for a spherical particle in the Stokes regime ($\text{Re}_p \ll 1$). Secondly, a particle dynamic equation was

proposed by Mei (1996) with a range of validity up to $Re_p \approx 170$ for which the intrusiveness of the tracers is still considered negligible. Taneda (1956) experimentally documented that the flow remains laminar and attached for $Re_p < 20$ in the wake behind a sphere. In the range of $20 < Re_p < 130$ a stable wake develops behind the cylinder with the presence of a vortex ring. For $Re_p > 170$, an unsteady-oscillating wake will develop (Kim and Perlstein, 1990) downstream the sphere.

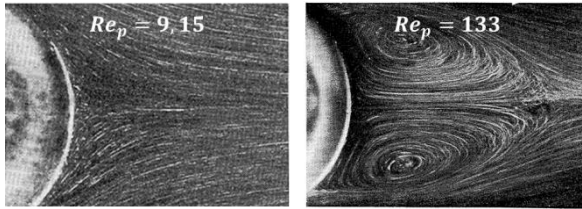


Figure 3.2 - Flow patterns for different Re_p (Taneda 1956).

In the regime where $Re_p < 1$, the motion of a small tracer is well approximated by the Stokes flow model. The latter yields the flow around the sphere and its drag. To estimate the relative velocity, U_{slip} , between the particle tracer and the surrounding flow (Raffel *et al.*, 2013) reads:

$$U_{slip} = U_p - U_f = d_p^2 \frac{(\rho_p - \rho_f)}{18\mu} \frac{dU_p}{dt} \quad (3.2)$$

where ρ_p the particle density. The density and dynamic viscosity of the flow are indicated with ρ_f and μ , respectively. Equation (3.2) shows that the slip velocity is directly proportional to the acceleration. The ideal particle behaviour is obtained when the tracers satisfy the neutral buoyancy condition: $\rho_p \approx \rho_f$. This condition can be easily achieved in water flows using, for instance, polyamide particles or hollow glass

spheres. In air flow applications very small particles ($d_p \sim 1 \mu\text{m}$) are commonly used to minimize the slip velocity due to the particle density which is three orders of magnitude larger than the air one. Only with the recent introduction of sub-millimetre helium-filled soap bubble (HFSB) by Bosbach *et al.* (2009), the neutrally buoyant condition was achieved in airflows allowing the use of larger tracers. Figure 3.3 depicts the order of magnitude of the Re_p for different particle size used in PIV experiments and the corresponding slip velocity.

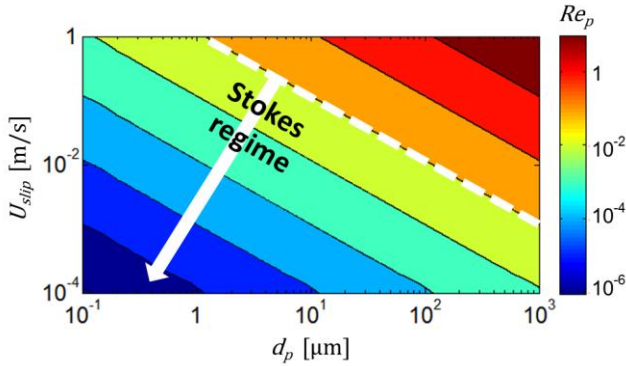


Figure 3.3 - Contour of Re_p as a function of slip velocity and particle size.

3.2.1 Equation of motion

The model proposed by Maxey and Riley (1983) takes into consideration the equation of motion resulting from a number of forces acting on a spherical particle of mass m_p

$$m_p \frac{d\mathbf{U}_p}{dt} = \sum_i \mathbf{F}_i \quad (3.3)$$

More explicitly, the model of Maxey and Riley describes the following forces:

$$m_p \frac{d\mathbf{U}_p}{dt} = \mathbf{F}_{G-B} + \mathbf{F}_{QS} + \mathbf{F}_{FS} + \mathbf{F}_{AM} + \mathbf{F}_H \quad (3.4)$$

Equation (3.4) includes the gravity-buoyancy force \mathbf{F}_{G-B} , quasi-steady drag force \mathbf{F}_{QS} , pressure force (or fluid stress force) \mathbf{F}_{FS} , added-mass force \mathbf{F}_{AM} and history force \mathbf{F}_H . Only the forces relevant for the application studied in the following chapters will be described. For a comprehensive analysis of equation (3.4) the reader is referred to the work of Mei (1996), where the analysis of the forces acting on the particles covers also the case of finite Reynolds number $\text{Re}_p > 1$.

The drag in Stokes regime on a solid sphere is defined as:

$$\mathbf{F}_{QS} = 6\pi\mu_f \frac{d_p}{2} \mathbf{U}_{slip} \quad (3.5)$$

The pressure force acts on a sphere immersed in a flow field with a pressure gradient. At high flow Reynolds number the pressure gradient can be related to the fluid acceleration and the pressure force can be expressed using Euler's equation valid for inviscid flows:

$$\mathbf{F}_{FS} = \frac{4}{3}\pi \left(\frac{d_p}{2}\right)^3 \rho_f \frac{D\mathbf{U}_f}{Dt} \quad (3.6)$$

In aerodynamics, pressure forces become relevant close to the stagnation and in highly rotational regions like in the core of vortices. In particular, when a particle is moving within a vortex, the forces acting along the radial direction are the centrifugal and the pressure forces, which balance each other for a neutrally buoyant tracer. In case of heavy tracers (such as liquid droplets in air) the unbalance of the latter two results in a net outward motion with a drag force given proportional to the radial drift velocity, as it is shown in equation (3.5).

The additional effect of the inhomogeneous pressure distribution over the particle surface is discussed in the work presented in chapter 6.

3.3 Characteristic time

Following Raffel *et al.* (2013), let us consider the particle response to an abrupt velocity change in the flow such as across a shock wave (step response). In this case, equation (3.2) and (3.4) are combined and only the viscous drag and inertial force are accounted for. The resulting relation is:

$$\frac{d\mathbf{U}_p}{dt} = \frac{1}{\tau_p} (\mathbf{U}_f - \mathbf{U}_p) \quad (3.7)$$

Under the assumption of Stokes flow regime, τ_p is a constant that does not depend on the fluid velocity or acceleration, but depends only on the fluid and particle properties. The analytical solution of equation (3.7) for a step function returns an exponentially decaying particle velocity, where the characteristic time is expressed as:

$$\tau_p = d_p^2 \frac{(\rho_p - \rho_f)}{18\mu_f} \quad (3.8)$$

τ_p is named *relaxation time* of the tracer and represents the time after which the velocity variation of the particle is $(1 - e^{-1}) = 63\%$ of the imparted velocity difference. Even if the particle response time can be defined only within the Stokes regime, it remains a convenient parameter to characterize the tendency of tracers to adapt to velocity variations in the flow even outside the latter regime.

Finally, the Stokes number, defined as the ratio of the particle relaxation time τ_p over the flow characteristic time τ_f , is a suitable measure that defines the tracing fidelity of particle in a specific flow:

$$St = \frac{\tau_p}{\tau_f} \quad (3.9)$$

It has been discussed (Samimy and Lele, 1991) that the condition $St < 0.1$, is sufficient to consider that the particle faithfully follows the flow.

3.4 Optical behaviour

As mentioned in chapter 2, PIV relies on the determination of the particle image displacement to retrieve the flow velocity. For this reason, the light scattered by the particle is a key factor for the image processing and it is important to record the particle images with an acceptable signal-to-noise ratio relative to the image background. For a given incident light intensity, the amount of light scattered by the particles is mainly dependent on the ratio of the refractive index of the tracer to that of the fluid n , the particle size d_p , the observation angle θ_s , and the wavelength of the light λ . The particle scattering range is expressed in terms of the Mie scattering parameter:

$$x_m = \frac{\pi d_p}{\lambda} \quad (3.8)$$

Under the assumption of spherical particles, the theory of Mie (1908) offers a complete description of the scattered light of a plane incident wave that interacts with a generic spherical particle. One of the first investigations on the scattering properties of fluid tracers for PIV

measurements was performed by Adrian and Yao (1985). Figure 3.4 shows the scattering intensity as a function of the particle diameter for $n = 1.5$ corresponding to oil or glass particles in air. For small particles ($x_m \ll 1$), the scattering intensity is proportional to d_p^4 . The size of conventional seeding particles for airflows is of the order of $1 \mu\text{m}$ ($x_m \approx 1$) and the scattering intensity scales with d_p^3 . For $x_m \gg 1$, the scattering behaviour approaches the geometric limit and the scattering intensity is proportional to d_p^2 . The scattering ranges are named as Rayleigh ($x_m < 1$), geometric optics (GO) ($x_m > 90$), and the intermediate range is called the Mie region (Tropea, 2011).

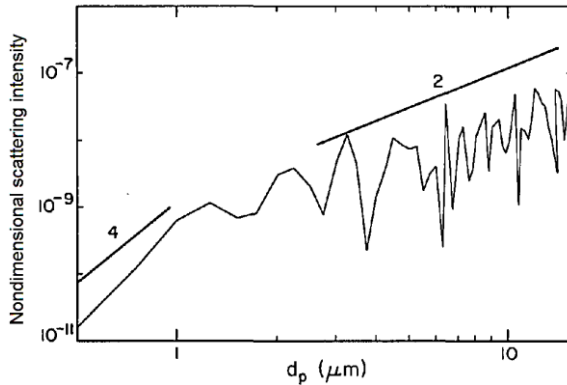


Figure 3.4 - Non-dimensional scattering intensity as function of particle diameter for $n = 1.5$ (Adrian and Yao, 1985).

In PIV experiments the range of interest is $x_m > 1$, considering particles that are larger than $1 \mu\text{m}$ and a light beam with a wavelength of $\lambda \approx 530 \text{ nm}$. The Lorenz-Mie theory gives the exact solution of the light scattering problem for spherical and homogeneous particles that interact with a plane wave of the incident light (van de Hulst, 1957); the corresponding computational models are described in the work of Barber and Hill (1990).

The light-particles interaction consists in reflection, refraction, and diffraction. Reflection involves a change in direction of light beams when they bounce off a surface. Refraction of waves involves a change in the direction of waves as they pass from one medium to another. The light interacting with a particle forms a discontinuous plane wave front where the missing part has the same size of the geometrical projection of the particle. The incomplete wave front produces at very large distance an intensity peak, the Fraunhofer diffraction pattern or simply diffraction.

The main parameters that characterise the total light scattered by the particle is its size, the relative refractive index and the wavelength of the light. The scattering intensity increases with d_p^s , where s ranges from 2 to 4 from geometric to Rayleigh regime, as it is shown in Figure 3.4. The polar diagram in Figure 3.5 illustrates the dependence of the scattered light intensity on the scattering angle θ_s . The peak intensity in forward scattering is mainly due to diffraction, while the other local maxima are the result of interference between the diffracted, reflected, and refracted light. The angular distribution and intensity of the diffraction peak depends only on the size of the particle and they are independent from the material and nature of its surface.

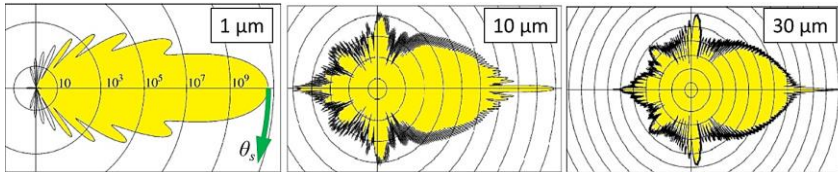


Figure 3.5 - Light scattering intensity in polar coordinates of different diameter glass particles in water according to Mie theory (Raffel *et al.*, 2007).

Figure 3.5 shows how the diffraction lobe will be more intense but compressed in a smaller solid angle around $\theta_s = 0^\circ$ in the far field increasing x_m . As a consequence, for large particles, the scattering due

to reflection and refraction can be decoupled from the diffraction pattern (van de Hulst, 1957). It is noticed that for PIV imaging systems the forward-scattering is not possible ($\theta_s = 0^\circ$) and the effect of the diffraction can be neglected.

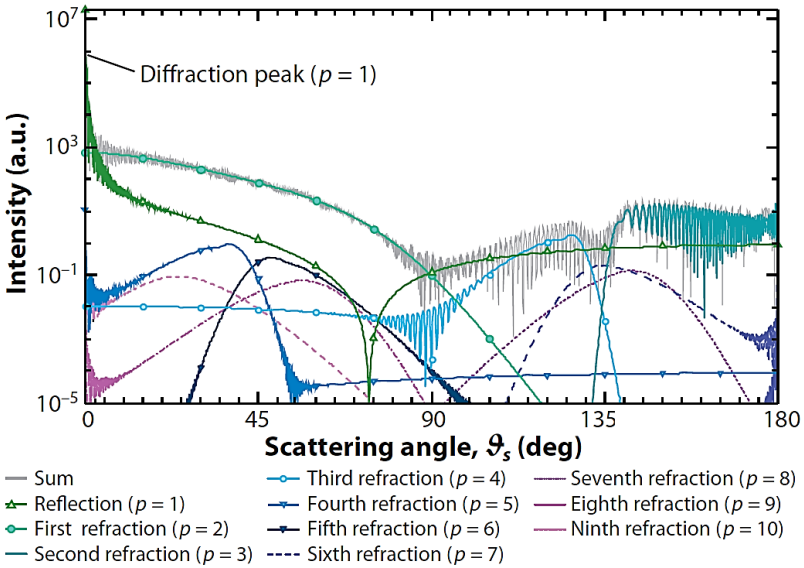


Figure 3.6 - Scattered light intensity as a function of scattering angle, decomposed for the first 10 scattering orders calculated with Lorenz-Mie theory and Debye series decomposition for an incident plane wave, $\lambda = 488$ nm, $x_m = 643.8$, $n_p/n_f = 1.333$ (Tropea, 2011).

The number of maxima in the interval $[0^\circ, 180^\circ]$ is approximately equal to x_m (Adrian and Westerweel, 2011). However, in PIV experiments the scattering light is recorded within a solid angle, defined by the object distance and the lens aperture. As a result, the light intensity is averaged over a range of angles and therefore considerably smoothed. In the range of geometrical optics, the scattered light can be represented as the interaction between the light rays reflected and refracted from the

particle. The reflections are considered specular, meaning that incident and reflected rays make the same angle with respect to the normal of the interface, namely $\alpha_i = \alpha_r$, as it is shown in Figure 3.7. The direction of the refracted ray follows from Snell's law:

$$n_1 \sin \alpha_i = n_2 \sin \alpha_t \quad (3.9)$$

The intensity of transmitted and reflected light at each interface is described by the Fresnel equations and is a function of relative refractive index and polarization. The solution of Fresnel equation differs between s- (incident light polarized with its electric field perpendicular to the plane containing the incident, reflected, and refracted rays) and p-polarization (the incident light is polarized with its electric field parallel to the plane of incidence).

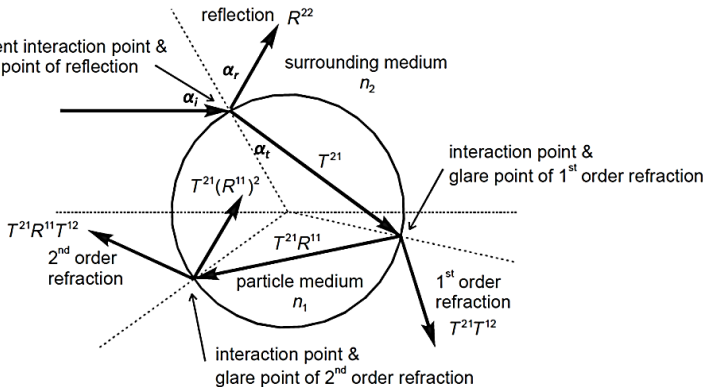


Figure 3.7 - Decomposition of an incident ray into reflection and refractive scattering orders for a droplet according to geometric optics (Albrecht 1999).

For non-polarised light beams, the arithmetic mean of the previous two solutions is used. The fraction of the incident power that is reflected from the interface is given by the reflectance or reflectivity, R , and the

fraction that is refracted is given by the transmittance or transmissivity, T :

$$R_s = \frac{|n_2 \cos \alpha_i - n_1 \cos \alpha_t|^2}{|n_2 \cos \alpha_i + n_1 \cos \alpha_t|^2} \quad (3.10)$$

$$R_p = \frac{|n_2 \cos \alpha_t - n_1 \cos \alpha_i|^2}{|n_2 \cos \alpha_t + n_1 \cos \alpha_i|^2} \quad (3.11)$$

$$T_{s-p} = 1 - R_{s-p} \quad (3.12)$$

In equation (3.12), the amount of energy lost by absorption inside the particle is assumed negligible. Figure 3.8 shows the distribution of the reflection coefficients of light as function of incidence angle. At one particular angle for given refractive indices n_1 and n_2 , the value of R_p goes to zero and a p-polarised incident ray is purely refracted. This angle is known as Brewster's angle, and is about 54° when the light passes from air to oil with $n_{oil} = 1.4$ (Figure 3.8-left).

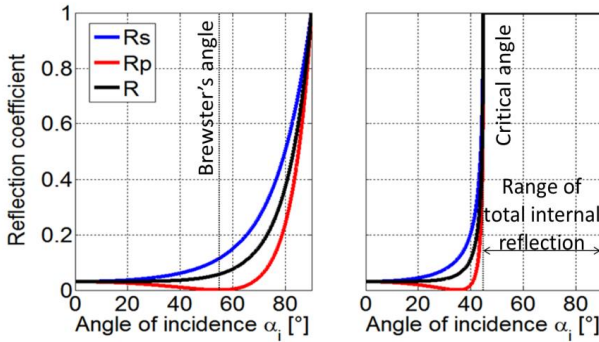


Figure 3.8 - Reflection coefficients of light as function of incidence angle for the interface air-oil (right) and oil-air (left).

When the light moves from a denser medium into a less dense one (Figure 3.8-right) above an incidence angle known as the critical

angle, all light is reflected and $R_s = R_p = 1$. This phenomenon is known as total internal reflection.

3.5 Common seeding particles for aerodynamics

The seeding particles used in aerodynamics are produced in a wide range of materials and size depending on the application. Oil-based droplets are mostly used from sub-sonic to compressible flows, metal oxide powders are often used in supersonic wind tunnel. Al_2O_3 and TiO_2 among others, offer the advantage of a high refractive index. An overview of the tracers used in gas flow with relevant parameters is shown in Table 3.1

Table 3.1 Seeding particles for PIV experiments in aerodynamics.

Material	d_p [μm]	ρ_p [Kg/m^3]	n	τ_p [μs]	Source
DEHS	0.5 - 1.5	912	1.4	1-2	Kähler <i>et al.</i> (2002)
Olive Oil	1 -10	970	1.4	1-4	Melling (1997)
TiO_2	0.01	4230	2.5	0.4	Ragni <i>et al.</i> (2011)
Al_2O_3	0.2 – 5	4000	1.7	20-28	Urban & Mungal (2001)

3.6 HFSB

In a large measurement volume, detecting individual tracer particles to obtain pathlines becomes increasingly difficult when the particles are characterized by small size. The energy flux of laser light decreases rapidly when the illumination is distributed over a large cross section. Moreover, the observation from a larger distance causes a quadratic decay of the scattered light intensity. A possible approach to compensate for the above effects is that of employing particles with

large diameter (see also fig 3.4). However, the tracer particles should have the same density of the fluid to ensure their fidelity to the flow motions, as described in the previous sections. This requirement has suggested the helium-filled soap bubbles (HFSB) as a viable solution due to their potential towards neutral buoyancy and their large diameter on the order of 0.1-1 mm. In the past decades, the HFSB tracers with a diameter on the order of millimetres have been employed for qualitative visualization of different aerodynamic flows, such as the flow around a parachute (Pounder, 1956; Klimas, 1973), separated flow around an airfoil (Hale RW, 1971), wing-tip vortices (Hale *et al.*, 1971) and jet flows (Ferrell, 1985). The low concentration of the HFSB along with their large diameter makes them ideal for visualization of the pathlines of individual fluid elements within complex flows.

Müller *et al.* (1997) and Müller *et al.* (2000) have conducted some of the first planar measurements using HFSB of approximately 2 mm in diameter. The experiments were performed inside an aircraft cabin to study the convective flow within a field of view of $2 \times 2.5 \text{ m}^2$. More recently, Machacek and Rösger (2003) have used HFSB of 2-3 mm in diameter for the 3D reconstruction of path lines in large scale wind tunnels. In the last 20 years, the HFSB technology improved up to the design of a new type of bubble generator by DLR (German Aerospace Agency). This type of nozzle was named *orifice type nozzle* and used by Okuno *et al.* (1993) first, but only after the enhancements of DLR (Bosbach *et al.*, 2009), the bubble generator was able to produce sub-millimetre bubbles (approximately 0.2-0.3 mm) and with a production rate higher than 50,000 bubbles per second. Thanks to these achievements, the HFSB technology is now ready to be adopted in wind tunnels, where the constraints related to the bubble size and to the production rate are much stricter than for convective flows in enclosures.

3.6.1 Optical properties

The helium-filled soap bubble has a different optical behaviour compared to all tracers commonly used in PIV experiments. Considering a light beam with a wavelength of $\lambda = 530$ nm, the Mie parameter for HFSB is approximately $x_m \approx 1800$ and the optical behaviour can be studied by means of geometrical optics and ray tracing. The bubbles are considered heterogeneous because of the presence of a thin and transparent film of bubble fluid solution (BFS) with two interfaces and an inner volume filled with helium. From the optical point of view, the bubble can be considered as a hollow shell because the difference between the refractive indexes of helium and air is below 0.1%.

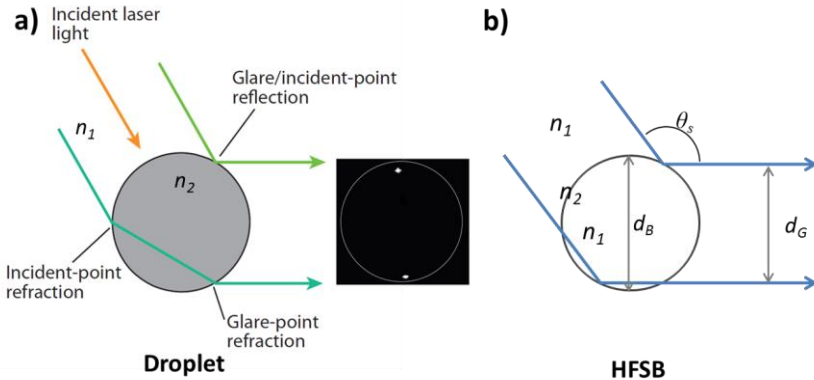


Figure 3.9 - Schematic overview of glare point for $\theta_s = 120^\circ$. a) Glare points generated by a droplet in the geometrical optics (Tropea, 2011). b) Glare points generated by HFSB.

Moreover, the thickness of the BFS film is three orders of magnitude smaller than bubble diameter (less than a micro-meter). Therefore, the ray deflection due to the refraction of light passing through the film or in the helium core is negligible. As a consequence, the two glare points

that reflect light rays in θ_s are equidistant with respect to the centre of the bubble, as indicated in Figure 3.9. The distance of the glare points depends on the bubble diameter and scattering angle:

$$d_G = d_B \cos\left(\frac{\pi}{2} - \theta_s\right) \quad (3.13)$$

In particular, Figure 3.9 shows the main difference between the glare points generated by a droplet (a) or HFSB (b). A more detailed analysis on the optical behaviour of HFSB will be presented in Chapter 7, where the ray tracing technique will be used to evaluate the scattering intensity collected by the imaging system for different bubble diameter and scattering angle.

4

HFSB SEEDING IN WIND TUNNELS

Part of the material presented in this chapter is published in the article “HFSB-seeding for large-scale tomographic PIV in wind tunnels”, from GCA Caridi, D Ragni, A Sciacchitano, F Scarano, *Experiments in Fluids* 57, 2016.

4.1 Introduction

The use of soap bubbles in wind tunnels as flow tracers dates back to the 1938, year in which Redon (1938) had filed the patent ‘*Means for materializing the stream*’ of air-flows. From that moment, these tracers have been mostly used to visualize individual path-lines within complex flows. A brief description of the evolution of the bubble generator has just been given (section 3.6), where some examples of flow visualisations conducted in the past are also listed. The devices currently used for the generation of HFSB are characterized by production rate ranging from 10^4 to 10^5 bubbles per second. This makes the image analysis via standard cross-correlation unsuited due to the resulting low seeding concentration. Moreover, uniform tracer dispersion in the airflow cannot be achieved with the use of a single-point source of tracers. These are the reasons that prevented the use of HFSB for PIV measurements in wind tunnels. In this chapter, the method adopted to overcome such limitations will be described. In

particular, it will be described a seeding system which could produce a sufficient amount of HFSB for large-scale PIV experiments in wind tunnels. In chapter 2, the relation between measurement spatial resolution and seeding concentration was introduced. This information is used here to guide the design of the seeding system based on HFSB for PIV experiments. In addition, the relevant parameters to scale the system and its main components will be described.

4.2 Bubble generator system

The production system of HFSB consists of a fluid supply unit (FSU) and a nozzle. The unit has the function of controlling the flow rate of helium, soap fluid, and air by setting the pressure upstream of the supply line.

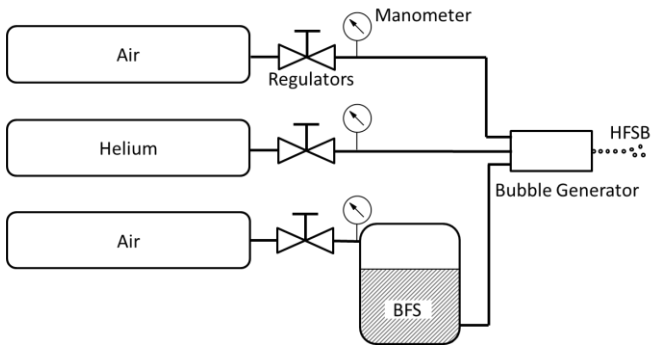


Figure 4.1 - Sketch of supply unit for HFSB generators.

Both air and helium are provided by pressurized vessels. Compressed air is also used to pressurize the tank of BFS and regulate its mass flow through the nozzle. A secondary stream of air is led to the nozzle through a regulator, as in the case of the helium line. It was chosen

helium as a filler gas because it compensates for the weight of the soap and it is a non-toxic and inert gas. Generation of neutrally buoyant (NB), lighter-than-air (LTA), and heavier-than-air (HTA) bubbles relies on a dedicated adjustment of the flow rates of He and BFS. The bubble generators used in this work are based on a design made by the German Aerospace Centre (DLR) and presented in the work of Bosbach *et al.* (2009). The sketch of the nozzle is reproduced in Figure 4.2. Helium is blown through a central pipe, which is mounted coaxially into a second channel. Through the latter, the bubble fluid solution (BFS) is driven at a controlled flow rate. Thus, small bubbles are generated and their separation from the pipe being driven by the air flow through the additional air-ducts.

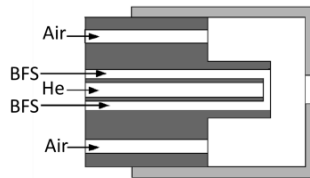


Figure 4.2 - Sketch of the HFSB nozzle (Bosbach *et al.*, 2009).

The present bubble generator has the highest production rate among those reported in the literature (Okuno *et al.*, 1993; Müller *et al.*, 2001; <http://www.sageaction.com/>), as shown in Table 4.1.

Table 4.1 Production rate of different HFSB generators.

Research Group	Production rate [bubbles/s]
Toyota—Tokyo University	3000
Sage Action Inc.	300 - 400
RWTH Aachen University	500
DLR	50,000
LaVision	50,000

In the work of Scarano *et al.* (2015), the bubble generator was placed downstream of a wind tunnel contraction and was able to generate a seeded stream-tube of approximately 3 cm width with no noticeable variation for a range of free-stream velocity between 1 and 30 m/s. It can be concluded that the use of a single generator is deemed unsuited for conducting large-scale three dimensional PIV experiments.

4.3 Production regimes

The generation process of HFSB has direct effects on PIV measurements where the bubbles are used as tracers. Tracers with monodisperse distribution in size and density are preferable for more accurate measurements. For this reason the production process of HFSB is investigated and was documented in the previous work of Morias *et al.* (2016). The HFSB generators used in the experiments described in the following chapters were developed in order to produce bubbles in a so-called *co-flow* configuration, also commonly used for air bubble production in water flows (Sevilla *et al.*, 2005a). Sevilla *et al.* (2005b) and Gañán-Calvo *et al.* (2006) discussed the importance of the velocity ratio between the co-flowing fluids for a stable and continuous bubble production.

Two different formation regimes were identified: *bubbling* and *jetting*. The latter is characterized by a long cylindrical ligament of the discrete phase that breaks up far from the exit of the generator. This results in aperiodic and polydisperse bubble production. Conversely, the *bubbling* regime features a fairly periodic and stable formation of the bubbles at the exit of the nozzle. The details of HFSB formation at the exit of the nozzle are inspected with high-speed shadowgraph at 90 kHz, with continuous back-illumination. The results illustrate an example of the stable *bubbling* regime (Figure 4.3-a). The

visualizations also reveal the formation of small droplets at the moment of detachment. Although irrelevant for the bubble diameter, this phenomenon may affect the dispersion of bubble weight.

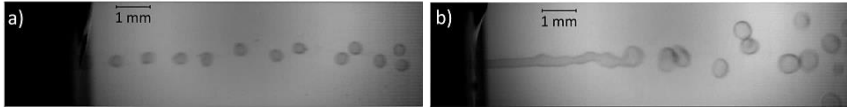


Figure 4.3 - High speed visualization of HFSB production in bubbling (a) and jetting regime (b).

In the observed *bubbling* regime, HFSB are ejected with a velocity of 20 m/s and with an average separation distance of less than 1 mm between each other. The production rate is estimated to be approximately 50,000 bubbles per second. When the bubble generator operates in the *jetting* regime, a quasi-cylindrical interface of BFS protrudes from the exit of the nozzle (Figure 4.3-b). It was observed that the cylindrical film is affected by large scale fluctuations and occasionally breaks up into bubbles far from the orifice. In the present case, the two regimes are obtained with the same flow rates of helium and at different flow rates of air, as shown in Table 4.2. It is observed that increasing the flow rate of air, the bubble production regime changes from bubbling to jetting.

Table 4.2 Supply flow rates for different regimes of HFSB production.

Regime	Q_{He} [l/h]	Q_{BFS} [ml/h]	Q_{Air} [l/h]
Bubbling	5	5	115
Jetting	5	5	160

Figure 4.4 shows the comparison between the size distributions of HFSB generated in both regimes. In bubbling production, the HFSB show a monodisperse distribution within 5% variation in diameter.

While, for the jetting regime the dispersion appears to be rather broad with multiple peaks in the distribution and an overall dispersion exceeding 25% of the arithmetic mean.

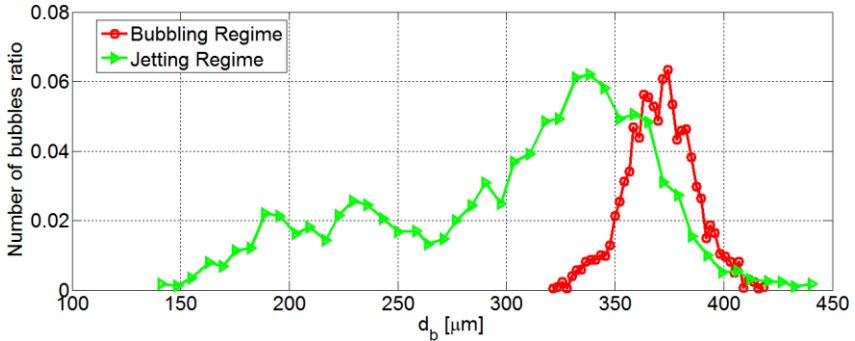


Figure 4.4 - HFSB diameter distribution in bubbling and jetting regime.

4.4 Use of HFSB in wind tunnels: Production rate and DSR

In this section, the relationship between the production rate of the HFSB and the *DSR*, defined in chapter 2, is discussed. Moreover, the influence of the location where the tracers are injected, namely upstream or downstream the wind tunnel contraction, is considered.

When using HFSB tracers, the concentration is limited by the maximum rate at which they can be released by an emitter. Moreover, given their large size and the limited lifetime, reported to be within 2 minutes (Bosbach *et al.*, 2009), the tracers are only used once after their emission, since they do not circulate around closed-loop wind tunnels. The present discussion is based on the hypothesis that HFSB tracers are released by an emitter at a rate \dot{N} bubbles/s and travel

without disturbing the flow within the stream-tube of cross section A corresponding to that of the emitter device, with the local flow velocity U . The rate at which the bubbles cross a plane normal to their direction of convection reads as:

$$\dot{N} = CAU \quad (4.1)$$

A simple example is given here to illustrate the requirements in terms of bubble production rate. Let us assume that a stream-tube with velocity of 10 m/s and a square cross section of $1 \times 1 \text{ m}^2$ is to be seeded at a concentration of 5 bubbles/cm³ ($I_V = 1 \text{ cm}$ for $N_I = 5$). The generation system needs to supply tracers at $\dot{N}=50 \times 10^6$ bubbles/s, which exceeds by three orders of magnitude the production rate of a single generator. The resulting DSR for such conditions would be around 100, which compares well to that of many planar PIV experiments reported in the literature (Raffel *et al.*, 2013; Westerweel *et al.*, 2013). Substituting C from the expression of the dynamic spatial resolution defined in equation (2.8), the DSR reads now as:

$$DSR = L \left(\frac{\dot{N}}{N_I A U} \right)^{\frac{1}{3}} \cong \left(\frac{L \dot{N}}{N_I U} \right)^{\frac{1}{3}} \quad (4.2)$$

In the last derivation on the right-hand-side term, it is assumed that $A \approx L^2$, i.e. the seeded stream-tube cross section is comparable to the characteristic length of the object of interest. Equation (4.2) states the dependence of the DSR upon the characteristic length of the measurement volume, the amount of HFSB entering the measurement volume per unit of time and the local stream velocity. The bubble rate in the measurement volume is thereby pivotal to achieve the required DSR . High values of \dot{N} yield a high concentration, which in turn increases the dynamic spatial range. On the other hand, as in every

tomographic PIV experiments, the number of ghost particles (Maas *et al.*, 1993) rapidly increases with the density of particle images (Discetti, 2013), which affects the accuracy of tomographic reconstruction and motion analysis, as discussed in the work of Elsinga *et al.* (2011). However, as shown in recent experiments with HFSB (see chapter 8), the particle image density levels achieved are far below the critical value of 0.05 ppp (particles per pixel) suggested in the work of Elsinga *et al.* (2006). Finally, the *DSR* is inversely proportional to the stream velocity U .

Equation (4.2) can also be interpreted as follows: for a given value of the Reynolds number, higher values of *DSR* can be achieved increasing the size of the scaled model and reducing the velocity. It may be concluded that scaling up the Reynolds number with the geometrical scale is a more convenient approach than increasing the velocity for achieving a high *DSR* with HFSB tracers.

The location of the seeding emitter inside the wind tunnel also affects the *DSR* of the measurement. Here, two relevant cases are discussed. The seeding probe could be installed inside the settling chamber (Figure 4.5-left) or downstream the contraction ahead the test section (Figure 4.5-right). In the latter case, the emitter must be placed sufficiently far upstream of the measurement volume such that to allow a sufficient decay of its wake.

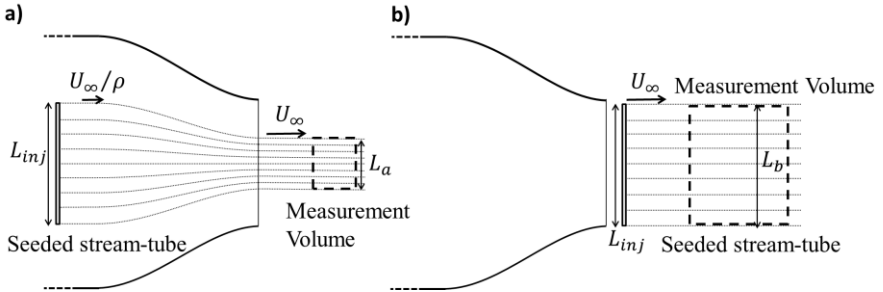


Figure 4.5 - Sketch of the seeded stream-tube for the injection inside the settling chamber ($\rho > 1$) and downstream the contraction ($\rho = 1$).

The presence of the contraction changes the flow velocity where the seeding is released by a factor $1/\rho$, where ρ is defined as the ratio between the cross-sectional area of the injector and that of the seeded stream-tube in the test section. As a consequence of the different volume of air seeded per unit of time, the concentration of flow tracers depends upon the chosen configuration. Assuming the cross section of the seeding probe to be L_{inj}^2 , with a constant bubble injection rate into the flow \dot{N} , the seeding concentrations read as:

$$C = \frac{\dot{N}}{L_{inj}^2 (U_\infty/\rho)} \quad (4.3)$$

In the above equation, the flow is assumed incompressible and lateral spreading of the stream-tube due to turbulent mixing is neglected. Equation (4.3) shows that the concentration of HFSB is higher when the emitter is placed in the settling chamber ($\rho > 1$). Conversely, the flow contraction reduces the cross section of the seeded stream-tube scale, which may be regarded as a disadvantage when the measurement region needs to cover large objects. The relationship between the emitter characteristic length and that of the seeded stream-tube is

$$L = \rho^{-1/2} L_{inj} \quad (4.4)$$

Combining equation (2.8) with equations (4.3) and (4.4), it is possible to retrieve the *DSR* ratio between the two configurations as follows

$$\frac{DSR_a}{DSR_b} = \frac{L_a}{L_b} \left(\frac{C_a}{C_b} \right)^{\frac{1}{3}} = \rho^{-\frac{1}{6}} \quad (4.5)$$

The ratio expressed in equation (4.5) quantitatively represents the effect of the contraction on the *DSR* in a volumetric PIV measurement. The dependence upon the 1/6 root indicates that the ratio in equation (4.5) is weakly dependent upon the chosen configuration, however, with a slight advantage in case the emitter is placed directly in the wind tunnel freestream. Furthermore, in many situations, the access to the settling chamber is limited if not impossible; thus, case *b* remains a more practical choice.

Figure 4.6 shows the dependence of the HFSB concentration *C* and the *DSR* upon the size of the emitter L_{inj} and the seeded stream-tube contraction ρ . The calculation is made assuming free-stream velocity of 8.5 m/s, a bubble emission rate of 8×10^5 bubbles/s and a particle image number density of 5, corresponding to the experiment presented chapter 8 on the vertical axis wind turbine (VAWT). Four values of the contraction ratio ρ are considered, namely 1, 3, 9 and 18, covering a range commonly encountered in low-speed wind tunnels (the last three numbers correspond to the OJF, W-tunnel and LTT wind tunnel, respectively, of the aerodynamics laboratory of TU Delft). The case with unitary contraction corresponds to case *b* where the injector is placed in the test section upstream of the model, which corresponds to the configuration used in the experiment described in section 8.2. These results are used to predict the concentration and the *DSR* for a given seeding system.

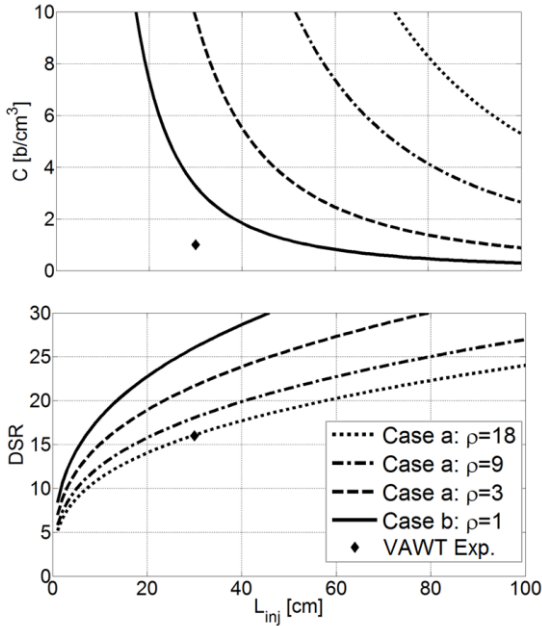


Figure 4.6 - Concentration (*above*) and *DSR* (*below*) as function of the characteristic length of the injector and of the contraction ratio. Equation (4.3) is used to retrieve C . DSR was computed using equation (4.2) where L is replaced by the relation expressed in equation (4.4) ($\dot{N}=8 \times 10^6$, $U_\infty=8.5$ m/s).

The increase of the injector size is detrimental to the seeding concentration unless additional bubble generators are added into the system. In Figure 4.6-left, for example, the concentration reduces of one order of magnitude when L_{inj} increases from 20 to 100 cm. In contrast, the dynamic spatial range increases with the size of the emitter and the one of the seeded stream-tube. On the other hand, the dynamic spatial range increases with the size of the seeding injector. In Figure 4.6, the working point of the seeding system used in the VAWT experiment (described in the chapter 8) is also shown. The seeding

system was used in configuration *b*, with the bubbles injector placed in the test section.

Due to the limited HFSB concentration, typically not exceeding a few bubbles per cubic centimetre, experiments conducted with HFSB are suited for image analysis based on PTV (particle tracking velocimetry) approaches, which requires that the average distance between the particles is large with respect to the average particle displacement (Maas *et al.*, 1993). The equations discussed above remain conceptually valid also for PTV analysis, provided that the image number density is set to unity: $N_I = 1$. It is well known that PTV approaches allow higher spatial resolution, whereas cross-correlation approaches yield higher probability of valid vector detection (Adrian, 1991). Furthermore, correlation-based techniques yield velocity data defined in a regular Cartesian grid, which is better suited for the computation of spatial derivatives and flow-derived properties as vorticity.

A survey of tomographic PIV experiments is given in Table 4.3 where the achieved *DSR* is reported. The dynamic spatial range of tomographic PIV experiments typically varies between 20 and 30. The recent introduction of HFSB certainly increases the measurement domain size, at the cost, however, of a lower *DSR*, mostly ascribed to the poor concentration of the tracers. The latter limitation is partly due to the current unavailability of HFSB generators that can accurately produce neutrally buoyant tracers at rates in the order of 10^7 – 10^8 bubbles/s. Moreover, the less fundamental, yet very relevant problem of uniformly introducing the tracers upstream of the test section with minimum intrusion to the free-stream flow conditions requires dedicated technical solutions. The experiment described in chapter 8 describes the concept and the realization of a seeding system that multiplies the instantaneous bubble emission rate from a single

generator to produce a quasi-uniform stream of seeded flow in a large-scale wind tunnel.

Table 4.3 Dynamic spatial range for relevant Tomographic PIV experiments in air flows

	Measurement domain linear size L [mm]	Interrogation box linear size I_B [mm]	DSR
Elsinga <i>et al.</i> (2006)	40	2.1	19
Staack <i>et al.</i> (2010)	50	2.5	20
Schröder <i>et al.</i> (2011)	63	2.7	22
Kühn <i>et al.</i> (2012) ^a	840	38	22
Fukuchi (2012)	160	5	30
Wake of a cylinder ^b	200	20	10

^a Experiment conducted with HFSB in a closed volume.

^b Experiment described in section 8.2.

4.5 HFSB injection in wind tunnels

The approach followed to increase both the rate of tracers injected in the flow as well as the size of the seeded stream-tube makes use of a dedicated system (Figure 4.7) composed of a HFSB generator that releases the bubbles inside of a large cylindrical reservoir (30 cm diameter and a volume of approximately 70 litres). The HFSB tracers are temporarily accumulated, while a piston driven by an electrical linear actuator increases the available volume. At the end of the expansion, the piston rapidly inverts its motion and conveys the air and the bubbles from the reservoir towards an injector placed in the wind tunnel through a flexible pipeline (3.6 cm diameter and 1.7 m length).

The latter is connected to the injector that distributes the tracers within a stream-tube.

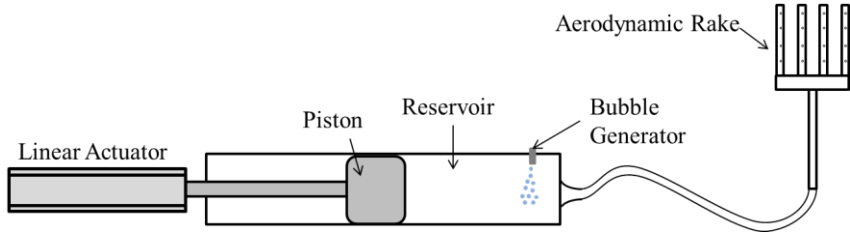


Figure 4.7 - Schematic description of seeding storage and transient injection system.

The aerodynamic rake can be placed in the settling chamber of the wind tunnel as done in the experiments described in section 8.2, or directly placed in the free-stream as in the current experiments. In the latter case, the expected cross section of the stream-tube coincides with that of the aerodynamic rake. The geometry of the injector is presented in Figure 4.8 and consists of an aerodynamic rake with 12 bi-convex aerofoils, with a chord of 10 cm and a thickness of 1.2 cm, arranged over two staggered rows. Each aerofoil has 22 orifices with a diameter of 3 mm along the trailing edge. The overall cross section of the rake is $30 \times 36 \text{ cm}^2$; only 550 cm^2 are obstructed by the aerofoil and therefore contribute to the blockage (considering the total amount of 12 aerofoil). However, one should keep in mind that the aerofoil are placed in two rows of six, which are staggered with respect to each other, thus reducing the blockage. This is considered negligible, less than 6 % blockage, in large wind tunnels with cross section of 1 m^2 or larger. Finally, the air flow injected with the HFSB from the seeding probe depends on the stroke of the piston and the injection time. For the experiment with the VAWT that is described in section 8.3, the additional air flow rate is $0.04 \text{ m}^3/\text{s}$. The latter is rather small in

comparison with the air flow crossing the overall cross section of the rake at 10 m/s (approximately $1 \text{ m}^3/\text{s}$), and it is certainly negligible when compared to the wind tunnel air flow rate.

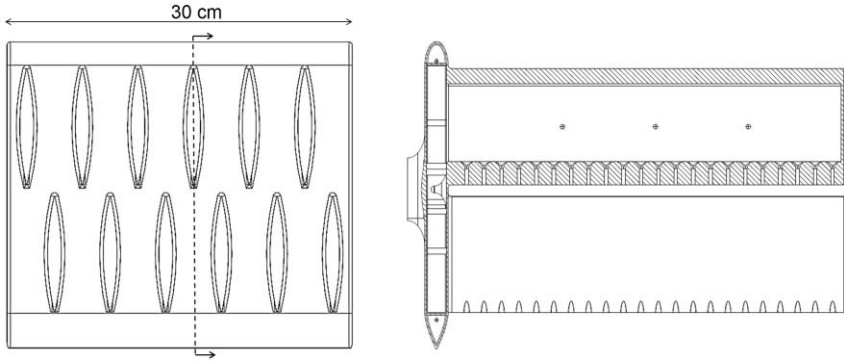


Figure 4.8 - Scale drawing of aerodynamic rake with 12 bi-convex airfoil staggered in two rows and with 264 orifices. *Left* top view; *right* section view.

The production rate of the bubble generator installed in the reservoir is indicated with \dot{N}_0 . As mentioned in previous sections, $\dot{N}_0 = 50,000$. The piston moves backward at constant speed, increasing the available volume during a time interval Δt_0 (*accumulation time*). After that, the piston rapidly moves forward during a time interval Δt_1 (*release time*). The total number of bubbles produced during one period of the piston motion is $\dot{N}_0 (\Delta t_0 + \Delta t_1)$. In the ideal case where all the produced bubbles are ejected from the system during release, the rate at which the bubbles exit the cylindrical reservoir is:

$$\dot{N}_1 = \dot{N}_0 \frac{\Delta t_0 + \Delta t_1}{\Delta t_1} \approx \frac{\Delta t_0}{\Delta t_1} \dot{N}_0 = G \dot{N}_0 \quad (4.6)$$

The accumulation time needs to be shorter than the lifetime of the bubbles which is approximately 2 minutes. In the present

case, $\Delta t_0 \gg \Delta t_1$. The time ratio $\Delta t_0 / \Delta t_1$ represents the *gain factor* G of bubble rate obtained by the seeding system compared to a single bubble generator. Assuming that during the accumulation phase, all the bubbles stay in the cylindrical reservoir, whose maximum volume during the accumulation time Δt_0 is V_0 , and the bubbles concentration within the reservoir is:

$$C_0 = \dot{N}_0 \frac{\Delta t_0}{V_0} \quad (4.7)$$

Outside of the seeding system, the bubbles concentration decreases to C due to dilution with the air flow crossing the injector during release:

$$C = \frac{\dot{N}_1 \Delta t_1}{V_0 + V_{wt}} = \frac{\dot{N}_0 \Delta t_0}{V_0 + V_{wt}} \quad (4.8)$$

V_{wt} is the air volume flowing through the diffuser and in which the bubbles are ejected. The term V_{wt} can be expressed as:

$$V_{wt} = A u \Delta t_1 \quad (4.9)$$

where U is the velocity of the flow in which the HFSB are injected and is equal to U_∞ / ρ in case *a* (injector in the settling chamber) and U_∞ in case *b* (injector in the test section). Substituting equation (4.9) into equation (4.8) and making use of the definition of the gain factor, the expression of the concentration becomes:

$$C = \frac{\dot{N}_0 G}{\frac{V_0 + V_{wt}}{\Delta t_1}} = \frac{\dot{N}_0 G}{\frac{V_0}{\Delta t_1} + A u_\infty} = \frac{\dot{N}_0 G}{\dot{V}_0 + A u_\infty} \quad (4.10)$$

Equation (4.10) shows the dependence of the concentration from the main working parameters of the seeding system. The choice of the

bubble generator determines the bubbles production rate \dot{N}_0 , and therefore it is crucial for the optimization of C . The latter is directly dependent upon the gain factor, which is varied by changing the accumulation time Δt_0 , provided it does not exceed the bubbles lifetime. The cross section of the seeded stream-tube A , determines the air volume flow rate where the bubbles are released and therefore the dilution in the wind tunnel. Increasing A reduces the concentration of tracers.

Using equation (4.10) with the values in Table 4.4, corresponding to the VAWT experiment (section 8.3), a theoretical concentration (C_{th}) of 3 bubbles per cm^3 are expected. This concentration allows tomographic PIV measurements to investigate flow structures of the order of a few centimetres, as it will be done for the analysis of the blade tip vortex of a vertical axis wind turbine. The concentration observed within the measurements (C_{meas}) is considerably less than the above one (1 bubble/ cm^3) as shown in Figure 4.6-left. This difference is ascribed to a number of factors; most importantly, bubbles extinction during their transport from the reservoir to the exit of the injector and bubble collisions inside the reservoir. As a result of the lower concentration, the tomographic PIV analysis is conducted with larger interrogation windows, yielding in turn a lower spatial resolution.

Concluding, it was noticed that the loss of bubbles upstream of the injector poses some limits to the seeding system described above. A possible solution to comply with this issue will be the use of many bubble generators in parallel installed directly inside the wind tunnel. A multi-generator system allows producing HFSB directly in the stream of the wind tunnel without transport losses and introduction of the air volume V_0 . The latter alternative, however, requires a large number of nozzles, on the order of G for a given $\dot{N}_0 = 50,000$ in order to retrieve the same concentration and DSR obtained for the present seeding system. In section 8.4 is described the measurements conducted in the

air-wake of a frigate, where the first prototype of a multi-nozzle injector was tested. The analysis performed in the present section can be extended to the latter case, provided that a unitary gain factor ($G = 1$) and the total production rate of all nozzles are considered.

Table 4.4 Theoretical and measured bubble concentration

\dot{N}_0 [b/s]	Δt_0 [s]	Δt_1 [s]	G	V_0 [cm ³]	A [cm ²]	U_∞ [m/s]
50,000	50	1	50	16,000	900	8.5

C_{th} [b/cm ³]	C_{meas} [b/cm ³]	DSR_{th}	DSR_{meas}
3	1	28	13

5

DYNAMIC BEHAVIOUR OF HFSB

The material presented in this chapter is published in the article “On the use of helium-filled soap bubbles for large-scale tomographic PIV in wind tunnel experiments”, from F Scarano, S Ghaemi, GCA Caridi, J Bosbach, U Dierksheide, A Sciacchitano, *Experiments in Fluids* 56: 42.

5.1 Introduction

The previous chapter evaluated the requirements for a sufficient HFSB-seeding density for three-dimensional PIV. Nonetheless, the main requirement for flow seeding particles is their ability to follow the flow. In this chapter, the dynamic behaviour of HFSB will be discussed. The aerodynamic performance of the HFSB in tracing the flow field has been investigated by Kerho and Bragg (1994) at the stagnation region of a NACA 0012 airfoil. Their experiments reported a deviation of the HFSB trajectories from the theoretical streamlines due to non-neutrally buoyant tracers. This was mostly due to the use of a cyclone device used to reject the heavier bubbles.

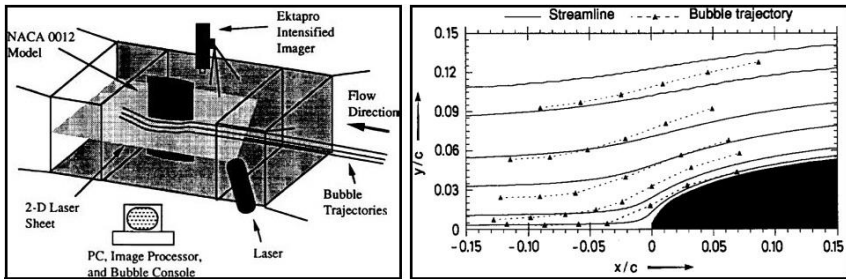


Figure 5.1- First quantitative measurement with HFSB ($d_b \approx 1\text{-}5$ mm) in a wind tunnel. Experimental set-up (left). Comparison of HFSB trajectories (dashed-line) with the numerical results (solid line) in the potential flow ahead a NACA0012 (right).

Therefore, the average weight of the tracers was biased towards lighter-than-air bubbles. They concluded that “*the use of bubbles generated by the commercially available system to trace flow patterns should be limited to qualitative measurements unless care is taken to ensure neutral buoyancy*”. As a result, the HFSB have been mostly used only in quantitative measurements of convective flows at low velocities (typically less than 1 m/s). The present chapter will present the experimental procedure, similar to the one adopted by Kerho and Bragg, to determine the particle relaxation time τ_p which quantify the flow-tracing capability in low-speed wind tunnels. The study is conducted using the last generation of bubble generator developed in DLR (Bosbach *et al.*, 2009), which is able to produce sub-millimetre diameter HFSB. Additionally, the reference velocity field is not inferred with potential flow theory, but additional PIV measurements with micro-size droplets are carried out.

5.2 Experimental apparatus and procedure

Experiments are conducted in a low-speed open-section wind tunnel (W-Tunnel) of the Aerodynamic Laboratories of the Aerospace Engineering Department at TU Delft. A 1.4-m-long rectangular channel follows the contraction nozzle. The exit cross section is $0.4 \times 0.4 \text{ m}^2$.

A circular cylinder of 25 mm diameter is placed at the exit. This geometry is chosen by ease of reproducibility and the scaling of the potential flow with the diameter on the front side. Moreover, the flow behaviour is stationary and the topology of the stagnation is similar to that at the leading edge of airfoil as used by Kerho and Bragg (1994). The schematic layout of the experiment is illustrated in Figure 5.2. Experiments are conducted at free-stream velocity of 30 m/s.

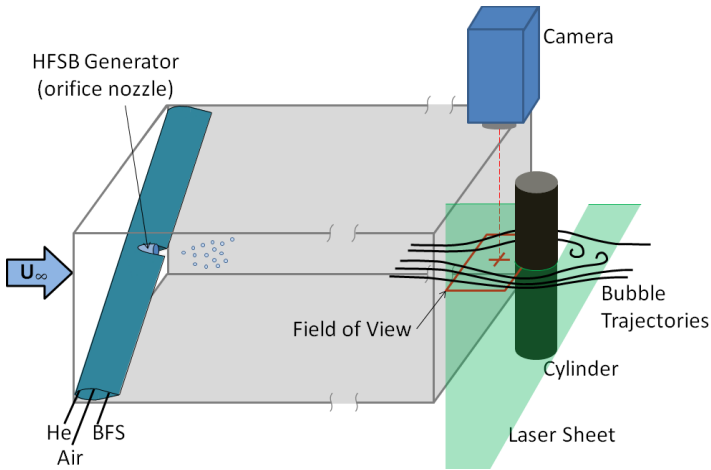


Figure 5.2 - Schematic arrangement of the experiment: wind tunnel channel and exit; HFSB injection; cylinder model; illumination, imaging and measurement region.

The HFSB generator is fed by constant flow rates of helium, bubble fluid solution (BFS) and air. The BFS is a mixture of water, glycerine and soap. Unlike the fluid supply unit described in the previous chapter, for the present experiment, stable operational conditions were achieved by controlling the BFS, air and helium flow using digital thermal mass-flow controllers (Bronkhorst High-Tech). Most experiments are conducted at a flow rate of 70 l/h for the air flow. Soap and helium flow rates were varied as reported in Table 5.1.

Table 5.1 Volume flow rates for HFSB production during experiments

\dot{v}_{BFS} [ml/h]	3	4	5	6	3	4	5	6
\dot{v}_{He} [ml/h]	4	4	4	4	5	5	5	5

Given the size of the tracers and the operating flow velocity, the Reynolds number related to the bubble diameter has an order of magnitude above 1. For micro-size tracers, the operating Reynolds is typically below unity, indicating that the interactions with the surrounding fluid pertain to the Stokes regime. Therefore, the behaviour of the tracers can be reduced to a time constant τ_p , referred to as the relaxation time. For small, heavy particles the relaxation time depends upon the square of the diameter and the difference in density to the fluid (Melling 1997).

Although a relaxation time for helium-filled soap bubbles τ_{HFSB} may not be a constant property, dimensional considerations enable to determine its order of magnitude as the ratio between the slip velocity (i.e. the local difference between the tracer velocity U_{HFSB} and the immediately surrounding fluid velocity U_{air}) and the local fluid parcel acceleration a .

The latter reads as

$$\mathbf{a} = \frac{\partial \mathbf{U}}{\partial t} + \mathbf{U} \cdot \nabla \mathbf{U} \quad (5.1)$$

For steady flow conditions ($\partial \mathbf{U} / \partial t = 0$), the local fluid acceleration only depends upon the transport term $\mathbf{U} \cdot (\nabla \mathbf{U})$, which simplifies the valuation of flow and particles acceleration from experiments. In conclusion, the estimation of the time response is evaluated according to the following expression:

$$\tau_{HFSB} = \left| \frac{\mathbf{U}_{HFSB} - \mathbf{U}_{air}}{\mathbf{U}_{air} \cdot \nabla \mathbf{U}} \right| \quad (5.2)$$

In the present experiments, only the streamwise component is considered along the stagnating streamline.

5.3 Velocity measurements

The reference velocity field is obtained by PIV measurements using micro-size droplets from a smoke generator (*SAFEX Twin Fog*). Illumination is provided by a *Quantronix Darwin-Duo Nd: YLF*, which has nominal pulse energy of 25 mJ at 1 kHz. The beam is shaped into a light sheet of 2 mm thickness. The imaging system consists of a *Photron Fast CAM SA1* camera (CMOS, 1,024×1,024 pixels, 12-bit, and pixel pitch 20 μm). The camera is equipped with a 105-mm *Nikkor* objective at aperture setting of f/5.6; the imaging magnification is $M = 0.54$. The active size of the sensor is 608×448 pixels. Sequences of 5,000 double-frame images were acquired with time separation of $\Delta t = 25 \mu s$ (for a free-stream velocity of 30 m/s) at acquisition frequency of 500 Hz. The image cross-correlation process is carried out within *LaVision Davis 8.1.4* with final window size of 32×32 pixels and overlap factor of 75 %. The resulting vector pitch is approximately 0.3 mm. The same equipment is used to measure the average velocity

field of the HFSB tracers. Due to the much lower concentration of the HFSB tracers in the individual images, the cross-correlation analysis is applied to a single image pair that superimposes 5,000 recordings from a sequence.

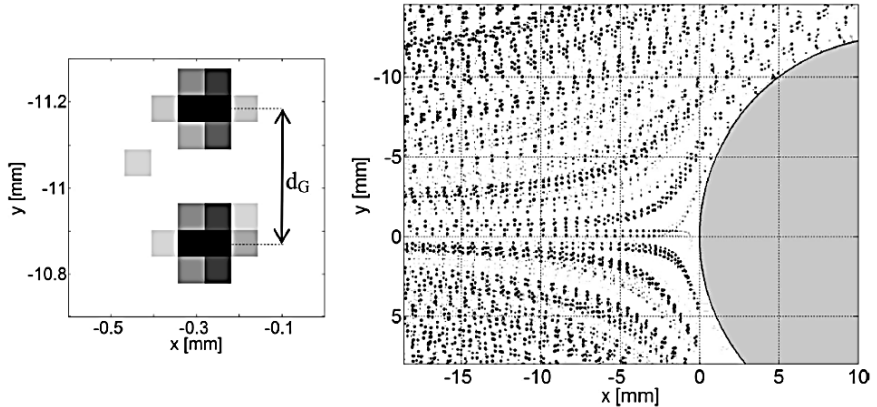


Figure 5.3 - *Left* glare points from a single image of HFSB. *Right* superimposed exposures of HFSB tracers.

Furthermore, high-speed measurements at a rate of 20 kHz enable the analysis of the trajectory from individual HFSB tracers by the PTV technique. The analysis is made with a MATLAB script based on particle peak detection and trajectory evaluation using a velocity predictor from the fog droplet velocity field. The multi-point trajectory is regularized with a least-squares regression of a third order polynomial based on a kernel of seven exposures. It is worth noting that every bubble produces a pair of glare spots (van de Hulst and Wang 1991). In the present experiment, these are oriented along the vertical direction, as it is shown in Figure 5.2-left. As mentioned in section 3.6.1, the glare points are always symmetrical with respect to the bubble centre; hence, no bias error is produced in the location of the bubbles.

In the present experiment, illumination and imaging directions are approximately perpendicular. Therefore, the distance between the glare points d_G determines the bubble diameter $d_b = \sqrt{2} d_G$. Based on the latter hypothesis, the bubble diameter in the present experiment is estimated as $d_b = 400 \mu\text{m}$. The presence of the glare points poses an additional problem for the cross-correlation analysis, as the correlation map exhibits two side-peaks corresponding to the autocorrelation of the glare points. This is taken into account by ignoring the regions of the correlation map affected by the autocorrelation of the glare points. Similarly, the PTV analysis is made with the additional condition that no confusion is made in pairing the lower glare point with the higher one between subsequent exposures. The tracking of particles is refined with sub-pixel precision using a Gaussian peak fit as commonly done in PIV. Finally, the centre of the bubble is assumed to be in the middle position between the two glare points.

5.4 Aerodynamic behaviour of HFSB

The analysis of the aerodynamic behaviour of the HFSB tracers aims at determining the characteristic time scale of the tracer response. The time-averaged streamlines of the HFSB are compared with the result obtained with fog droplets in Figure 5.3. At the lowest helium flow rate, the streamlines of the bubbles produced with the highest soap fluid flow rate show a delayed response with respect to the decelerating air flow. Such behaviour is representative of heavier-than-air tracers. This is clearly visible from the trajectory close to the stagnation point, where the heavier tracers advance further before deviating upwards. This effect is consistently observed for all streamlines related to the condition ($\dot{v}_{He} = 4 \text{ l/h}$, $\dot{v}_{BFS} = 6 \text{ ml/h}$). When the rate of soap fluid is decreased, the overall density of the tracers is reduced and the deviation

from the air flow trajectories becomes less significant. For $\dot{v}_{BFS} = 4$ or 5 ml/h, the difference between air and HFSB trajectories can barely be noticed.

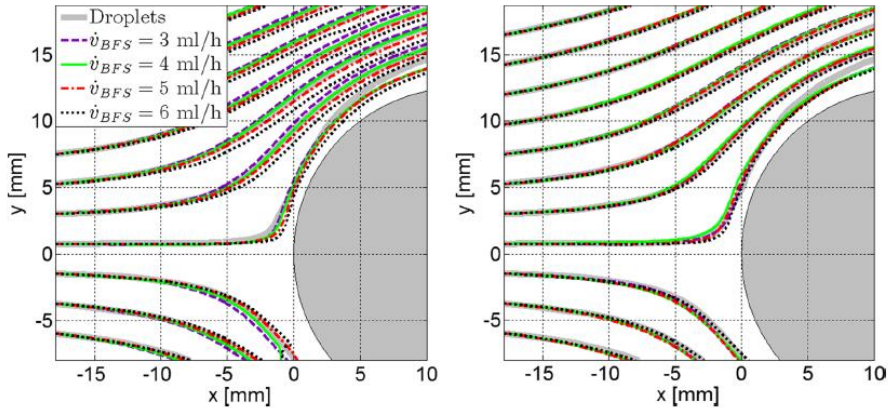


Figure 5.4 - Time averaged streamlines at $U_{\infty} = 30$ m/s obtained with micro-size droplets and HFSB with four different volume rates of BFS and two volume rates of helium: $\dot{v}_{He} = 4$ l/h (left), $\dot{v}_{He} = 5$ l/h (right). Streamlines determined by cross-correlation analysis.

Further reduction in the soap fluid flow produces lighter-than-air tracers, which exhibit a *floating* behaviour with respect to the pressure gradient imposed by the cylinder at stagnation. As a result, the trajectories for $\dot{v}_{BFS} = 3$ ml/h depart from the air flow by anticipating the deceleration and deviating earlier from the stagnation region, similar to the experiments conducted by Kerho and Bragg (1994).

Results obtained at higher helium flow rate ($\dot{v}_{He} = 5$ l/h) are included for completeness, where a similar behaviour of the tracers is noticed, although with less pronounced deviation from the air flow.

The velocity of the tracers travelling along the stagnation streamline is compared to the air flow in Figure 5.5. In the range of flow rates analysed here, the maximum velocity difference is estimated around

1 m/s for the heaviest or lightest tracers. Optimal conditions are approached when $\dot{v}_{He}=5$ l/h and $\dot{v}_{BFS}=5$ ml/h. In this case, the velocity difference is estimated to be < 0.5 m/s. The tracing fidelity appears to be more rapidly affected by varying the soap fluid rather than the helium flow rate. The velocity values are affected by an uncertainty of 0.5 m/s with a confidence level of 95%, which was obtained using the a-posteriori quantification procedure introduced by Wieneke (2014).

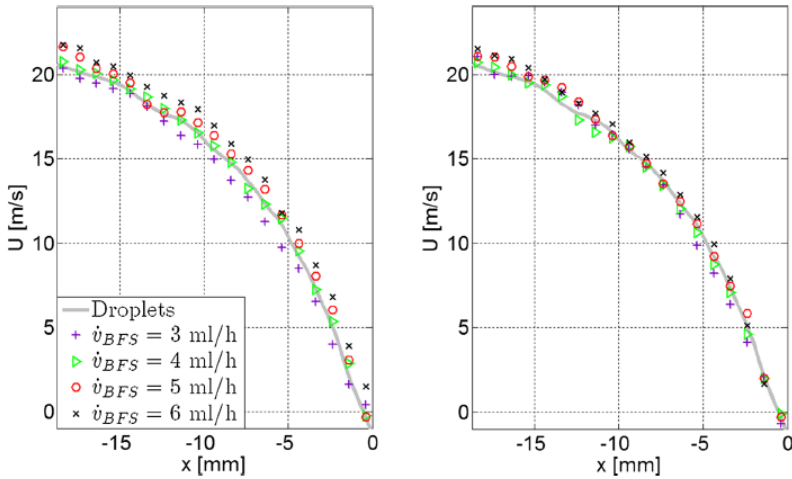


Figure 5.5 - Comparison of HFSB velocity along the stagnation streamlines. Results are shown for different values of the helium flow. *Left* $\dot{v}_{He} = 4$ l/h; *right* $\dot{v}_{He} = 5$ l/h.

The velocity and acceleration of individual tracers is based on the time-resolved measurements conducted at 20 kHz. Subsequently, the *slip velocity*, $U_{BFS} - U_{air}$, between the HFSB tracers and the air flow is computed. It should be remarked that in the present case, the velocity measurements with micro-size droplets are considered unaffected by errors due to slip velocity. The analysis is conducted around the stagnation streamline over a stripe of approximately 3 mm. Negative values of the mean slip velocity in Table 5.2 correspond to lighter-than-

air bubbles with lower flow rate of BFS. Instead, a positive value of the slip velocity is associated with heavier-than-air bubbles. The standard deviation of slip velocity is computed considering the contribution of all the bubbles crossing the control volume. The mean value of the slip velocity is slightly larger than 10 cm/s, for optimal tracers, corresponding to 0.3 % of the free-stream value. This indicates that HFSB tracers in the current experiment yield a rather unbiased average velocity field.

Table 5.2 HFSB tracing governing parameters, slip velocity, acceleration and characteristic response time for helium flow rate of $\dot{v}_{He} = 4$ l/h.

\dot{v}_{He} [ml/h]	Mean U_{slip} [m/s]	a_x [m/s ²]	τ_{HFSB} [μ s]
3	-0.37	-1.08×10^4	31
4	-0.14	-1.06×10^4	12
5	0.13	-1.06×10^4	11
6	0.51	-1.03×10^4	42

The value of the standard deviation from tracer to tracer is comparatively larger as it attains 2% of the free-stream velocity. This behaviour is ascribed to two possible effects. The first could be the different value of the slip velocity at varying positions in the domain. The second and more critical, following Bosbach *et al.* (2009), is related to the variation of bubbles properties, namely a variance in the diameter of 20 % for the same type of nozzle, in turn affecting the neutral buoyancy of HFSB.

The above measurements also yield the particles acceleration, which is reported for different values of the soap fluid flow rate (Figure 5.6). The acceleration of HFSB closely follows the trend of the reference PIV data obtained with fog droplets. The lighter bubbles appear to anticipate the deceleration induced by the adverse pressure gradient emanating from the stagnation line, whereas for the heavier bubbles,

the delay is not as evident. The ratio between the local slip velocity and the acceleration returns the HFSB characteristic time response.

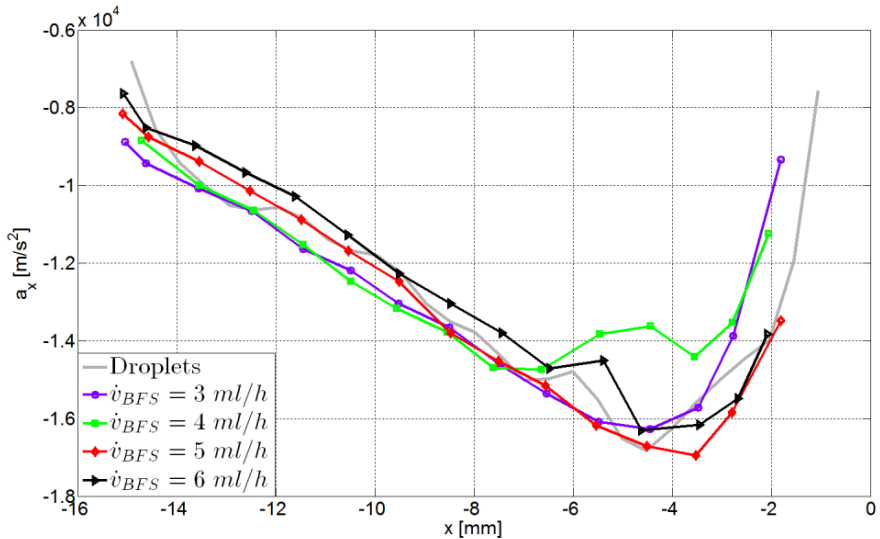


Figure 5.6 - Comparison of the horizontal acceleration of the bubbles (for different BFS flow rates and $\dot{v}_{He} = 4l/h$), with the time-averaged acceleration of the reference PIV data (micro-size droplets).

Table 5.2 summarizes the results, with minimum values of τ_{HFSB} in small excess of 10 microseconds. An estimate of the flow time scale for the present experiment is given by the ratio between the cylinder diameter and the velocity. For a free-stream velocity of 30 m/s, $\tau_{flow} = 800 \mu s$, which approximately two orders of magnitude above the tracer characteristic time. From the calculated values of τ_{HFSB} and τ_{flow} , it is concluded that in the present experiment the HFSB accurately follow the flow and can be used as flow tracers.

6

HFSB FOR VORTEX CORE VELOCIMETRY

Part of the material presented in this chapter is published in the article “Helium-filled soap bubbles for vortex core velocimetry”, from GCA Caridi, A Sciacchitano, F Scarano, *Experiments in Fluids* 58, 2017.

6.1 Introduction

In the previous chapter, the analysis on the tracing-fidelity for HFSB has shown a characteristic response time of the order of $\tau_{HFSB} \approx 10 \mu\text{s}$. The latter value is an order of magnitude larger than the one of micro-size droplets, commonly used in wind tunnels experiments (Raffel *et al.*, 2013). It is not surprising that in many flow conditions the tracking capability of micrometric droplets is higher with respect to a bubble with a diameter hundred times larger. Although, HFSB have demonstrated to be still accurate tracers for quantitative velocimetry in applications where the characteristic time of the flow is in the order of milliseconds.

Nevertheless, there are flows where body forces are dominant and they affect considerably the aerodynamic performance even of micro-size tracers. As an example, in swirling flow the centrifugal force

accelerates the particles radially outside the vortex. As a consequence, the seeding in air flows with high degree of circulation (e.g. tip vortices or leading edge vortices) is still recognized as a challenge in PIV measurements.

An example is the experiment of Hong *et al.* (2014), mentioned in chapter 1. Even if the large size of the natural snowfall tracers allows large-scale PIV measurements, the dynamic behaviour of these tracers generates a characteristic void signature within the vortex core resulting in lack of signal, as it is shown in Figure 6.1.

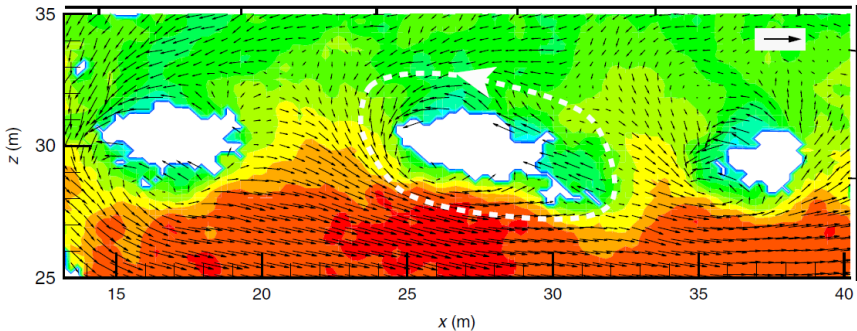


Figure 6.1 - Velocity vector field measured in the wake of a 2.5 MW wind turbine (Hong *et al.*, 2014), showing the effect of a non-homogeneous distribution of seeding particles within the core of the vortices (raw image in Figure 1.4-a).

A second example shows in Figure 6.2 the tip vortex measurements performed on a rotor system by Bhagwat and Ramasamy (2012) with conventional seeding. Even though micro-size particles have been used, the results are still affected by a lack signal in the vortex core. Other examples with micro-size particles are documented in the literature as mentioned in section 1.3.

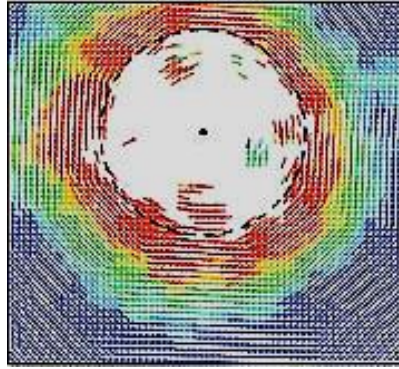


Figure 6.2 - Instantaneous PIV measurements of a tip vortex with conventional seeding (Bhagwat and Ramasamy, 2012).

In this flow topology, the buoyancy of tracers plays a key role. Tracers with weight approaching that of the surrounding fluid are not expected to suffer from the mentioned radial drift because of the balance between centrifugal force and pressure gradient. Therefore, HFSB are expected to preserve a uniform concentration within the highly swirling regions of the vortex.

The analysis of the present chapter is motivated by the above considerations. Firstly, a brief discussion of the dynamic behaviour of HFSB of sub-millimetre diameter in a vortical flow will be presented. Secondly, an experimental assessment will show a comparison between micro-size fog droplets and HFSB in a laminar vortex produced by a sharp-edged delta-wing. Laser sheet visualization is used to inspect the spatial concentration of tracers. Stereo-PIV measurements with fog droplets return a systematically underestimated axial velocity distribution within the vortex core due to drop-out of image cross-correlation signal. On the other hand, the nearly neutrally buoyant HFSB tracers appear to maintain a homogeneous spatial concentration and yield cross-correlation signal up to the vortex axis.

6.2 Particle dynamics in a vortex

The motion of a tracer particle immersed in a flow that features steady circular motion has been modeled in the work of Julien (1987) who studied the case of spherical particles moving in a Rankine vortex. In the present section, first an order of magnitude analysis is conducted, that determines the tracers Stokes number. The latter is followed by a more detailed evaluation of the drifting motion of the tracer immersed in a vortex based on the governing equations describing the motion of a small tracer. A direct, yet approximate, estimate of the adequacy of particle tracers in describing the fluid motion in a vortex can be based on the particle Stokes number St_k , the governing non-dimensional parameter for fluid-particles interaction. The latter is defined as the ratio between the characteristic response time of the particle to step-like velocity variation τ_p and the time scale representative of the flow under analysis τ_f . Following the work of Samimy and Lele (1991) values of St_k below 10^{-1} indicate that the tracers will follow the velocity fluctuations to within 1% discrepancy.

According to Rockwell (1993), the main time scale in a leading edge vortex released by a delta wing can be defined as the turn-over time: one local revolution of the vortex. Therefore, the characteristic time scale τ_f can be associated with the turn-over time τ_{to} , defined by the local value of the tangential velocity U_t and the radial position r , expressed as follows

$$\tau_{to} = \frac{2\pi r}{U_t} \quad (6.1)$$

The present experiments are conducted at free stream velocity of 10 and 30 m/s. Knowing that the maximum tangential velocity of the LEV is approximately equal to U_{inf} (Nelson and Pelletier, 2003), a Lamb-Oseen

vortex with a $U_{t,max} = U_{inf}$ is considered for the evaluation of the Stokes number along the radial position (Figure 6.3). In a previous work from the authors, the particle characteristic time response has been experimentally determined (Scarano *et al.* 2015), and it ranges from 10 to 50 μs . It is worth remarking that the conservative assumption of a particle response time of 50 μs is taken.

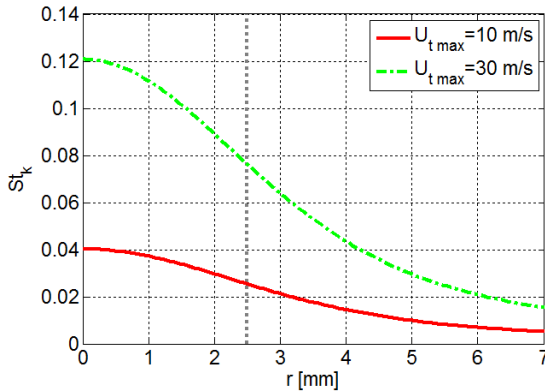


Figure 6.3 - Stokes number in a Lamb-Oseen vortex for HFSB tracers, vortex radius indicated with dashed grey line.

The particles Stokes number lies between 10^{-2} and 10^{-1} indicating that HFSB tracer particles are potentially suited to measure the velocity in this type of flow. Although the Stokes number pertaining micrometric droplets is significantly smaller (their response time is at least one order of magnitude below that of HFSB), their systematic drift causes the core depletion.

Recalling the work of Julien (1987), in the frame of reference that travels with the fluid parcel surrounding the tracer, three forces act onto the particle: the centrifugal force that results from the particle tangential velocity V_t along the curved trajectory, the pressure force F_P , and the

steady state drag force F_D due to the particle drifting radially with velocity V_r (Figure 6.4). The equation of motion is briefly recalled here:

$$m_p \frac{V^2}{r} = F_D + F_P \quad (6.2)$$

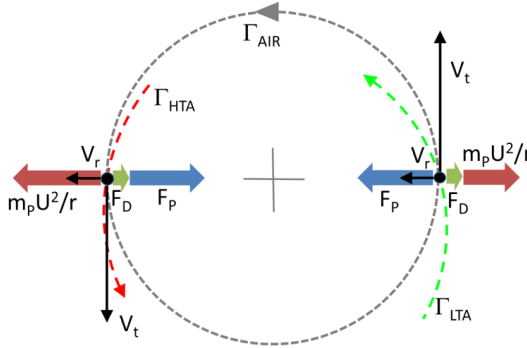


Figure 6.4 - Trajectory of heavier-than-air (Γ_{HTA} , dashed red) and lighter-than-air (Γ_{LTA} , dashed green) tracer within a flow with circular motion (Γ_{AIR}). Radial forces are indicated by thick arrows following definitions in Eq. 6.3. Tracer velocity decomposed into radial (V_r) and tangential (V_t) components.

where m_p is the tracer mass and r is the radius of the circular trajectory. The velocity of the fluid U is acting only on the tangential direction and it is assumed that $V_t = U$. The only relevant component of the velocity difference between the particle and the surrounding fluid velocity is the radial one, where tracers motion lead to depletion of the concentration in the core. Therefore, the radial particle velocity V_r corresponds to the velocity slip V_{slip} . The latter can be obtained expressing the terms in Eq. 6.2 as:

$$\frac{\pi}{6} d_p^3 \rho_p \frac{U^2}{r} = 3\pi \nu d_p \rho_f V_{slip} + \frac{\pi}{6} d_p^3 \rho_f \frac{U^2}{r} \quad (6.3)$$

Here, ρ_p and ρ_f are the density of the particle and of the fluid respectively and ν is the kinematic viscosity of the fluid. The transient effect of particle radial acceleration is not considered here. Therefore, the slip velocity corresponds to the limit radial velocity attained by the particle subject to a constant radial acceleration. The expression of V_{slip} is obtained from Eq. 6.3:

$$V_{slip} = \frac{1}{18} \bar{\rho} \frac{U^2}{r\nu} d_p^2 \quad (6.4)$$

where the normalized density difference $\bar{\rho}$ is given by:

$$\bar{\rho} = \frac{\rho_p - \rho_f}{\rho_f} \quad (6.5)$$

Equation 6.3 states that for a neutrally buoyant tracer (with $\bar{\rho} = 0$), the slip velocity vanishes, with the particle exhibiting a circular trajectory. A micrometric droplet (with $\bar{\rho} \sim 10^3$) will slightly move outward from the vortex core region. Lighter-than-air tracers ($\bar{\rho} < 0$) move in the opposite direction converging towards the centre of rotation: the vortex axis. The magnitude of the radial velocity increases linearly with the deviation from the neutrally buoyant condition, while it is proportional to the second power of the particle diameter and is highest at the edge of the vortex core where the flow exhibits high angular velocity. The latter consideration is relevant for the comparison between HFSB and micro-droplets, because the former approximately satisfy the neutral buoyancy condition ($\bar{\rho} \cong 0$); however their diameter is two orders of magnitude larger.

A numerical example is introduced here to perform an order-of-magnitude analysis for the radial motion of tracer particles within a Lamb-Oseen vortex model with core radius $r_c = 2.5$ mm and maximum

tangential velocity $U_{max} = 10$ m/s (at $r = r_c$). These conditions mimic those encountered in the present experiments with a free stream velocity $U_{inf} = 10$ m/s (see Section 4). Fog droplets with a density of 1000 kg/m^3 ($\bar{\rho} \cong 830$) and $1 \text{ }\mu\text{m}$ in diameter are taken for reference of typical tracers employed in PIV. Helium filled soap bubbles of $300 \text{ }\mu\text{m}$ diameter and five different buoyant conditions are considered following the previous work described in chapter 5. Figure 6.5 shows the radial distribution of the slip velocity for the chosen tracers. Despite the HFSB are two orders of magnitude larger than fog droplets, their low density allow them to recede from the vortex centre with a velocity comparable to the fog droplets. The results indicate that HFSB with a control of their neutral buoyancy within 1% ($|\bar{\rho}| \approx 0.01$) yield the same radial slip as the fog droplets. The cases of Helium-filled-soap-bubble within 0.5 and 5% departure from neutral buoyancy ($|\bar{\rho}| = 5 \times 10^{-3}$ and $|\bar{\rho}| = 5 \times 10^{-2}$) are illustrated in the example. Close to the neutral buoyancy condition HFSB have not only similar behaviour than the micro-size droplets, but most importantly, the lighter-than-air tracers exhibit a negative (centripetal) drift velocity. As a result tracers are expected to accumulate towards the vortex axis where the concentration is maintained high.

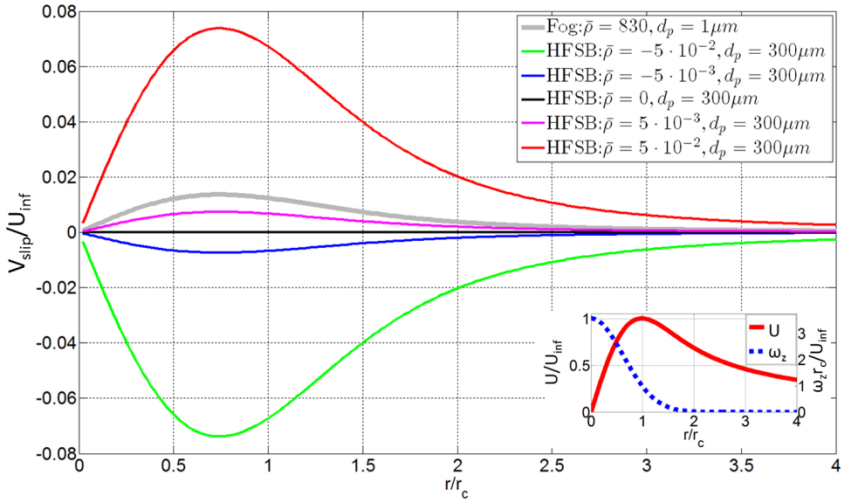


Figure 6.5 - Tracer slip velocity for different seeding particles, with radial profiles of dimensionless velocity of the flow, U , and vorticity, ω_z , for a Lamb-Oseen vortex.

6.2.1 Pressure distribution on HFSB of finite size

Let us consider conservatively a particle tracer of $400 \mu m$, a free stream velocity of 30 m/s and $U_{t_max} = U_{inf}$. The diameter of the vortex is assumed to be 5 mm . Let us now take the case of a bubble placed at the location of the maximum pressure gradient (dashed blue line in Figure 6.6). The tracer will experience a maximum pressure difference along its circumference of $10\% p_{core}$, being p_{core} the pressure minimum at the center of the vortex. The pressure force F_p , computed from the pressure distribution around the bubble with equation 6.6, is compared in Figure 6.7 with the pressure force, F_p' , calculated with the expression and reported in equation 6.7:

$$\mathbf{F}_p = \iint p \cdot \mathbf{n} dS \quad (6.6)$$

$$\mathbf{F}_p' = \frac{\pi}{6} d_p^3 \rho_f \frac{U_t^2}{r} \quad (6.7)$$

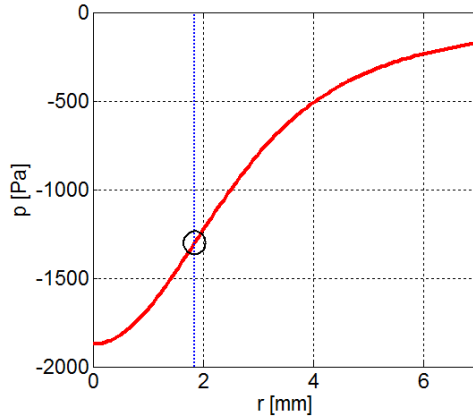


Figure 6.6 - Pressure distribution in a Lamb-Oseen a vortex of 5 mm diameter with $U_{t,max} = 30$ m/s and location of the maximum pressure gradient (dashed line).

When the tangential velocity is computed as the value at the center of the bubble, U_c (as it was computed in the article), a difference between F_p and the centrifugal force of 0.5% is retrieved, (in the present case $d_b/R_0 = 0.16$), as it is shown in Figure 6.7-left. The difference with F_p is even lower if the tangential velocity is computed as the mean square value in the region occupied by the bubble, $\overline{U_t^2}$ (the results are shown in Figure 6.7-right). The numerical simulations show that the pressure forces computed as in the article can be considered valid even for relatively large bubbles of with an approximation of 0.5%.

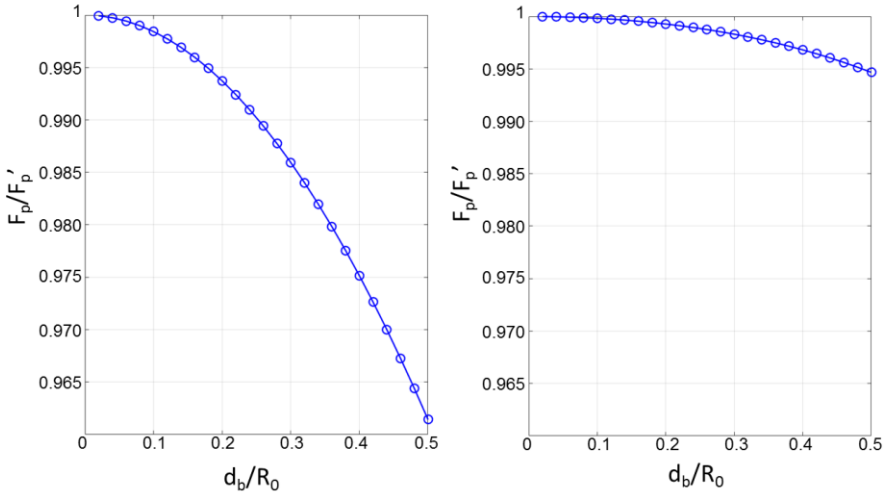


Figure 6.7 - Left: Ratio of the pressure force calculated from the pressure distribution around the bubble and the pressure force calculated from equation 6.7 using the U_i at the centre of the HFSB. Right: Ratio of the pressure force calculated from the pressure distribution around the bubble and the pressure force calculated using the mean square of tangential velocity computed in the region occupied by the bubble, $\overline{U_t^2}$.

6.3 Experimental apparatus and measurement procedure

The experiments are conducted in a low-speed open test section wind tunnel (W-Tunnel) of the Aerospace Engineering aerodynamic laboratories of TU Delft. The W-Tunnel features a test section of 40×40 cm² and the air-flow reaches 30 m/s with a turbulence level below 1%. A sharp-edge 76° swept delta wing is used with chord length of 300 mm. The model is made of acrylic glass (PMMA) and painted black to minimize the laser light reflections. The bottom side of the leading edge

is bevelled at 30° . Figure 6.8 shows the details of the model (left) and its installation at the exit of the wind tunnel (right) at 20° incidence and a free-stream flow velocity U_{inf} varying from 10 to 30 m/s. The blockage ratio generated by the model is 4.6%. The corresponding chord based maximum Reynolds number is $Re_c = 6 \times 10^5$.

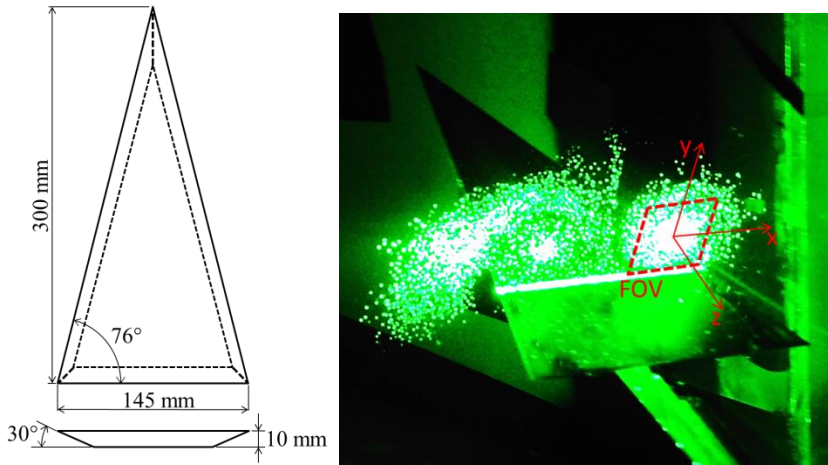


Figure 6.8 - Left: top and side views of the delta wing model. Right: experimental arrangement with the model installed at the wind tunnel exit. The field of view (FOV) of PIV measurements is indicated by red dashed lines. Time-averaged image of planar illumination using HFSB with lighter-than-air condition.

Laser sheet visualization is performed in a plane perpendicular to the surface of the delta wing that captures the entire vortex region at approximately 75% of the chord. A Photron *FastCAM SAI* camera (CMOS, $1,024 \times 1,024$ pixels, $20 \mu\text{m}$ pixel pitch, 5,400 fps) records the light scattered by the tracers from a distance of 2.4 m. The active area of the sensor is cropped to 512×512 pixels. At the set magnification of $M = 0.13$, the field of view is 15 cm and covers the wing span.

The imaging apparatus used for the stereoscopic-PIV makes use of two cameras of the same type as above. The cameras are equipped with 200 mm focal length Nikon objectives ($f_{\#} = 16$) mounted on Scheimpflug adapters. The angle between the cameras is set to 45° . A magnification factor ($M = 0.25$) yields a digital imaging resolution of 18.7 pixels/mm. The field of view captures the leading edge vortex on the right side of the wing. The coordinate system chosen for the present study is illustrated in Figure 6.8-right, with the z-axis along the model chord, the x- and y- axes along the span and wall-normal directions, respectively.

To determine the time-averaged scattering intensity of tracers, 40,000 images are recorded at 250 frames per second for each type of seeding. For the stereoscopic-PIV measurements, sequences of 40,000 double-frame images are acquired with time separation of $\Delta t = 60 \mu\text{s}$ for a free stream of 10 m/s and $\Delta t = 10 \mu\text{s}$ for a free stream of 30 m/s. The analysis of the stereoscopic recordings is carried out within LaVision *Davis* 8.3. Given the relatively high imaging signal-to-noise ratio yielded by the HFSB tracers and the absence of solid surface in the field of view, no image pre-processing was required for background intensity. The cross-correlation analysis is based on iterative multigrid window deformation. A starting window size of 96×96 pixels is selected and progressively refined to 32×32 pixels with overlap factor of 50%. The final vector pitch is 0.85 mm. The seeding density for the HFSB experiments is extremely low (typically no more than 10 particles are present in each recording). Therefore, the overall ensemble of 40,000 images has been analysed with the ensemble correlation algorithm (Meinhart *et al.* 2000).

6.4 Flow Seeding

The micro-size droplets are based on a water-glycol solution vaporized with a SAFEX fog generator. The mean droplets diameter is $1\ \mu\text{m}$ with a density of approximately $1000\ \text{kg/m}^3$. HFSB are generated by an orifice-type bubble generator similar to that described in chapter 3.

Generation of neutrally buoyant (NB), lighter-than-air (LTA), and heavier-than-air (HTA) bubbles relies on a dedicated adjustment of the flow rates of He and bubble fluid solution (BFS). The relaxation time of NB bubbles, used for PIV measurements, ranges between 10 and 30 μs , as it is measured in chapter 5. The size of the bubbles is mainly controlled by the air flow rate, and it is determined from the raw images measuring the distance between glare points. The latter procedure yields an estimate of the mean diameter of $300\ \mu\text{m}$. The uncertainty of the diameter estimation is approximately $30\ \mu\text{m}$ (see Figure 6.9).

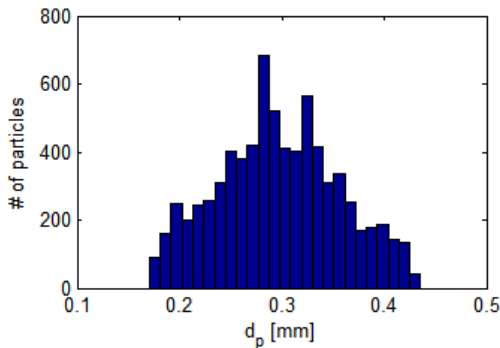


Figure 6.9 - NB-HFSB size distribution of the PIV measurements.

The fog generator is positioned upstream the fan of the wind tunnel to allow a homogeneous seeding distribution. Instead, the bubble generator is placed inside the settling chamber approximately 1.2 m upstream of the contraction and 2 m from the delta wing. An

assessment of the free-stream turbulence in the test section with the presence of the bubble generator yields practically the same level of rms fluctuations as with the empty settling chamber.

6.5 Tracers visualization within leading-edge vortex

Experiments conducted with laser sheet visualization aim at determining the tracer concentration in the vortex region above the delta-wing. The time-average scattered light intensity from microdroplets yields a rather uniform concentration with a clear deficit region centred on the axis of the vortex. The extent of the circular deficit region is approximately 5 mm in diameter (Figure 6.10-a). The latter corresponds approximately to the vortex core radius as discussed in the remainder. Increasing the free stream velocity from 10 m/s to 30 m/s does not alter the situation significantly (Figure 6.10-d). However, from instantaneous snapshots the deficit region slightly grows with the flow velocity (Figure 6.10-b, e), which is expected from the increase of the radial drift with the square of the tangential velocity.

The experiments conducted with HFSB in the nearly neutrally buoyant condition ($|\bar{\rho}| < 0.01$) also yield an overall uniform concentration of the tracers (Figure 6.10-c). Despite the large number of recordings, a fully uniform intensity is not achieved due to the small number of tracers (approximately 10) recorded in each image. The latter effect is more pronounced at higher flow velocity as the tracer's concentration scales inversely proportional to it (Figure 6.10-f), as it is documented in work of described in section 4.5.

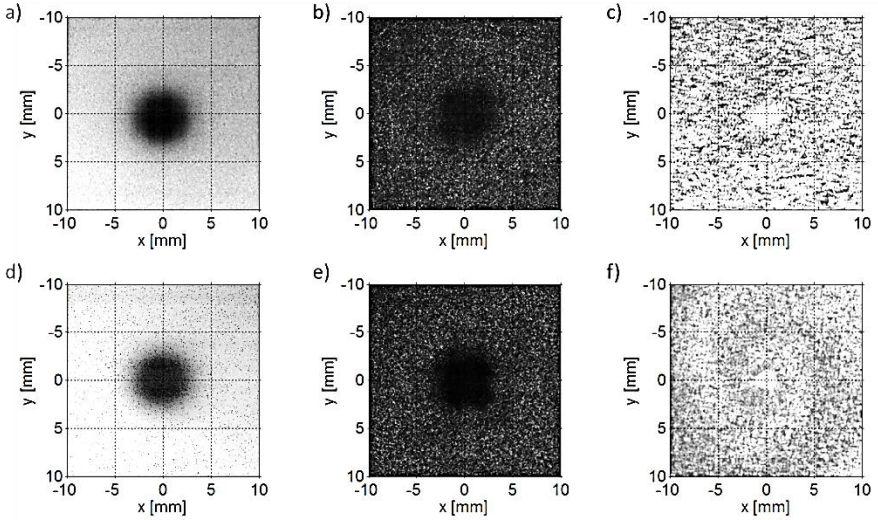


Figure 6.10 - Laser sheet visualization in the LEV: Time-average recorded intensity with fog at 10 m/s (a) and 30 m/s (d); Instantaneous particle images with fog at 10 m/s (b) and 30 m/s (e); Time average recorded intensity with HFSB at 10 m/s (c) and 30 m/s (f).

This result is consistent with equation 3, which states that tracers with density close to that of the fluid experience less radial drift than the fog droplets. Furthermore, a small increase of seeding concentration is found at the core axis (Figure 6.10-c,f). This is ascribed to the fact that even a fraction of the bubbles population with lighter-than-air weight will experience a negative radial force and associated motion, resulting in accumulation of tracers around the vortex axis.

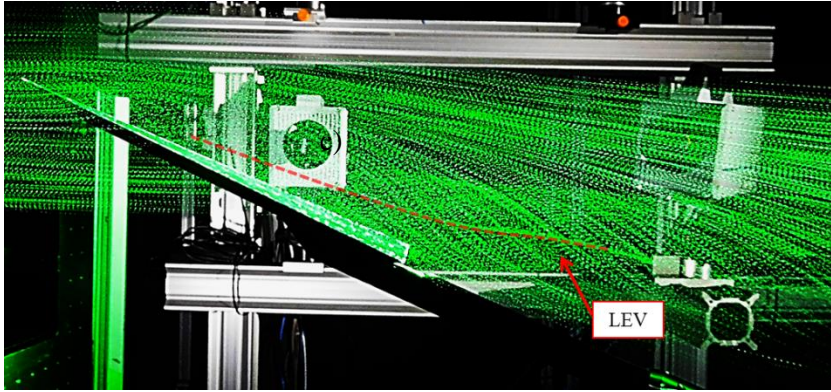


Figure 6.11 - Visualization of HFSB tracers pathlines by multiple-exposure image ($U_{inf} = 10$ m/s).

From a side view, the visualization of the tracers illustrates the presence of lighter-than-air tracers at the vortex axis resulting from their slight inward drift. Figure 6.11 shows a visualization of the tracers pathlines around the delta wing. The photograph is taken with exposure time of 5 ms, while the laser is firing at 1 kHz rate. The axis of the vortex where more particles accumulate is highlighted with a dashed red line. The continuous shape of the vortex axis indicates a quasi conical development of the vortex up till the trailing edge of the delta wing. Downstream, the vortex line bends upwards; towards the edge of the photograph, the inception of vortex breakdown is signalled by a sudden broadening of the tracers at the axis.

6.6 Velocity field in the vortex region

The time average velocity fields obtained with fog-droplets and HFSB are compared in Figure 6.12. The measurement conducted with micro-size droplets suffers from loss of correlation signal in the core region. The signal-to-noise ratio (SNR), defined in section 2.7, is well below a criterion for reliable velocity vector detection.

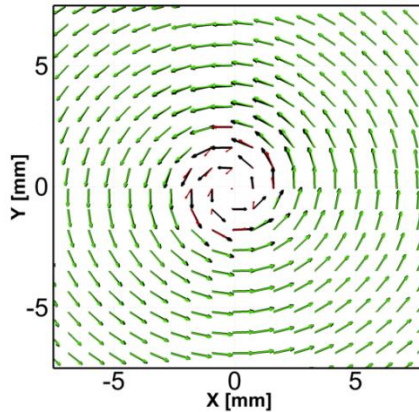


Figure 6.12 - Velocity vector field from measurements with HFSB and micro-size droplets at 10 m/s. Black vectors: HFSB; green vectors: micro-size droplets with SNR > 1.5; red vectors: micro-size droplets with SNR < 1.5.

In the core region the condition of SNR < 1.5 is verified and the estimates of the three velocity components are expected to be erroneous there. Outside of the core region, the measurements obtained with fog droplets follow with good agreement that of HFSB.

The contours of the time-averaged tangential velocity field, measured with micro-droplets and HFSB, are separately shown in Figure 6.13 at the two values of the free stream velocity. The distribution of the tangential velocity features the expected ring shape

and an annular region of maximum is observed at a radial distance of approximately 2.5 mm from the vortex axis. It is noted that only the inner part of the core differs between the measurements obtained with fog droplets and HFSB.

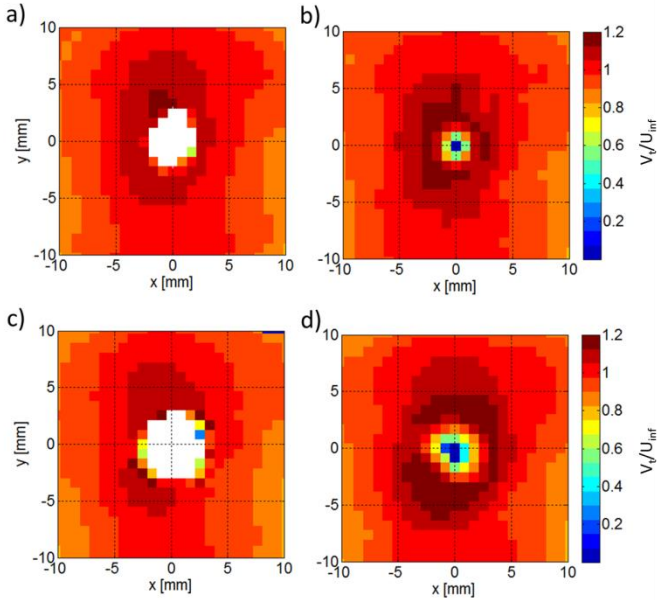


Figure 6.13 - Colour contours of time-averaged tangential velocity component. Fog droplets at $U_{inf}= 10$ m/s (a) and 30 m/s (c); HFSB at $U_{inf}= 10$ m/s (b) and 30 m/s (d).

In particular, the tangential velocity measured with fog droplets (Figure 6.13-a) exhibits several spurious measurement points ($SNR < 1.5$, masked in white) and the velocity does follow a linear distribution as expected and documented in literature (Nelson and Pelletier 2003). The above effects are more pronounced at higher velocity (Figure 6.13-c) due to the increased effect of particle centrifugation. The measurements from HFSB (Figure 6.13-b,d) return

a higher value of the maximum tangential velocity ($V_t = 1.2 U_{inf}$) as well as a well-defined vortex centre at velocity close to zero.

The axial velocity in the vortex region typically features a maximum or a minimum at the axis. This is reported as jet-like or wake-like behaviour of the vortex (Nelson and Pelletier 2003). Excess or defect of the axial velocity in the vortex core is an important property for predicting the occurrence of vortex breakdown (Escudier 1988). Therefore, the accurate measurement of the axial velocity and its streamwise development is relevant to the study of vortex dominated flows. In the present case, a jet-like distribution is expected in the core of the vortex, which is revealed with the measurements done with HFSB (Figure 6.14-b). A self-similar behaviour is observed when the axial velocity is normalized with the free-stream value (Figure 6.14-b,d). The non-linear distribution of the axial velocity makes it impossible to estimate it from spatial interpolation of the values in the neighbourhood of the vortex axis, which is the typical case when dealing with data drop-out in the centre region of the vortex (Figure 6.14-a,c). The axial velocity peak value obtained with the HFSB measurements is approximately twice the free stream velocity, which agrees well with the previous experimental results reported by Nelson and Pelletier (2003).

A quantitative inspection of the velocity distribution in the vortex core region is presented by velocity profiles extracted across the vortex axis ($y = 0$ mm). The distribution of the tangential velocity features the characteristic antisymmetric shape with a quasi-linear region around the centre and two opposite extrema that identify the edge of the vortex core (Figure 6.15-top). The core radius, defined as half of the peak-to-peak distance, is estimated to be $r_c = 2.5$ mm.

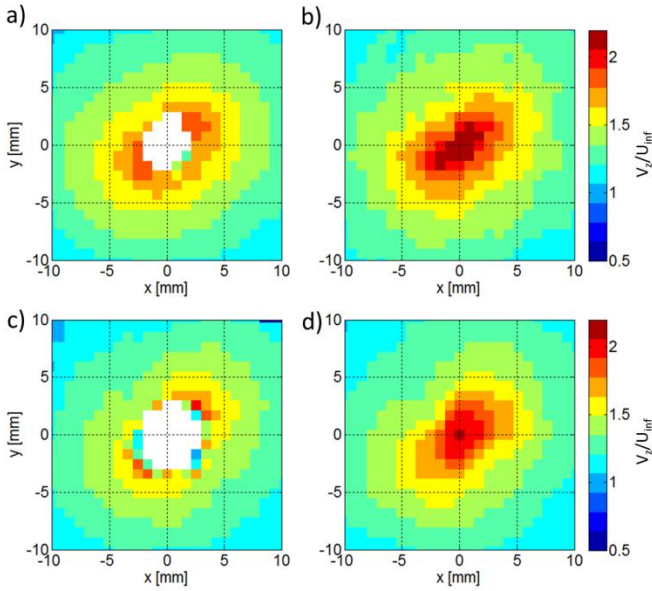


Figure 6.14 - Contour of the time-averaged axial component of the velocity for: a) fog at 10 m/s; b) HFSB at 10 m/s; c) fog at 30 m/s; d) HFSB at 30 m/s.

The peak value measured with fog slightly underestimates that returned with HFSB (by approximately 10%). Since the tangential velocity follows a linear distribution within the vortex core, the lack of signal caused by the fog tracers has limited consequences on the accuracy of this component. In fact, the tangential velocity in the vortex core could be evaluated by linear interpolation of velocity values at the edge of the core. The uncertainty stems from the underestimation of the peak value and its offset from the actual position.

Conversely, the absence of seeding has a non-negligible effect in the axial velocity component, where the lack of signal precludes the accurate estimation of the velocity peak, as it is shown in Figure 6.15-bottom. Neither a spatial interpolation can be used to alleviate the strong bias (underestimation) that affects the axial velocity. Outside of

the vortex core the good correspondence between HFSB velocity and that of fog droplets confirms the adequacy of the former as aerodynamic tracers.

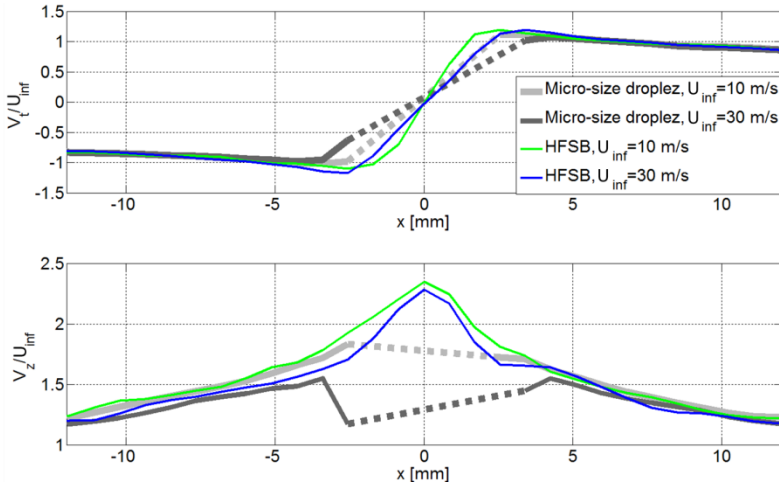


Figure 6.15 - Time-averaged velocities for different seeding particles at $U_{inf} = 10$ m/s. Top: tangential velocity. Bottom: axial velocity.

6.7 Discussion

The use of neutrally buoyant or slightly buoyant HFSB is proposed as a possible approach to solve the problem of lack of tracer particles in the vortex core precluding detailed velocity measurements by particle image velocimetry. The particles density relative to that of the air is the key parameter that determines whether the tracer particles are centrifuged outside of the vortex or accumulated at its centre. Experiments conducted on the leading edge vortex of a slender delta wing assess the capability of HFSB to populate the vortex core.

Neutrally buoyant HFSB appear distributed rather homogeneously within the leading edge vortex region. In contrast fog droplets are visibly centrifuged outside the vortex core and produce a “black hole”. As a result, the correlation signal-to-noise ration obtained using fog droplets as tracers for stereo-PIV suffers from drop-out in the vortex core. The problem is circumvented with neutrally buoyant HFSB that yield a reliable velocity measurement in the vortex core as well as in the outer region.

The experiments illustrate that HFSB tracers exhibit some dispersion in their density, resulting in a population that spans tracers from the condition lighter-than-air to heavier-than-air. The former component tends to accumulate at the vortex axis and may be considered advantageous for the LEV visualization as they allow real-time inspection of the presence and location of vortex and the onset of vortex breakdown.

7

OPTICAL CHARACTERIZATION OF HFSB

7.1 Introduction

Chapter 3 has introduced the main differences between the light scattered by HFSB with respect to micro-size droplets. The bubbles have size of the order of 300 μm and are constituted by two phases, which include a thin spherical shell of bubble fluid solution (BFS) and the inner volume of helium. This peculiarity of the HFSB poses open questions on the scattering properties of these seeding particles. The objective of the present chapter is to quantify how much more intense the light scattered by HFSB is compared to the micro-sized droplets. The answer to this question will enable the determination of the size of the maximum measurement volume achievable with HFSB for given light source and imaging setup.

The optical behaviour of HFSB is modelled by geometrical optics and a ray tracing procedure determines the amount of light scattered by the particle and collected by the sensor. The principles of the ray tracing technique are summarized in chapter 3. The approximation provided by the geometric optics is good for particles with $x_m \gg 1$, in which the

light wave is treated as a bundle of rays that interact independently with different parts of the particle. After the determination of the total light scattered from the HFSB in all directions, it is possible to calculate the amount of light collected by the camera knowing the imaging distance and the solid angle determined by the aperture of the lens. This procedure is then experimentally assessed by quantifying the light intensity collected by a camera at a given distance from the particles. The measurements are conducted by illuminating the tracers with a laser beam and considering the amount of light collected by the camera in terms of counts.

The present work quantifies the recorded light energy as well as the scaling behaviour with the diameter of the bubbles. Additional observations on the angular dependence of the scattered light intensity are conducted that show a mild variation of the particle light intensity from back-scatter to side-scatter and more pronounced variation towards forward-scatter.

7.2 Adrian's formulation based on Mie theory

The scattering energy collected by the camera is calculated for the same image recording system using the formulation proposed by Adrian (1991) and reported in equation 7.1 and 7.2. Adrian documented with the Mie theory analysis that for a fixed wavelength of the incident light small particles, in the range of 1-10 μm , the energy collected by the camera sensor has a cubic dependence on the tracer. In the same study it was reported that as the particle size increases to the geometric scattering regime ($x_m > 50$), the energy collected by the sensor becomes proportional to d_p^2 , as it is summarized in Figure 3.4. An energy density of the light pulse of $E_i = 3 \text{ J/m}^2$ (laser pulse of 25 mJ and expanded to diameter of 9 cm), a magnification factor of $M = 0.35$ and a camera

aperture of $A=8 \text{ mm}^2$ (corresponding to an objective with $f=105 \text{ mm}$ and $f_{\#}=32$) were considered in order to calculate the total energy collected by the camera E_{fog} and E_{HFSB} . The object distance is set to $L_o=1 \text{ m}$.

$$E = \frac{E_i A \lambda^2}{L_o^2} \left(\frac{d_p}{\lambda} \right)^s \quad (7.1)$$

$$\frac{E_{HFSB}}{E_{fog}} = \frac{d_{HFSB}^2}{d_{fog}^3} \lambda \quad (7.2)$$

Considering a particle diameter of $d_{fog} = 1 \text{ }\mu\text{m}$ and $d_{HFSB} = 300 \text{ }\mu\text{m}$, the exponent s is 3 and 2 for oil droplets and HFSB, respectively. In the present configuration $E_{fog} = 5.0 \cdot 10^{-17} \text{ J}$ and $E_{HFSB} = 2.3 \cdot 10^{-12} \text{ J}$. The comparison shows that the HFSB are scattering 2×10^4 more light than the micro-size droplets.

7.3 Ray-tracing model for HFSB

The principles of geometrical optics consider incident plane waves, or equivalently, a multitude of discrete parallel rays. The propagation of individual rays is traced and the refracted and reflected components are defined using the Snell's law and Fresnel's equations (van de Hulst, 1957). The number of rays reaching the camera sensor can be determined for a given distance. The intensity collected by the sensor is the summation of the intensity of all light rays reaching it. The following assumptions are made, which greatly simplify the analytical solution of the problem:

- Incident radiation is parallel and uniform.

- The surrounding medium and the medium inside the HFSB are considered to have the same refractive index due to the optical similarity between air and helium. In fact, the difference of refractive index is below 0.1% (Chang and Dalgarno, 1965).
- The bubble fluid solution forming the shell is made of homogeneous, non-absorbing material.
- Polarization effects are not considered.
- All interfaces are optically smooth and geometric optics principles can be considered valid.
- The thickness t of the shell is comparable with the wavelength of the incident radiation, i.e., interference between the emerging rays should be considered, but in this preliminary work it is neglected for simplicity.
- For neutrally buoyant bubbles, the BFS thickness is at least a factor 1,000 smaller than the bubble radius (Morias *et al.*, 2016).

The incident light beam is assumed to be non-polarised to simplify the problem and to facilitate the computation of the closed-form analytical solution. The coordinate system is shown in Figure 7.1 and the origin is at the centre of the bubble. In the model the incident rays are parallel to the x -axis and θ is the angle between the exiting (reflected) ray and the positive x -axis; for instance, θ is 180° for the backscattering and 0° for forward scattering. The distance between the incident ray and the x -axis is defined as h . The angles that the incident, reflected and refracted rays make with respect to the normal to the interface are given as α_i , α_r , α_t , respectively. The coordinates (x, y) represent the position where the rays interact with the interface of the bubble. For every incident ray I_{in} , there are four rays that are reflected once by the interfaces of the bubble and those correspond to the one externally reflected I_{11} , the second-order refraction rays I_{12} , I_{21} , and I_{22} (see Figure 7.1). I_r is the first-order

refraction. These rays are the most energetic and for this reason the rays of higher order refraction were not considered.

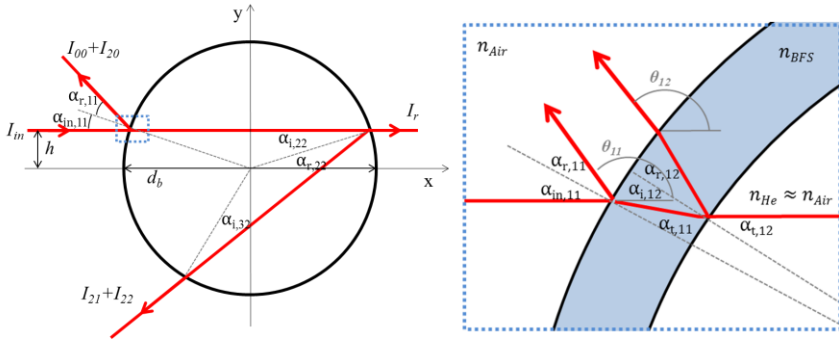


Figure 7.1 - Path of light rays through an HFSB.

The refracted angle is assumed equal to the incident angle due to the negligible thickness of the shell and the negligible difference in refractive index between helium and air. As mentioned in section 3.4 the reflections are specular. An incident ray I_i at location $y_{i1} = h$ intersects the bubble's surface at a point of coordinates:

$$x_{11} = -\sqrt{\left(\frac{d_b}{2}\right)^2 - y_{i1}^2} \quad (7.3)$$

$$y_{11} = h \quad (7.4)$$

For a given radius of HFSB r_1 and internal radius defined $r_2 = r_1 - t$ a simple geometrical analysis results in the following relations of incident angle and scattering angles:

$$\alpha_{i,11} = \arctan \frac{y_{11}}{x_{11}} \quad (7.5)$$

$$\alpha_{t,11} = \arcsin \left(\frac{n_{air}}{n_{BFS}} \sin(\alpha_{i,11}) \right) \quad (7.6)$$

$$\alpha_{i,12} = \arcsin\left(\frac{r_2}{r_1} \sin(\alpha_{t,11})\right) \quad (7.7)$$

$$\alpha_{t,21} = \arcsin\left(\frac{n_{air}}{n_{BFS}} \sin(\alpha_{in,21})\right) \quad (7.8)$$

$$\theta_{11} = \pi - 2\alpha_{i,12} \quad (7.9)$$

$$\theta_{12} = \theta_{11} + 2\alpha_{i,12} \quad (7.10)$$

$$\alpha_{i,22} = \alpha_{t,21} \quad (7.11)$$

The point (x_{I2}, y_{I2}) on the BFS-He interface can be found as the intersection between the line with angular coefficient $(\alpha_{i,11} - \alpha_{t,11})$ and the circle with radius r_2 . The equation of the rays I_{11} and I_{12} can be expressed in terms of the scattering angles θ_{I2} and θ_{22} and the coordinates of the interaction points. The equation of the rays I_{21} and I_{22} follows the ones indicated above (equation 7.5-7.11). The following equation for a generic light ray is obtained:

$$I_n: \quad y = \tan \theta_n (x - x_n) + y_n \quad (7.12)$$

Equation (7.12) gives the geometrical paths of the scattered rays. The light energies of the rays leaving the bubble are defined as:

$$E_{11} = E_i R(\alpha_{i,11}, n_{12}) \quad (7.13)$$

$$E_{12} = E_i \left(1 - R(\alpha_{i,11}, n_{12})\right) R(\alpha_{i,12}, n_{21}) \left(1 - R(\alpha_{t,11}, n_{21})\right) \quad (7.14)$$

$$E_r = E_i (1 - R(\alpha_{i,11}, n_{12})) (1 - R(\alpha_{i,12}, n_{22})) \dots \quad (7.15)$$

$$\dots (1 - R(\alpha_{i,21}, n_{21})) (1 - R(\alpha_{i,22}, n_{12}))$$

where R is the Fresnel reflection coefficient given in chapter 3. The subscript $I2$ in the relative refractive indices in equation 7.15 denotes the passage from air to BFS and vice versa. E_i is the amplitude of the incident ray which is 3 J/m^2 times k^2 , where k represents the ray spacing of the incident wave. In this case, it was assumed $k = 50 \text{ nm}$.

In order to study the detectability of the HFSB, the model has to consider the imaging setup. A lens with aperture area A is placed at a

distance L_0 from the helium-filled soap bubble. The schematic of the image recording system in Figure 7.2 contains the directions of incidence and of scattering. The amount of light scattered within the solid angle $\Omega = A/L_0^2$ is collected by the sensor of the camera.

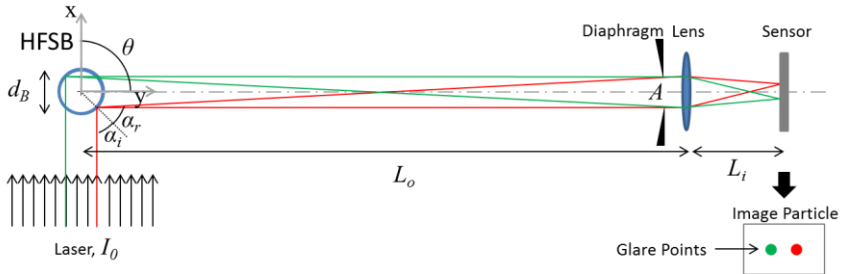


Figure 7.2 - Image recording system for a scattering angle $\theta = 90^\circ$. Dimensions not in scale.

7.3.1 Numerical Assessment

In the present section, the ray tracing model is assessed via computer simulations. The total energy collected by the camera, E_{HFSB} , was calculated using the optical configuration described in section 7.2. The results obtained with the ray tracing model show the quadratic scaling behaviour of the recorded light energy scattered by a HFSB with the bubble diameter (see Figure 7.3). The angular dependence of the scattered light intensity for a HFSB is shown in Figure 7.4 for a bubble size of $d_b = 300 \mu\text{m}$. The order of magnitude of the intensity is not changing from the forward to the back scattering, which is the major difference in respect to the case of micro-size particles in the Mie scattering range. A minimum is reached in side scattering; in back scattering the light intensity increases by 10%, while in forward scattering it increases by 25%.

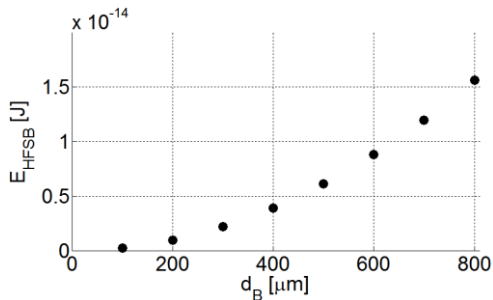


Figure 7.3 - Numerical scaling behaviour of the recorded light energy, E_{HFSB} , scattered by HFSB with the bubble diameter for the scattering angle of $\theta = 90^\circ$.

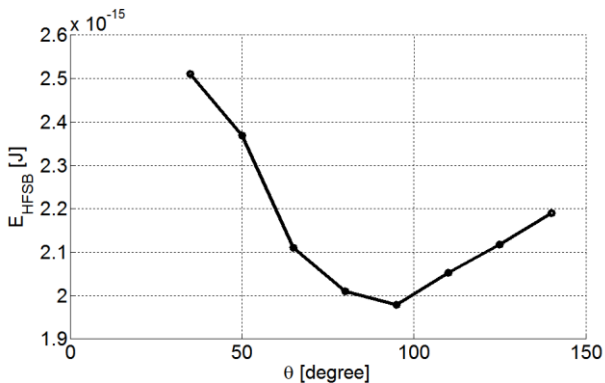


Figure 7.4 - Angular dependence of the scattered light intensity for a HFSB with $d_b = 300 \mu\text{m}$.

7.4 Experimental approach

The above numerical model is validated with an experimental investigation conducted in the Aerodynamics Laboratory of TU Delft. The measurement compares the energy scattered in to the camera from HFSB and micro-size droplets.

7.4.1 Experimental apparatus and setup

The experimental assessment is performed using a Quantronix *Darwin Duo* Nd:YLF laser (2×25 mJ at 1 kHz), a LaVision Imager LX 2MP camera (1628 x 1236 pixels, with 4.4 micron pitch) with an $f = 105$ mm Nikon objective. The optical magnification is approximately $M = 0.35$ and the extent of the field of view is 1.5×2 cm². Figure 7.5 illustrates the arrangement of the light beam, the tracers, and the camera. The lens aperture is set to $f_{\#} = 2.8$ for the imaging of the micro-size droplets. The imaging of HFSB is performed with an aperture of $f_{\#} = 32$ in order to avoid image saturation.

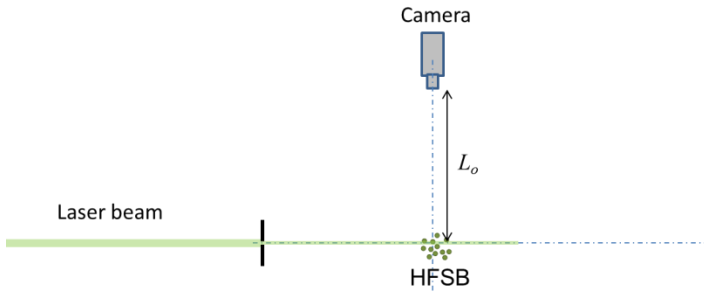


Figure 7.5 - Experimental setup.

A spherical lens is used to expand the laser light into a beam of approximately 9 cm diameter. A beam slit was used to cut the beam into a sheet of 2 mm thickness as it is shown in Figure 7.5. In this way uniform illumination intensity was achieved in the measurement volume. The HFSB generator was fed by constant flow rates of helium, BFS, and air through the fluid supply unit described in chapter 4. The HFSB are injected in the field of view with two different conditions to produce different size ranges of bubbles. The pressure in the feeding line of the soap fluid was varied as reported in Table 7.1.

Table 7.1 Fluid Pressure for HFSB production during the experiment

	He [bar]	Air [bar]	BFS [bar]	Mean d_{HFSB} [μm]
Run001	2	2.2	2.1	350
Run002	2	1.5	2.1	600

In Run001 the bubbles have an average radius of 350 μm . In Run002 a higher bubble radius is obtained reducing the air flow rate.

7.4.2 *Image processing*

Image acquisition is performed using the LaVision Software DaVis 8.1; the raw images are processed in Matlab R2012b. The bubble images feature two glare points as discussed in chapter 3. The total energy collected by the camera from the bubbles is measured by summing the total amount of *counts* from both the glare points of each individual bubble. Figure 7.6 shows the bubble images for a typical recording. The coloured circles represent the region in which the pixel counts are summed up. The circles of the same colour identify the glare points of the same bubbles.

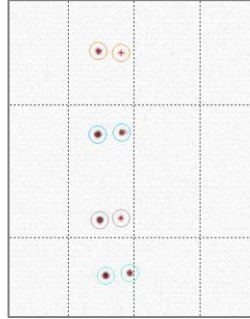


Figure 7.6 Raw image with inverted grey scale. The circles of the same colour identify the glare points of the same bubbles.

The total amount of counts is converted into total energy collected by the camera considering that every count corresponds to 1 eV (1.6×10^{-19} J) and taking into account the quantum efficiency, η_{QE} , of the sensor (59%):

$$E_{HFSB} = \frac{\# \text{ counts}}{\eta_{QE}} 1.6 \cdot 10^{-19} \quad (7.22)$$

7.4.3 Results and comparison with the ray-tracing

A comparison between raw images of fog droplets (a) and HFSB (b) with a mean diameter of 300 μm is shown in Figure 7.7. The total energy scattered by individual tracers and captured by the imaging system is computed integrating the total counts over the pixels occupied by the particle image. Both glare points are considered for HFSB. The comparison between the two different tracers is performed taking in consideration the two different apertures of the camera lens using a scaling factor defined as the ratio of the two apertures A_1/A_2 . The resulting values are shown in Table 7.2. The comparison between the two seeding particles shows that the energy collected by the camera

from the HFSB is 10^4 higher than the one collected by the fog particles. This value is in agreement with the theoretical model retrieved with the formulation of Adrian in section 7.2.

Table 7.2 Light intensity of HFSB and fog particles.

	$d_p[\mu\text{m}]$	# counts	$f_{\#}$	A [mm^2]	# counts / A [mm^{-2}]
HFSB	300	10,300	32	8	1,300
Fog particles	1	200	2.8	1400	0.14

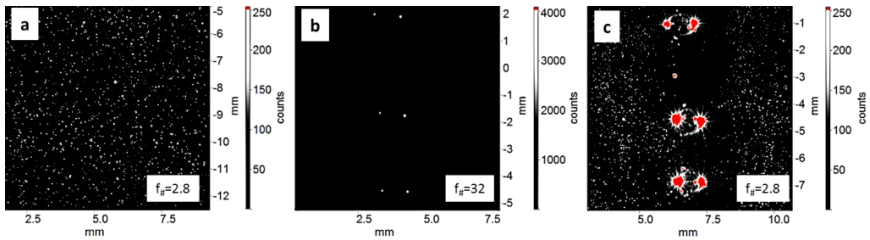


Figure 7.7 - Particle images of fog droplets (a), HFSB (b), fog droplets and HFSB (c) at different $f_{\#}$.

The light intensity scattered by the HFSB is measured and it is in relatively good agreement with the ray tracing algorithm developed in the present chapter. The scattering intensity shows a monotonic increasing behaviour with the bubble diameter. A significant dispersion of the collected intensity is observed for bubbles larger than $400 \mu\text{m}$. The reason is ascribed to the *jetting* regime working of the bubble generator, as it is described in section 4.3. The experimental results are averaged within ‘bins’ determined by the size of the bubbles, in this case, every $20 \mu\text{m}$. F

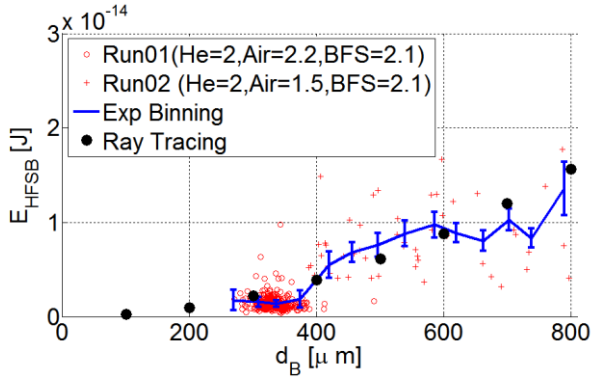


Figure 7.8 - Experimental assessment of the quadratic behaviour of the scattering energy compared with the results of the ray tracing.

The angular dependence of the scattered light intensity for HFSB is shown in Figure 7.9. The results of the ray tracing model and measurements are in good agreement. They both show that the light scattered by the bubbles is minimum in side-scattering, $\theta \approx 90^\circ$, and higher in forward- and back-scattering. This behaviour is similar to the one of micro-size particles, as it is shown in Figure 3.4. It is noticed that the variation of the light intensity with respect to the scattering angle is much lower for HFSB. For micro-particles, the change of intensity of the scattering light can be of several order of magnitude passing from side- to forward-scattering.

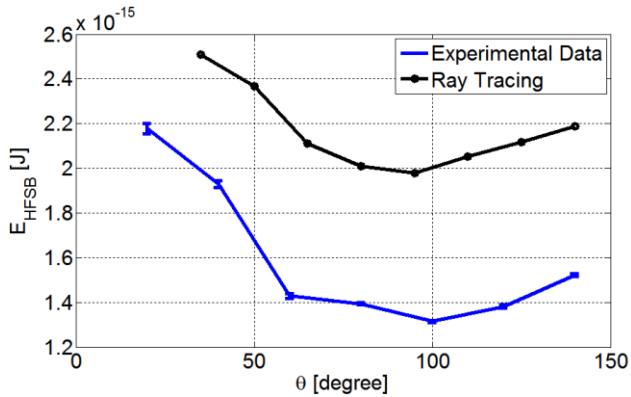


Figure 7.9 - Experimental assessment of the angular dependence of the scattered light intensity for a HFSB compared with the results of the ray tracing.

7.5 Implications on the measurement volume size in PIV experiments

The comparison between the light scattered from HFSB and micron-size oil droplets allows the determination of the maximum measurement volume in terms of detectability of the tracers by the camera sensor. As discussed in chapter 4, the measurement volume in tomo-PIV experiments depends also on the distribution of seeding in the test section of the wind tunnel; however, in this section only the parameters related to the imaging of the particles are considered, in particular the scattering properties of the tracers, the intensity of the illumination and the solid angle determined by the aperture of the lens.

The effect of reduced tomographic reconstruction quality when increasing the depth of the measurement volume (due to the increase of the ppp, particles per pixel) is not accounted for. The general

formulation to retrieve the light energy collected by the camera (Adrian, 1991) is shown in equation 7.24 where the aperture of the camera A is expressed as a function of $f_{\#}$:

$$E = \frac{I_0 \lambda^2}{\Delta Z \Delta Y L_o^2} A \left(\frac{d_p}{\lambda} \right)^5 \quad (7.23)$$

$$E = \frac{I_0 \lambda^2}{\Delta Z^2 L_o^2} \frac{\pi}{4} \left(\frac{f}{f_{\#}} \right)^2 \left(\frac{d_p}{\lambda} \right)^5 \quad (7.24)$$

I_0 is the energy released by the laser pulse and ΔZ^2 represents the cross section of the laser beam in the measurement volume which is assumed as a square area. The $f_{\#}$ of the objective, in a PIV experiment, must be chosen according to the size of the illuminated volume along the viewing direction ΔZ . In order to avoid out-of-focus particles in the illuminated region, the depth of focus δZ should equal ΔZ (see section 2.5). For this reason, $f_{\#}$ was obtained from equation 2.9 and substituted in equation 7.24:

$$E = \frac{I_0 \lambda^2}{\Delta Z^2 L_o^2} \frac{\pi}{4} f^2 \frac{4.88 \lambda}{\Delta Z} \left(\frac{M+1}{M} \right)^2 \left(\frac{d_p}{\lambda} \right)^5 \quad (7.25)$$

The present formulation consider an objective of $f=50$ mm, a magnification factor of $M=0.05$, an object distance of $L_o=1$ m, and a light with wavelength of $\lambda=530$ nm. The cross section of the illuminated volume ΔZ^2 can be obtained from equation 7.25 keeping the energy collected by the camera constant. The energy E_{HFSB} measured from the experimental campaign for the HFSB of 300 μm diameter is used as reference. The variation of ΔZ^2 as a function of the bubble size is expressed as:

$$\Delta Z^2 = \left(\frac{I_0}{E_{HFSB} L_o^2} \frac{\pi}{4} f^2 4.88 \lambda \left(\frac{M+1}{M} \right)^2 d_b^2 \right)^{\frac{2}{3}} \quad (7.26)$$

Equation 7.26 shows that the size of the laser beam does not scale simply with d_b^2 . The increment of the illuminated area needs a reduction of the camera aperture to ensure in-focus particles. As a result, ΔZ^2 increases with a lower order as $d_b^{4/3}$.

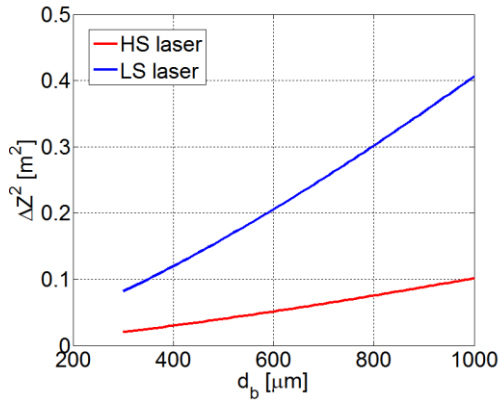


Figure 7.10 - Cross section of the illuminated volume as function of the HFSB size for two light source: $I_0=25$ mJ (High-Speed laser) and $I_0=200$ mJ (Low-Speed laser).

Figure 7.10 shows the variation of the measurement volume in two cases. In the first one, a high-speed laser is chosen as a light source with a pulse energy of $I_0=25$ mJ, corresponding to the Quantronix Darwin Duo 527-80-M. In the second case, a more powerful laser is considered, as in the case of low-speed lasers. In this example a value of $I_0=200$ mJ is used, as for the Quantel Evergreen 200. For typical bubble diameter of $400 \mu\text{m}$, a linear cross section size of 15 cm and 33 cm is achieved with high-speed laser and low-speed laser, respectively.

8

USE OF HFSB IN LARGE-SCALE MEASUREMENTS

Part of the material presented in this chapter is published in the article “On the use of helium-filled soap bubbles for large-scale tomographic PIV in wind tunnel experiments”, from F Scarano, S Ghaemi, GCA Caridi, J Bosbach, U Dierksheide, A Sciacchitano, *Experiments in Fluids* 56, 2015; and in the article “Helium-filled soap bubbles for vortex core velocimetry”, from GCA Caridi, A Sciacchitano, F Scarano, *Experiments in Fluids* 58, 2017.

8.1 Introduction

The work presented in this chapter explores the use of HFSB in large-scale measurements for different aerodynamic applications. In particular, the experiments described in the following section show examples where the use of HFSB yields an advantage with respect to PIV measurements with conventional seeding, meaning micro-size droplets. The first example reported hereafter is based on the measurement of a cylinder wake flow, which represents: 1) the first volumetric measurement conducted with HFSB in a wind tunnel; 2) an experimental assessment of the tomo-PIV technique in combination of the first HFSB seeding system for wind tunnels. The other cases reported cover different

types of aerodynamic problems that are more pertinent to the interests of industry. The flows analysed are at high Reynolds number and fully 3D. In particular, the cases under study include the visualization and quantification of large structures in the rotor region of a vertical axis wind turbine (VAWT) and the analysis of the entire landing deck of a frigate. Finally, the discussion stemming from the analysis of the results puts in evidence some current limitations of the use of HFSB and possible solutions.

8.2 Circular cylinder wake flow

8.2.1 *Experimental setup*

The model is a smooth cylinder of 4.5 cm diameter, placed horizontally at the wind tunnel exit. The dedicated seeding system used in the experiment is described in the section 4.5. The tracers within a stream-tube follow the contraction along the wind tunnel nozzle resulting in a final stream-tube of approximately $20 \times 20 \text{ cm}^2$ cross section. Based on particles images count, a concentration of approximately 1 particle/ cm^3 is achieved at wind tunnel speed of 5 m/s. The laser beam is expanded to illuminate a volume of approximately $40 \times 12 \times 20 \text{ cm}^3$. The recordings are taken at 2 kHz. Three cameras compose the tomographic imaging system. The optical magnification is approximately $M = 0.09$ and the extent of the observed region is $20 \times 20 \times 12 \text{ cm}^3$ (Figure 8.1). A lens aperture set to f/32 yields images in focus over the entire depth. Under these conditions, images were recorded with a particle density of approximately 0.006 ppp (6,000 particles/Mpixel) and the typical particle peak intensity was 300 counts. The background noise was approximately 10 counts. Although, large-scale tomographic particle image velocimetry has been used for the evaluation of the flow structures of turbulent convective air flow in an rectangular convection cell (Kühn *et al.*, 2011),

according to a recent survey (Scarano 2013), this is the first experiment realized in a wind tunnel with time-resolved tomographic PIV over a volume of approximately 4800 cm^3 .

A typical recording is shown in Figure 8.2, where a detail of the tracers images is displayed. Due to the low magnification factor, the glare points are imaged with a separation of 1-2 pixels. Diffraction causes the particle image diameter to exceed 2-3 pixels. As a result, no double intensity peak is observed.

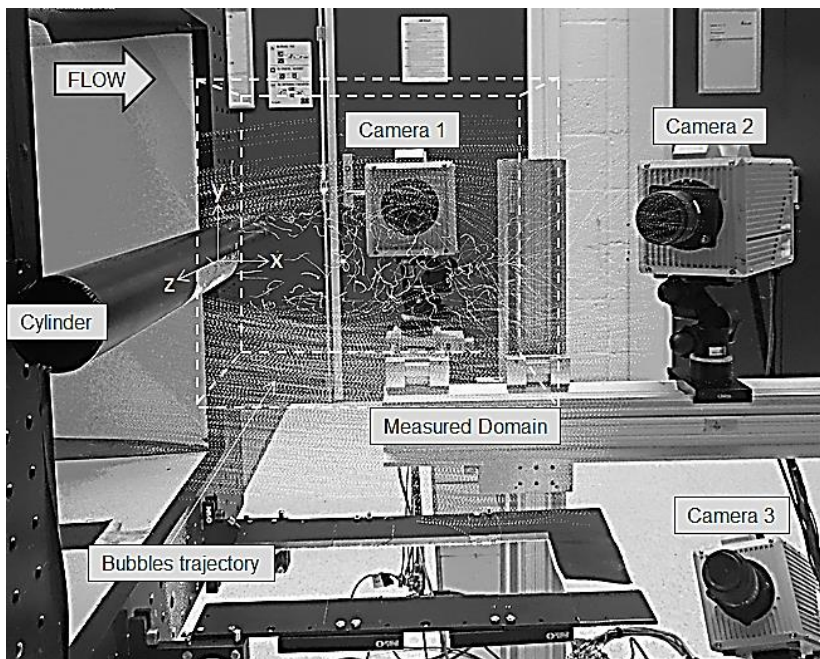


Figure 8.1 Setup of tomographic PIV system, with cylindrical model, 3-cameras imaging and indication of measured domain.

The distribution of light along the volume depth is given by the reconstructed light intensity. Integrating the intensity over 300 objects, one obtains the result shown in Figure 8.3. Each point of the profile is

obtained summing up values belonging to the entire plane of voxels at the same z -coordinate. The ratio of intensity inside and outside the illuminated region is indicative of the reconstruction signal-to-noise ratio SNR_R . For the present experiment, it was measured a $SNR_R = 60$ (Figure 8.3). Based on a recent experimental characterization of tomographic reconstruction accuracy (Lynch and Scarano 2014), such level of SNR_R implies that the ghost particles velocity does not affect the velocity estimates from cross correlation (Elsinga *et al.*, 2006).

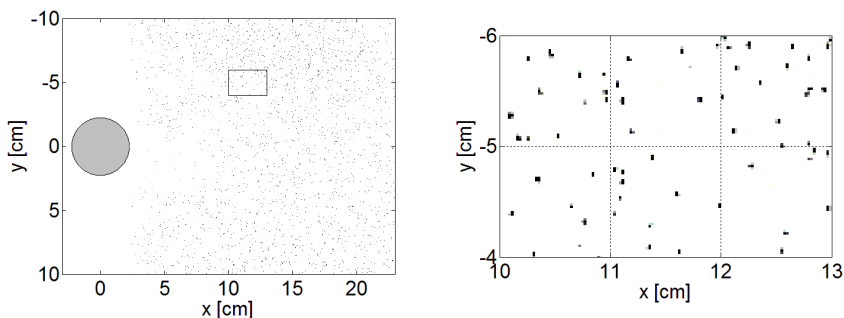


Figure 8.2 - Left: raw image from camera 1 (intensity with inverted colours). Right: detail of particle images.

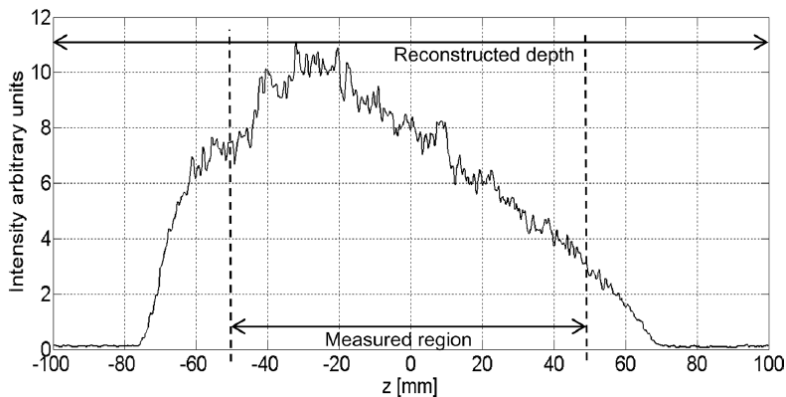


Figure 8.3 - Spanwise-profile of reconstructed intensity light. Dashed lines indicate depth of the measured volume.

8.2.2 *Instantaneous velocity field*

The tomographic data analysis is performed with LaVision software Davis 8.2. Before volume reconstruction, standard image pre-processing for tomo-PIV is conducted, which consist of image background elimination via minimum subtraction and Gaussian filter to regularize the particle image intensity distribution. The domain is discretized into $1000 \times 1000 \times 500$ voxels and reconstructed with the MART algorithm using the Fast-MART approach. The objects are interrogated with correlation blocks of $96 \times 96 \times 86$ voxels ($2.1 \times 2.1 \times 1.9 \text{ cm}^3$) and 75% overlap factor, with a sparse direct correlation algorithm (Discetti and Astarita 2012), yielding a measurement of $50 \times 50 \times 24$ vectors with a grid spacing of 5 mm.

The resulting vector field is post-processed with the universal outlier detection (Westerweel and Scarano, 2005) and filtered with a 2nd order polynomial in the time domain with a kernel of 7 snapshots. Figure 8.4 illustrates the results in terms of velocity vectors and z-vorticity contours at the plane corresponding to $z=0$. The sequence illustrates the spatio-temporal development of the *Kármán Street* composed of counter-rotating vortices shedding from the rear side of the cylinder.

The limited spatial resolution, mostly due to the sparse seeding, does not allow to resolve the thin shear layer prior to the vortex roll-up, as well as the turbulent sub-structures such as the *ribs* or *fingers* reported in previous tomographic experiments on the same geometry (Elsinga *et al.* 2006, Scarano and Poelma 2009). In the three-dimensional snapshot represented in Figure 8.5 the iso-surface of vorticity magnitude reveals both shear layers developing from the cylinder surface. The cross-correlation signal-to-noise ratio (Keane and Adrian, 1992) typically exceeds 2.5 in the outer region, while it drops to 1.4 in the near wake region as a result of the lower tracers concentration.

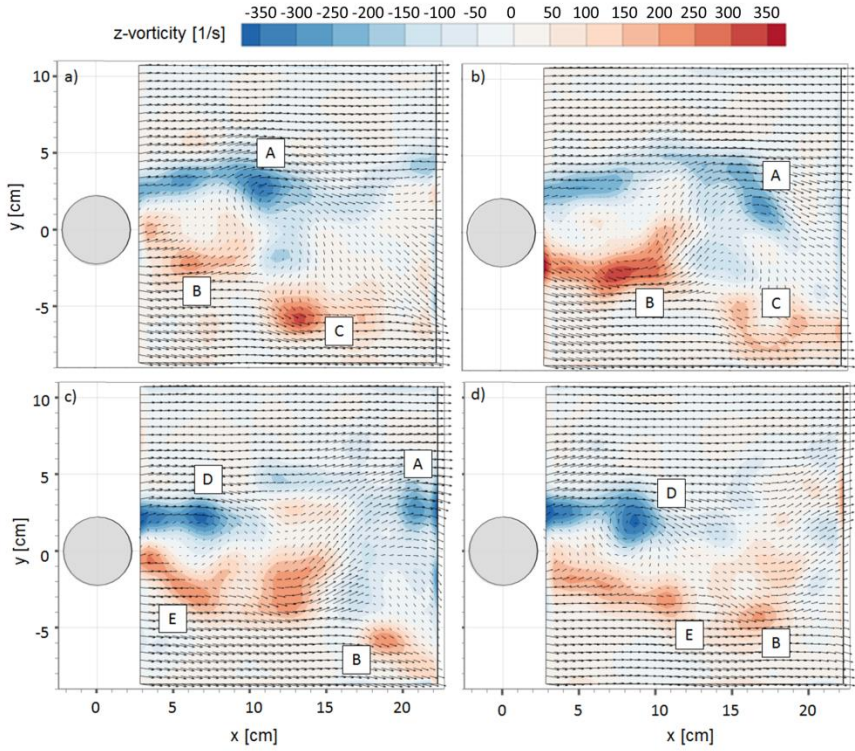


Figure 8.4 - Spanwise vorticity contour at four time instants: a) $t = 0$ ms, b) $t = 15$ ms, c) $t = 30$ ms, d) $t = 45$ ms (shedding period: $T = 60$ ms).

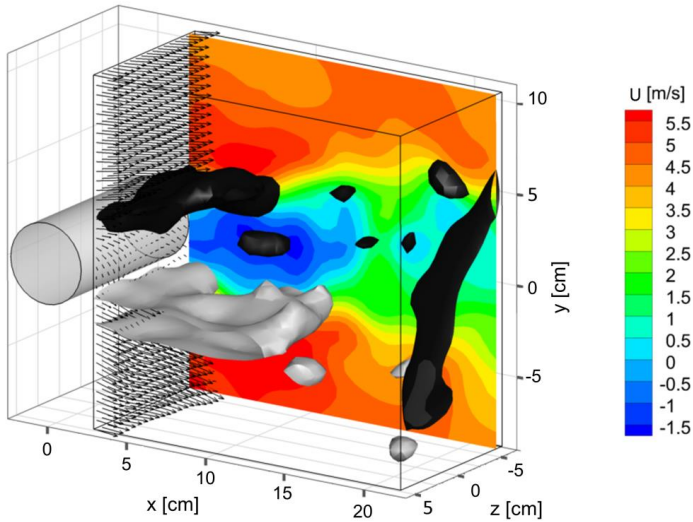


Figure 8.5 - Instantaneous velocity and vorticity distribution in the wake of the cylinder. Dark and light grey iso-surfaces correspond to spanwise vorticity of ± 300 1/s respectively.

8.3 Measurements in the rotor region of VAWT

The HFSB are used to study the dynamical evolution of the three-dimensional flow developing from the rotor blade tip of a vertical axis wind turbine (VAWT) of 1 m diameter and 1 m height. The measurements are taken at a rate of 1000 Hz in a volume of $40 \times 20 \times 15$ cm³, which allows following the blade passage and the associated tip-vortex formation, release and spatio-temporal evolution in the inner rotor region. The results obtained with tomographic PIV cross-correlation analysis are compared with the Tomo-PTV approach that follows the

VIC+ method (Schneiders and Scarano 2016) in relation to the tip-vortex peak vorticity.

8.3.1 Experimental setup

The measurements are conducted in the Open Jet Facility (OJF) of TU Delft. The wind tunnel features an open test section with closed-circuit. At the end of the contraction, the wind tunnel has an octagonal cross section of $2.85 \times 2.85 \text{ m}^2$. The air flow is driven by a 500 kW electric motor. In the test section, the free stream velocity can range from 3 to 35 m/s with a maximum turbulence intensity of 0.5%. The model is a two-blade H-shaped rotor VAWT of 1 m diameter (D).

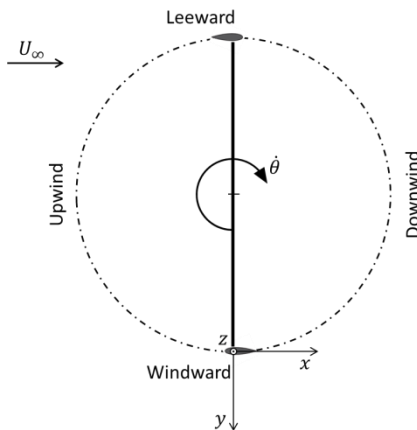


Figure 8.6 - System of reference and schematic of the blade motion on a vertical axis turbine.

The rotor blades are shaped following the NACA0018 profile with 6 cm chord length and installed with zero angle of attack. The blades are tripped by zig-zag stripes in order to force the boundary layer transition from laminar to turbulent regime. The blade span H is 1 m long, yielding an aspect ratio $AR = H/D = 1$. Measurements are conducted at free-stream velocity $U_\infty = 8.5 \text{ m/s}$ and rotational speed $\Omega = 800 \text{ rpm}$, yielding

a tip speed ratio $\lambda = 5$. The Reynolds number based on the chord length and the tangential velocity of the blades is $Re_c = 170,000$. The choice of the frame of reference and associated terminology follow the work of Tescione *et al.* (2014). The schematic from the previous authors is shown in Figure 8.6. The Cartesian coordinate system has its origin at the bottom surface of the blade and azimuthal angle $\theta = 0^\circ$ (windward position). The free-stream velocity is directed along x . The turbine rotates clockwise when seen from the top.

Figure 8.7 illustrates the arrangement of the seeding system and tomographic setup in the wind tunnel. The cylindrical reservoir is placed below the wind tunnel exit; the seeding injector was installed at the exit of the wind tunnel 2.5 m upstream of the VAWT model. A stream tube of tracers is released such that it flows around the bottom tip of the blade when it is at $\theta = 0^\circ$.

The turbulence intensity of the stream before it interacts with the wind turbine is assessed by dedicated measurements returning rms fluctuations below 2% of the free stream. The HFSB injected in the flow have an average diameter of approximately $300 \mu\text{m}$. The bubbles are generated in the same condition as it is described in chapter 4 and injected in the wind tunnel with the same technique used in the previous experiment presented in section 8.2. The only difference is that in this experiment the diffuser is installed downstream the contraction.

The tomographic PIV system consists of a Quantronix *Darwin Duo* Nd:YLF laser ($2 \times 25 \text{ mJ}$ at 1 kHz) and three Photron Fast CAM SA1 cameras (CMOS, $1,024 \times 1,024$ pixels, 12-bit and pixel pitch $20 \mu\text{m}$). The optical magnification is approximately $M = 0.05$ and the extent of the measured domain is $40 \times 20 \times 15 \text{ cm}^3$. The lens aperture is set to $f/11$ to ensure images in focus over the entire depth. Under these conditions, images are recorded with a particle density of approximately 0.004 ppp

(4,000 particles/Mpixel) and the typical particle peak intensity is 300 counts.

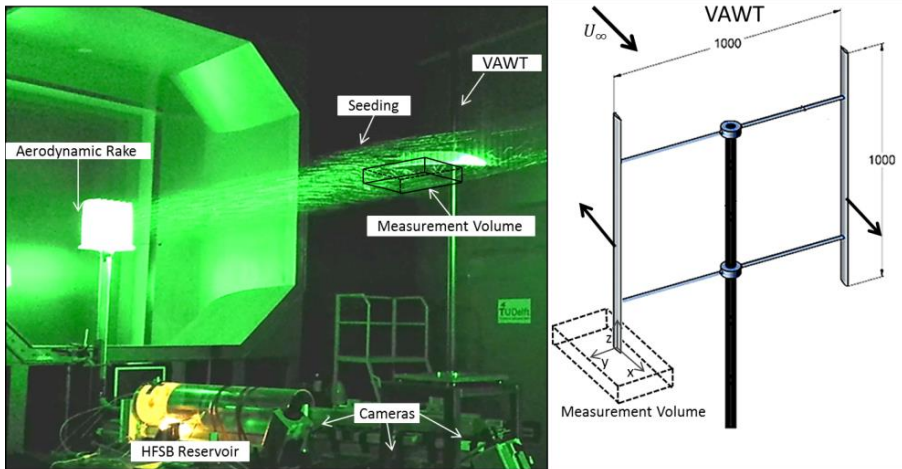


Figure 8.7 - Arrangement of the experimental set-up, with the HFSB released by the aerodynamic rake installed at the exit of the wind tunnel. Cylindrical reservoir, cameras and indication of the measured volume (left). Sketch of the VAWT with dimensions in millimetres (right).

Image pre-processing consists of image background elimination via minimum subtraction and Gaussian filter ($3 \times 3 \times 3$ pixels). The domain is discretized into $910 \times 814 \times 456$ voxels and reconstructed with 10 iterations of the fast MART algorithm. The objects are interrogated with correlation blocks of $80 \times 80 \times 80$ voxels ($3.3 \times 3.3 \times 3.3 \text{ cm}^3$) and 75% overlap factor, yielding $42 \times 35 \times 23$ vectors with a grid spacing of approximately 8 mm. The resulting vector fields are post-processed with the universal outlier detection algorithm (Westerweel & Scarano 2005). Moreover, Tomo-PTV analysis is performed on the same recordings in the vortex region to evaluate the effects of spatial resolution on the estimates of peak vorticity and vortex core diameter. The method is

based on the Vortex-in-Cell (VIC) technique, introduced by Schneiders *et al.* (2014), and it is used in the analysis of the peak vorticity for comparison with the cross-correlation-based results. The method is used to reconstruct velocity fields on a regular grid from volumetric particle tracking measurements. The time-resolved reconstructions, used for the tomographic PIV, are also used for a tomographic PTV analysis. The locations of the particles are identified with sub-voxel accuracy using a 3-point Gaussian fit. The 3D trajectories allow the determination of the velocity and acceleration through a second order polynomial fit along seven snapshots. The dense interpolation of the velocity from the sparse PTV-grid onto a regular one is made using an iterative minimization problem of a cost function that is proportional to the difference between the PTV measurements and the VIC+ results. The minimization is constrained by the incompressible flow assumption and the momentum equation in vorticity-velocity formulation. Due to their different dimensions, velocity and acceleration are scaled in the cost function by a factor α , which is chosen to be equal to the ratio of the typical magnitude of velocity and acceleration calculated from their root mean squared value. The VIC+ step is initialized using a uniform flow in the free-stream direction. The computational domain is chosen 30% larger than the measurement volume with constant boundary conditions based on the free-stream. The mesh spacing equal to 20 voxels. After the computation, the volume is cropped to the measurement volume and the exterior is not considered for data analysis. For full details of the VIC+ method, the reader is referred to Schneiders and Scarano (2016).

The recordings are acquired at 1 kHz, resulting into time-resolved information for the particle tracking technique. Figure 8.8 shows the particle image density for a typical recording. The quality of tomographic calibration and reconstruction is verified inspecting the reconstructed light intensity distribution along the volume depth (Figure 8.9). The profile, obtained from the average over 400 instantaneous objects, yields

a reconstruction signal to noise ratio (Lynch and Scarano, 2014) above 7 in most of the domain.

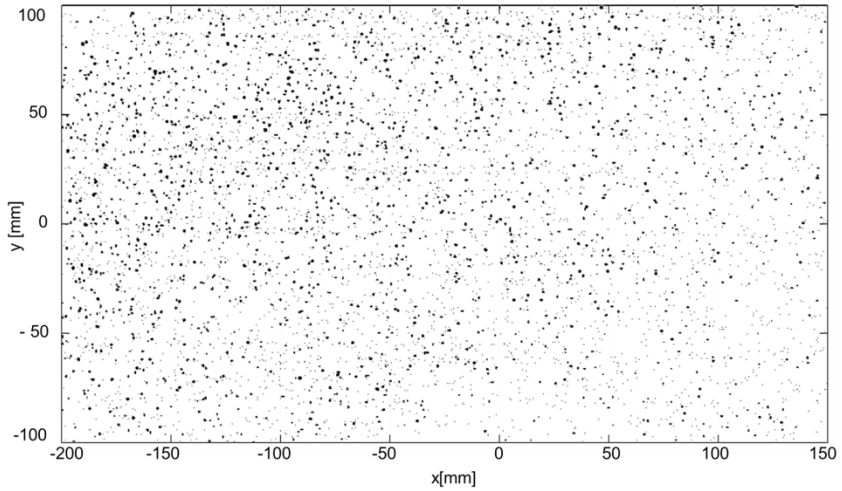


Figure 8.8 - Raw image from camera 2 (inverted gray levels).

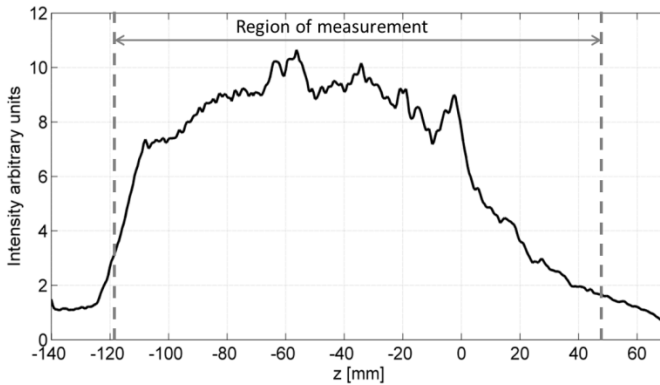


Figure 8.9 - Spanwise profile of reconstructed light intensity.

8.3.2 Results

The temporal evolution of the tip vortices emanating from the blade tip is illustrated by a sequence of four instantaneous velocity and vorticity fields (Figure 8.10) at angular positions of the blade: $\theta = \{0, 30, 60, 90\}$ degrees, corresponding to time steps of 6 ms. The vorticity was computed with an approximation of a grid point with a second order central scheme. A more detailed representation is given with the animation Movie 1 (<https://link.springer.com/article/10.1007/s00348-016-2277-7#SupplementaryMaterial>). In Figure 8.10, the column on the left shows the top view of the measured velocity and vorticity field, while the right column gives the lateral view.

The large-scale tomographic PIV returns the presence of tip vortices regularly generated by the motion of the retrograding blade from the windward to the upwind position. A portion of the blade is captured inside the measurement volume only for $\theta = 0^\circ$ in Figure 8.10a. When the blade is at $\theta = 0^\circ$, it passes through the condition of zero incidence, where no lift is generated. At this particular location, the blade is not releasing any tip vortex, therefore the vortical structures present in the measurement domain, indicated as A and B in Figure 8.10a, have been released by prior blade passages and convected downstream.

When the blade is in position $\theta = 30^\circ$, it releases a tip vortex of finite and measurable strength, labelled with C in Figure 8.10b. The vortices A, B and C are convected downstream by the flow field and their mutual distance depends on the tip speed ratio. From the side views of Figure 9, it is clear that the vortical structures are also convected outboard (towards negative values of Z), departing downward from the blade tip plane ($Z = 0$). The tip vortex C released by the blade at $\theta = 30^\circ$ (Figure 9b) appears weaker than the vortex generated with the blade at higher angle of attack (Figure 8.10c and d). The change of the vortex strength is related to the variation of the lift generated as the blades rotate. The observed behaviour agrees with the three-dimensional unsteady RANS

simulation of Howell *et al.* (2010), where strong correlation between the maximum developed lift and maximum strength of the tip vortex was documented.

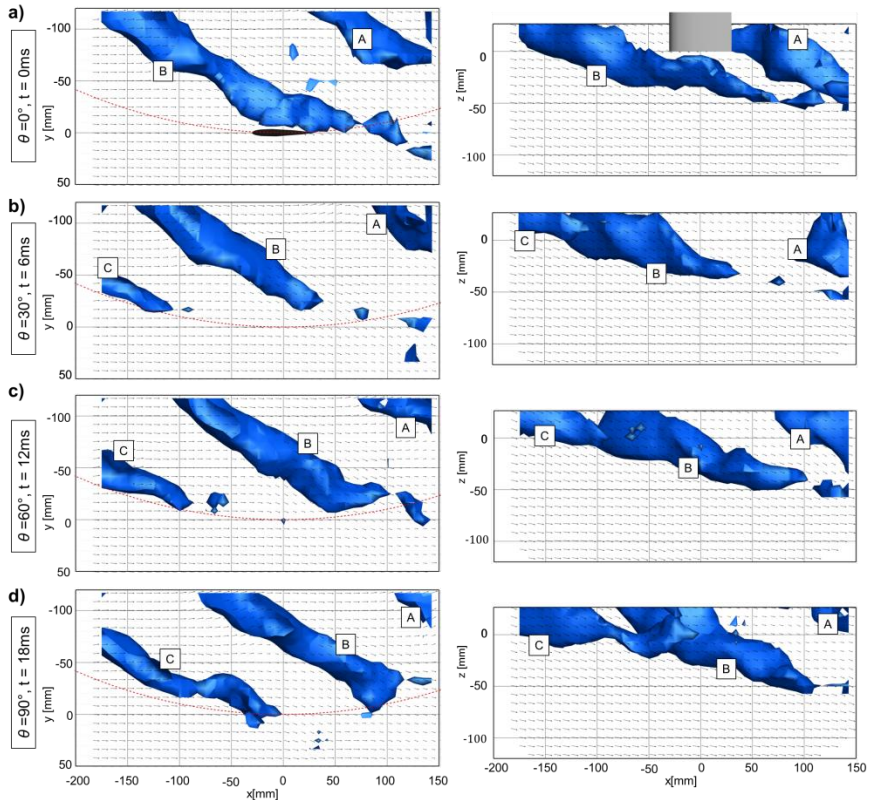


Figure 8.10 - Instantaneous velocity vector field (from cross-correlation) and vorticity magnitude iso-surface ($|\omega| = 170\text{ s}^{-1}$) for tip vortices generated by the retrograding blade in a VAWT. One plane of velocity vectors represented at $Z = 0$ (left) and at $Y = -50\text{mm}$ (right). Red dashed line represents the blade trajectory.

The spanwise velocity profile along the vertical direction of the tip vortex B (Figure 8.10b) is shown in Figure 8.11. The position of the core is determined using the peak value of vorticity. The profile is extracted at plane $X = 50$ mm for ten successive blade passages at $\theta = 30^\circ$. The tip of the blade is located at $Z = 0$, the negative values correspond to the outboard region.

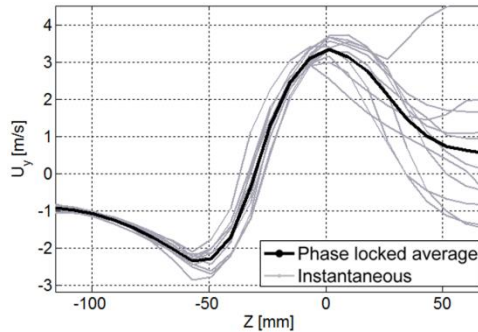


Figure 8.11 - Vertical profile of spanwise velocity component of the tip vortex B across the location of the vorticity ($X = 50$ mm, $\theta = 30^\circ$).

The instantaneous profiles show pronounced velocity fluctuations inside the rotor region ($Z > 0$), whereas the outboard region exhibits a more stable behaviour. The variations of the velocity profiles are therefore localized in the turbulent wake of the blades, in which the laminar-turbulent transition of the boundary layer is forced with the tripping procedure. In addition, the wakes generated by the blades in the upwind position ($0^\circ < \theta < 180^\circ$) are transported downstream through the inner region of the rotor. As a result, the velocity field is characterized by higher fluctuations at this location, as reported by the experimental results of Tescione *et al.* (2014). The interaction between the blades and their own wakes, produced in the previous rotation, influences the flow condition in the pressure and suction sides with a consequent effect on the generation and development of the tip vortices.

Figure 8.12 shows a comparison of the two techniques on an instantaneous vorticity contour of vortex B extracted at $X = 0$ mm. The VIC+ result exhibits a peak vorticity approximately two times higher than that returned with cross-correlation. These discrepancies are ascribed to the higher spatial resolution of the PTV-based algorithm. Similarly to the analysis made on aircraft wing tip vortices (Scarano *et al.*, 2002), limited spatial resolution causes a peak modulation and vortex diameter overestimation; their combined effect is less detrimental in terms of vortex total circulation, which relates to the integral of vorticity. In Figure 8.12, a clear difference of the vortex diameter is not evident. Therefore the circulation associated to the vortex is expected to be underestimated when measured with tomographic cross-correlation compared to VIC+.

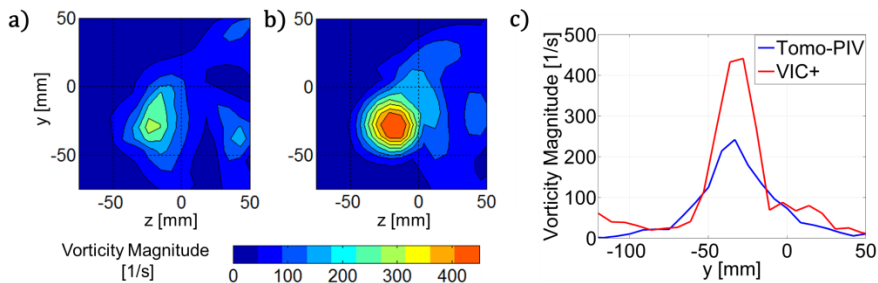


Figure 8.12 - Comparison between cross-correlation and VIC+ for the instantaneous vorticity magnitude of the tip vortex B (Figure 9a). Vorticity magnitude colour contours with cross-correlation (a) and VIC+ (b). Vertical profiles of the vorticity (c).

The peak values of vorticity presented in the work of Tescione *et al.* (2014) are also approximately 300 1/s, but the value only pertains to the y-component as obtained from planar and stereoscopic PIV measurements. The three-dimensional structure of the vortices shed from VAWT would require rotating the measurement angle with the blade position to compensate from the rotation of the vorticity vector. For

practical reasons, experiments are often conducted at a fixed orientation of the measurement plane that only provides one component of the vorticity vector (not generally aligned with the axis of the vortex). Large-scale tomographic PIV allows the measurement of the three components of the vorticity vector, enabling the three-dimensional inspection of the vortex structure, which is strongly affected by the characteristic flow curvature in the rotor region of VAWT. However, as shown in the current experiments, the limited spatial resolution of this approach poses a caveat on the interpretation of peak vorticity and circulation (Figure 8.12c).

Figure 8.13 shows the axial distribution of peak vorticity in vortex B, as indicated in Figure 9a. The peak vorticity is presented along the stream-wise direction X , approximately corresponding to the direction of the vortex axis. The distribution corresponds to the angular position $\theta = 0^\circ$ of the blade. The instantaneous measurements (thin lines) are presented along with the corresponding phase average (thick line).

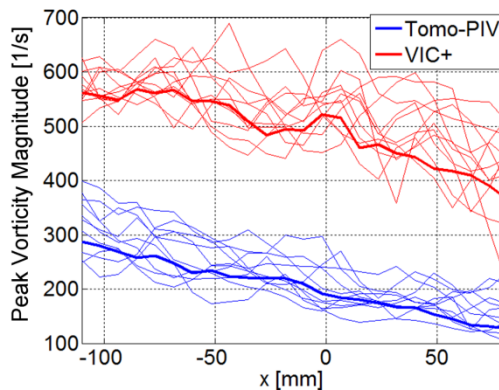


Figure 8.13 - Peak vorticity magnitude of the tip vortex B (Figure 9) with the blade at position $\theta = 0^\circ$. Thin lines correspond to instantaneous measurements and thick lines to the phase average.

The peak vorticity decreases monotonically moving downstream, which is consistent with the increase of lift generated by the blade when it rotates from $\theta = 0^\circ$ to higher values of the phase angle. The results obtained by cross-correlation analysis are significantly below the estimates returned with VIC+, which has also been reported in a study by Schneiders *et al.* (2016). This is mainly due to the more pronounced effect of spatial filtering associated to the cross-correlation operator. Despite the aforementioned effect, the cross-correlation analysis returns a consistent characterization of the tip-vortex topology, the induced velocity field and the dynamical evolution of the vortex.

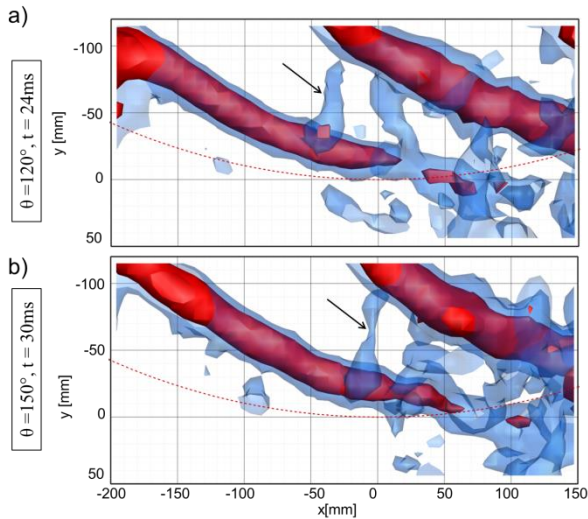


Figure 8.14 - Instantaneous iso-surfaces of vorticity magnitude (red: 300 s^{-1} , blue: 170 s^{-1}) returned by VIC+ data processing.

The instantaneous data exhibit a significant dispersion around the phase-average value (Figure 8.14). The latter cannot be explained by the effect of measurement noise as the flow exhibit turbulent behaviour mainly ascribed to the wake of the blade in the inner rotor region of the VAWT.

In the vorticity field retrieved with VIC+, additional rib-like vortical structures are observed that connect two consecutive tip vortices while convecting downstream (black arrows pointing at them in Figure 8.14). These interactions do not exhibit as regular occurrence as encountered in shear layers dominated by Kelvin-Helmholtz vortices (Lopez and Bulbeck, 1993), however, their structure resembles that of rib-like vortices interconnecting co-rotating tip vortices. The intensity of such ribs has lower values of vorticity compared with those of the tip vortices ($|\omega| < 200$ 1/s) and they are expected to contribute in destabilizing the tip vortices during their dynamical evolution in the rotor wake region.

8.4 Flow around a frigate

The objective of the experimental campaign is to study the behaviour of the wake flow in the landing deck of a frigate at different yaw angles in respect with the main flow. This project is part of an international research, TTCP, AER-TP2, with the propose of understanding and simulating the ship air-wake and its dynamic interaction with the rotor of an helicopter during the landing manoeuvre. The large-scale measurement performed with HFSB will give the possibility to measure and visualize the entire 3D shear layer developing around the landing deck.

8.4.1 *Experimental setup*

The general dimensions of the model are shown in Figure 8.15 where the relative sizes are indicated with respect to the hangar step high h . The model is a simplified version on a frigate in which only the superstructure, the funnel and the landing deck are reproduced (Figure 8.15). The experimental campaign is conducted in the Low Speed Wind Tunnel Facility (LST) of the German-Dutch Wind Tunnels (DNW).

All measurements are performed at $U_\infty = 10$ m/s which results in $Re_h = 8 \times 10^4$ based on the model step height ($h = 10$ cm). The acquisition system, which comprises 4 high-speed Photron Fast CAM SA1 cameras is installed on the side of the test section as described in Figure 8.16. The acquisition frequency is set at 1 kHz. The first three cameras (C1, C2, C3) are equipped with a $f = 60$ mm Nikon objective.

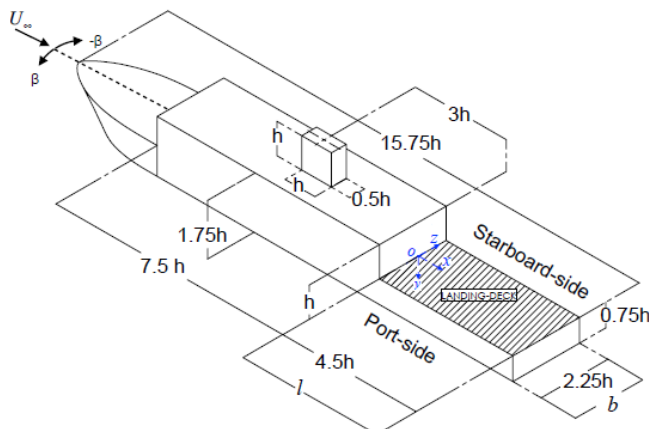


Figure 8.15 - Model dimensions with respect to the hangar step size $h = 10$ cm.

The fourth camera C4 is located slightly farther than the first three cameras due to constraints in the experimental facility, therefore a $f = 105$ mm Nikon objective is used. The aperture is set to $f_\# = 16$ on all cameras, based on the magnification factor $M = 0.032$ of C1 calculated at the mid-plane of symmetry a depth of focus of $\delta z = 691$ mm is achieved.

The illumination source consisted of a high-speed Litron LDY300 Nd:YLF laser (2×30 mJ at 1 kHz) installed outside the test-section. The experimental setup is completed with a multi-generator rake with 20 LaVision nozzles, as the one mentioned in section 4.4. As illustrated in Figure 8.16 the rake is positioned 2.8 m upstream of the model seeding a stream tube of approximately 30×28 cm². The HFSB concentration

reached in the experiment is approximately 0.03 b/cm^3 , which is not enough for an instantaneously analysis of the flow. For this reason the it is used the adaptive Gaussian windowing (AGW; Agüí and Jiménez, 1987), an ensemble averaging technique that in this case is used to interpolate scatter PTV data of all the HFSB tracks detected in the whole time of the acquisition in order to retrieve a time-average flow field within an homogeneous grid of data points of 5 mm of distance between each other. After the time averaging it was reached approximately 150 tracks per cubic centimetre.

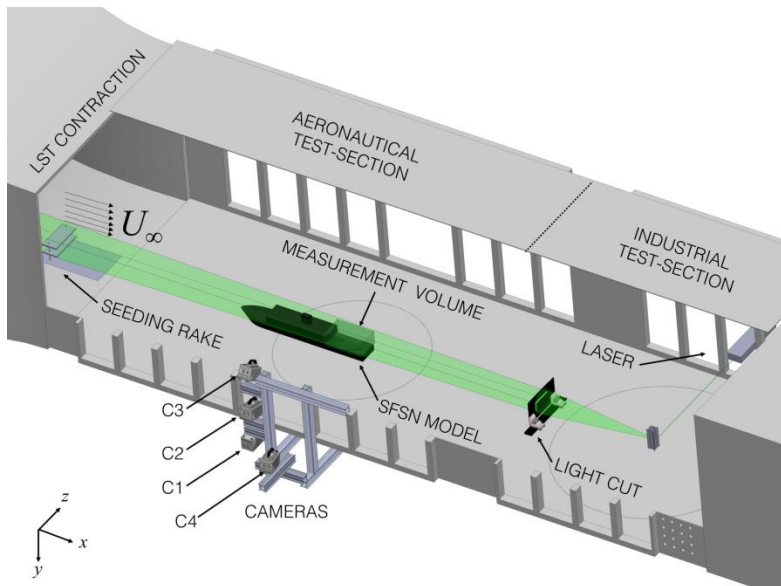


Figure 8.16 - Isometric view of the Tomographic PTV experimental setup in the LST test section at DNW (Rius Vidales, 2016).

8.4.2 Results

When the frigate departs from headwind condition an asymmetric streamwise velocity distribution develops even for very low yaw angles (1°). For a positive yaw angle the flow recirculation region on the port-

side side increases and for negative it decreases as illustrated in Figure 8.17. An iso-surface of Q-criterion clearly identifies the arch vortex (E) in Figure 8.18b. Although similar stream-wise vorticity regions are present at the landing deck region. An increase in stream-wise vorticity in regions (D1-D2) and (G1-G2) is observed as result of a model yaw rotation of one degree which alters also the angle of the funnel with respect to the free-stream flow.

Finally, the opposite behaviour is observed for positive yaw angles, see Figure 8.18a. The present results show that the change in the time average structure of the flow leads to the observed stream-wise asymmetrical velocity distribution. Additionally the sensitivity of the wake orientation with yaw angle variation is confirmed.

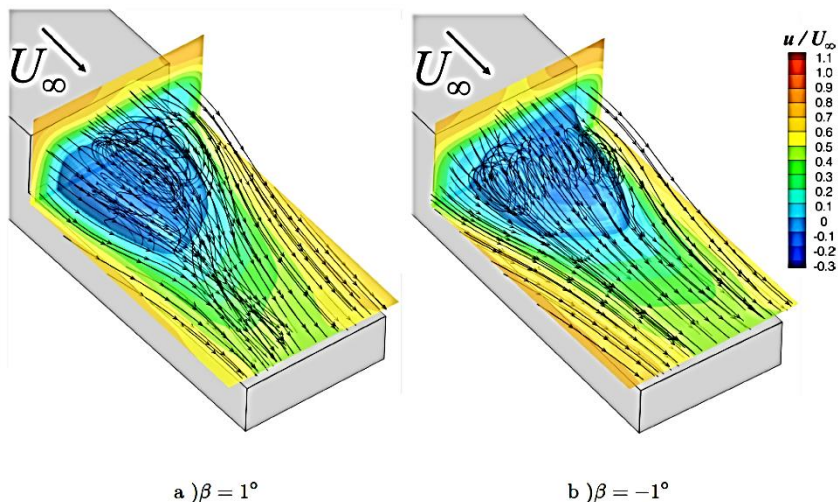


Figure 8.17 - Time-Averaged Velocity Field in the Landing Deck region at $Re_h = 8 \cdot 10^4$. Contours of stream-wise Velocity component ($x/l = 0.06$, $y/h = -0.1$). One iso-surface at $|U| = 0$ m/s (Rius Vidales, 2016).

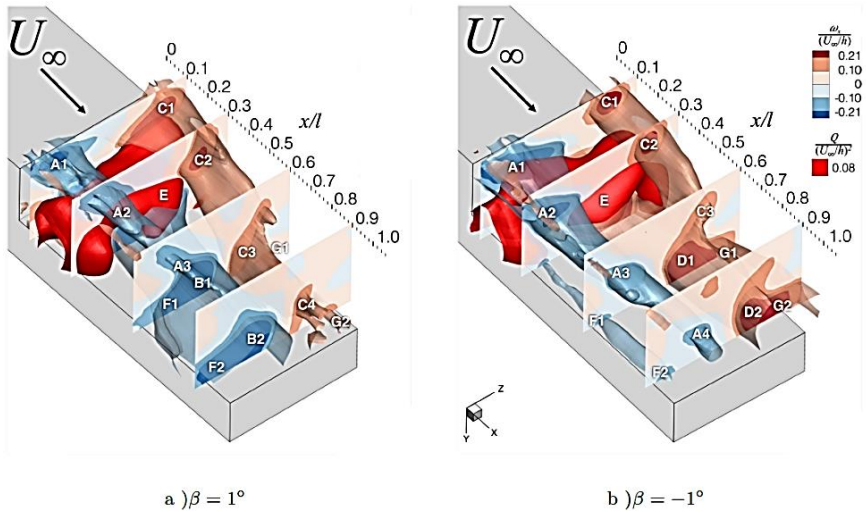


Figure 8.18 - Time averaged flow structures in the landing-deck region for near head-wind conditions ($\beta = 1^\circ$ and $\beta = -1^\circ$), $Re_h = 8 \cdot 10^4$; One Q-criterion iso-surface in conjunction with two stream-wise vorticity (w_x) iso-surfaces and several vertical planes colour coded with stream-wise vorticity (w_x) (Rius Vidales, 2016).

8.5 Lessons learned from experiments

The experiments described in the previous sections provide the capabilities of the PIV measurements with HFSB in different turbulent flows. Figure 8.19 shows a survey of relevant experiments in airflows where the measurement volume is plotted against the acquisition frequency. The measurements described in this chapter and other experimental campaigns conducted with HFSB by Kühn *et al.* (2011), Schneiders *et al.* (2016), and Huhn *et al.* (2016) have measurement volumes that are 2-3 orders of magnitude higher in respect with previous tomographic PIV experiments performed in the past. One can see that

volumetric measurements with acquisition frequency at the order of kilohertz do not reach 100 cm^3 when micro-size tracers are used. This shows that the extension to measurements volumes in the order of the litre can be applied for high-speed volumetric PIV system only with HFSB.

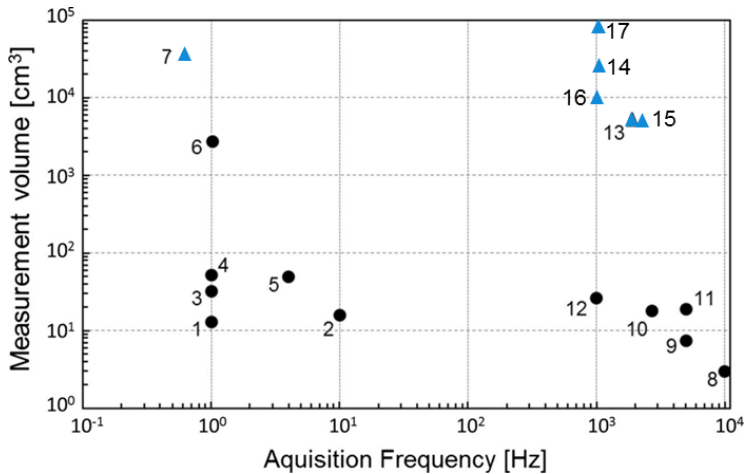


Figure 8.19 - Measurement volume versus acquisition frequency for relevant Tomographic PIV experiments in airflows with conventional seeding (dots) and HFSB (triangles). 1 *Elsinga et al.* (2006), 2 *Humble et al.* (2009), 3 *Atkinson et al.* (2011), 4 *Schröder et al.* (2011), 5 *Staack et al.* (2010), 6 *Fukuchi* (2012), 7 *Kühn et al.* (2011), 8 *Pröbsting et al.* (2013), 9 *Violato et al.* (2011), 10 *Ghaemi and Scarano* (2011), 11 *Schröder et al.* (2009), 12 *Michaelis et al.* (2012), 13 *Circular cylinder wake flow*, 14 *VAWT experiment*, 15 *Schneiders et al.* (2016), 16 *Frigate experiment*, 17 *Huhn et al.* (2016).

The reasons are described in chapter 2 and 3, where it is explained how the volumetric illumination intensity reduces in respect with planar PIV and it reduces even further at high acquisition frequency, considering the inverse proportionality between the light source repetition rate and pulse energy. The problem is exacerbated by the small optical aperture (high $f_{\#}$)

of the imaging system, needed to obtain focused particles in all the measurement dept.

The comparison between the three experiments summarized in Table 8.1 and described in this chapter shows that the *DSR* is on the order of standard tomographic experiments (Table 4.3), as it was discussed in chapter 4. The *DSR* retrieved in the experiment with the frigate reaches a value almost on order of magnitude higher in comparison with the other experiments. The reason is related to the technique used to retrieve the velocity vector field, which is obtained through a time-averaging procedure. Indeed, the instantaneous bubble concentration in the latter case is much lower than the first two experiments. The reason depends of the different type of seeding system used to inseminate the flow. In the case of the piston-cylinder system (chapter 4) a measured concentration of approximately 1 b/cm^3 is obtained. The effect of the free stream velocity of the concentration is mitigated by the volume of air injected from the reservoir, \dot{V}_0 , as it is shown in Eq. 4.10.

Table 8.1 - HFSB concentration and Dynamic special (spatial) range for the experiments described in this chapter.

	U_∞ [m/s]	Measurement domain [cm ³]	Seeding System	C [b/cm ³]	<i>DSR</i>
Wake of cylinder	4	9.6×10^3	Piston-cylinder System	1	10
VAWT	8.5	12×10^3	Piston-cylinder System	1	13
Frigate	10	10^4	20 nozzle in parallel	0.01	80*

* *DSR* is computed after doing the time-average

9

CONCLUSIONS

9.1 Seeding system for large scale measurements

The increasing need of aerodynamic research and development in the aerospace, ground vehicle and wind energy sectors requires the development of more efficient measuring techniques in terms of versatility. The possibility of conducting instantaneous measurements at full model scales and/or capturing the entire wake dynamics will favour the aerodynamic industry needs. The second chapter has shown the main limitations of the PIV equipment (i.e. light sources and imaging system) regarding the enlargement of the measurement domains. In chapter 3, the state of art of seeding particle for PIV experiments in low speed wind tunnels has been discussed. The comparison of different tracers (i.e. diameter, density, and refractive index) reveals that only HFSB are the candidates to perform large scale measurements with the current technology of light source and cameras. This was further demonstrated in previous experiments conducted in closed volumes with convective flows. However, the use of HFSB in wind tunnels for PIV measurements was hampered by the limited production rate of the bubble generators and the lack of information about the HFSB in terms of tracing fidelity.

The present dissertation proposes different solution in order to increase the number of HFSB injected in flow, namely the piston-cylinder system and the multi-nozzle rake described in chapter 4. The first solution increases the rate of bubbles injected in the stream using one or a limited number of generator. The principle of accumulating the HFSB in a reservoir and conveying them to an injector placed in the wind tunnel through a pipeline has been demonstrated to be effective for tomo-PIV measurements. The bubbles extinction during their transport from the reservoir to the exit of the injector and their collisions inside the reservoir were also documented. This reason, accompanied by a greater availability of generators promoted the development of the second solution, namely the installation of multiple bubble generators directly in the wind tunnel within an aerodynamic rake. Moreover, a framework for the evaluation of the seeding concentration and measurement dynamic spatial range based on the seeding production rate, free-stream velocity and geometry of seeding system and wind tunnel has been developed in chapter 4.

9.2 Dynamic behaviour of HFSB

In chapter 5, for the first time the relaxation time of sub-millimetre HFSB was estimated. For this purpose, an experimental procedure was introduced where the dynamic behaviour of the HFSB is compared to that of conventional micro-size droplets in the potential flow ahead a cylinder. The estimated characteristic response time scale ranges between 10 and 50 μs . The HFSB can be considered an accurate tracing particle for most aerodynamic applications, considering that many flows in low speed wind tunnels have characteristic time of the order of milliseconds,. Despite the relative large size of the HFSB, which exceeds by two orders of magnitude that of the micro-size droplets normally adopted in wind

tunnels, the low relaxation time is achieved via the neutrally buoyant condition of the bubbles in air-flows (ratio between bubble and air density approximately equal to 1). The ability to tune the HFSB density enables to conduct measurements that are precluded even for the 1- μm -droplets, as in the case of flows where body forces are dominant. One of the most relevant examples in aerodynamics is that of vortical flows. As discussed in chapter 6, the use of neutrally buoyant or slightly buoyant HFSB is proposed as a possible approach to solve the problem of lack of tracer particles in the vortex core, which precludes detailed velocity measurements by particle image velocimetry. The particles density relative to that of the air is the key parameter that determines whether the tracer particles are centrifuged outside of the vortex or accumulated at its centre. Experiments conducted on the leading edge vortex of a slender delta wing assess the capability of HFSB to populate the vortex core. Neutrally buoyant HFSB appear rather homogeneously distributed within the leading edge vortex region. In contrast, fog droplets are visibly centrifuged outside the vortex core and produce a “black hole”. As a result, the correlation signal-to-noise ratio obtained using fog droplets as tracers for stereo-PIV suffers from drop-out in the vortex core. The problem is circumvented with neutrally buoyant HFSB that yield a reliable velocity measurement in the vortex core as well as in the outer region.

9.3 Optical behaviour of HFSB

Chapter 7 has discussed the light scattering behaviour of the HFSB, with focus on the quantification of scattered energy and the scaling behaviour with the diameter of the bubbles and with the scattering angle. The main conclusion of the optical assessment is that the HFSB scatter 10^4 - 10^5 more light with respect to the micro-size droplets. The amount of

light scattered increases with a quadratic dependence with the bubble's diameter and exhibits minor variations with the scattering direction. The empirical formulation expressed in section 7.3 allows the estimation of the size of the illuminated volume achievable in order to still detect the HFSB by a conventional imaging system, knowing the power of the light source and the size of the HFSB.

9.4 Perspectives

In the last years different milestones were accomplished for the development of large-scale 3-D PIV for industrial aerodynamic applications. The characterization of HFSB in terms of tracing fidelity, optical properties and the design of an injection system to reach adequate seeding concentration within a stream-tube of optimum size are just the first steps. The increasing use of HFSB recorded by different institutes requires a large-scale production of HFSB generator and therefore a deeper understanding of the bubble formation. This information will allow a more efficient production rate in terms of bubble size dispersion, life time of the bubbles, and the possibility to produce neutrally buoyant HFSB within a large range of size, in order to increase the versatility of seeding system.

Aside from tracing particles a more versatile 3-D PIV system needs other developments. One is the need to simplify the arrangement of the imaging system (3-4 cameras) and formation of the light beam in order to reduce the mounting time of the PIV setup and geometrical calibration. The current complication of the tomo-PIV set-up is still a fundamental limitation within the industrial wind tunnels experiments. A solution to overcome those constraints is to mount the cameras within a single probe, in which the relative angles between the imagers are kept fix. The

illumination can be provided from the same probe in which is installed an optical fibre connected with the light source, as it is shown in Figure 9.1. The coaxial imaging and illumination probe (Schneiders *et al.*, 2017) can be repositioned to measure different regions of interest of the flow without repeating the geometrical calibration (Jux *et al.*, 2017). As a result, this coaxial configuration increases the flexibility of the volumetric measurement in large-scale domains.

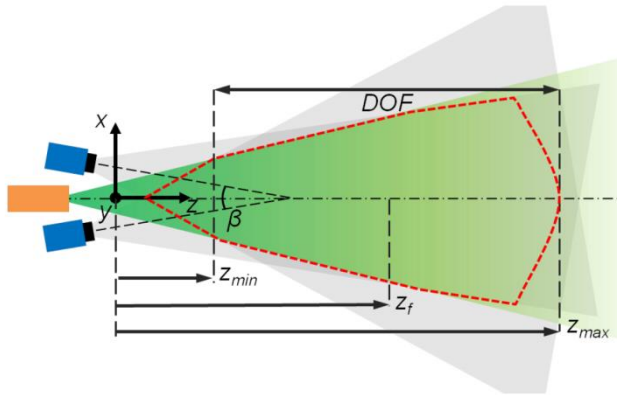


Figure 9.1 - Schematic of the coaxial imaging and illumination configuration, with light source (orange), tomographic cameras (blue) and low aperture lenses (black). Fields of view indicated in grey, whereas illumination volume is green. Measurement volume is outlined in dashed red (Jux C., 2017).

The use of HFSB is also extended in field experiments outside wind tunnels. An example is related to the on-site sport aerodynamics, where the use of large-scale measurements, on the order of a human being, can provides insights on the posture of the athletes and equipment geometry (i.e. helmets) to reduce the aerodynamic drag.

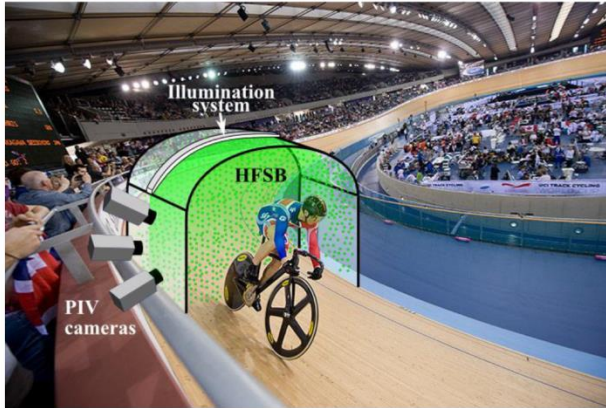


Figure 9.2 - Schematic representation of the ring-of-fire concept for on-site aerodynamic measurements in a velodrome (Sciacchitano *et al.*, 2015).

The concept of the on-site experimental setup, named ‘*ring-of-fire*’ was first introduced by Sciacchitano *et al.* (2015) and includes a measuring system installed in a chamber that can be integrated in different fields, such velodromes (as in Figure 9.2), racing tracks and other sport fields.

REFERENCES

- Adrian R J and Yao C S (1985), Pulsed laser technique application to liquid and gaseous flows and the scattering power of seed materials, *Appl. Opt.* 24:44-52
- Adrian RJ (1991), Particle-imaging techniques for experimental fluid mechanics, *Annu. Rev. Fluid. Mech.* 23: 261-304
- Adrian RJ (1997), Dynamic ranges of velocity and spacial resolution of particle image velocimetry, *Meas. Sci. Technol.* 8:1393
- Adrian RJ (2005), Twenty years of particle image velocimetry, *Exp. Fluids* 39: 159-169
- Adrian RJ and Westerweel J (2011), *Particle image velocimetry*, Cambridge University Press
- Adrian RJ, Meinhart CD and Tomkins CD (2000), Vortex organization in the outer region of the turbulent boundary layer, *J. Fluid Mech.* 422: 1-54
- Arroyo MP and Greated CA (1991), Stereoscopic particle image velocimetry, *Meas. Sci. Technol.* 2: 1181
- Atkinson C, Coudert S, Foucaut JM, Stanislas M and Soria J (2011), The accuracy of tomographic particle image velocimetry for measurements of a turbulent boundary layer, *Exp. Fluids* 50: 1031-1056
- Bailey SC, Tavoularis S, and Lee BH (2006), Effects of Free-Stream Turbulence on Wing-Tip Vortex Formation and Near Field, *J. air.* 43: 1282-1291
- Beaudoin JF and Aider JL (2008), Drag and lift reduction of a 3D bluff body using flaps, *Exp. Fluids* 44: 491-501
- Bhagwat M and Ramasamy M (2012), Effect of tip vortex aperiodicity on measurement uncertainty, *Exp. Fluid* 53: 1191-1202
- Bosbach J, Kühn M and Wagner C (2009), Large scale particle image velocimetry with helium filled soap bubbles, *Exp. Fluids* 46: 539-547
- Caridi GCA, Ragni D, Sciacchitano A and Scarano F (2016), HFSB-seeding for large-scale Tomographic PIV in wind tunnels, *Exp. Fluids* 53: 1191-1202

- Caridi GCA, Sciacchitano A & Scarano F (2017), Helium-filled soap bubbles for vortex velocimetry, *Exp. Fluids* 58: 130
- Carmer CF, Konrath R, Schroder A and Monnier JC (2008), Identification of vortex pairs in aircraft wakes from sectional velocity data, *Exp. Fluids* 44: 367-380
- Chan YM and Dalgarno A (1965), The refractive index of helium, *Proc. of the Phys. Soc.* 85: 227
- Clancy LJ (1975), *Aerodynamics*, Halsted Press
- Conlisk AT (1997). *Modern helicopter aerodynamics*. *Annu. Rev. Fluid Mech.* 29: 515-567
- Devenport WJ, Rife MC, Liapis SI and Follin GJ (1996), The structure and development of a wing-tip vortex, *J. Fluid Mech.* 312: 67-106
- Discetti S and Astarita T (2012), Fast 3D PIV with direct sparse cross-correlations, *Exp. Fluids* 53: 1437-1451
- Durst F and Stevenson WH (1979), Influence of Gaussian beam properties on laser Doppler signals, *App. Opt.* 18: 516-524
- Elsinga GE, Scarano F, Wieneke B and Van Oudheusden BW (2006), Tomographic particle image velocimetry, *Exp. Fluids* 41: 933-947
- Elsinga GE, Westerweel J, Scarano F and Novara M (2011), On the velocity of ghost particles and the bias errors in Tomographic-PIV, *Exp. in Fluids* 50: 825-838
- Escudier M (1988), Vortex breakdown: observations and explanations, *Prog. Aero. Sci.* 25: 189-229
- Ferrell, GB, Aoki K and Lilley DG (1985), Flow visualization of lateral jet injection into swirling crossflow, *AIAA Paper* 85.0059: 14-17
- Fukuchi Y, (2012), Influence of number of cameras and preprocessing for thick volume Tomographic PIV, 16th Int. Symp. Applications of Laser Techniques to Fluid Mechanics, Lisbon, Portugal
- Furman A and Breitsamter C (2013), Turbulent and unsteady flow characteristics of delta wing vortex systems, *Aero. Sci. Technol.* 24: 32-44
- Ghaemi S and Scarano F (2010), Multi-pass light amplification for tomographic particle image velocimetry application, *Meas. Sci. Technol.* 21: 127002

- Ghaemi S and Scarano F (2011), Counter-hairpin vortices in the turbulent wake of a sharp trailing edge, *J. Fluid Mech.* 689: 317-356
- Goto S (2008), A physical mechanism of the energy cascade in homogeneous isotropic turbulence, *J. Fluid Mec.* 605: 355-366
- Hain R and Kähler CJ (2007). Fundamentals of multiframe particle image velocimetry (PIV), *Exp. in Fluids* 42: 575-587
- Hale RW, Tan P and Ordway DE (1971a), Experimental investigation of several neutrally-buoyant bubble generators for aerodynamic flow visualization, *Nav. Res. Rev.* 24: 19-24
- Hale RW, Tan P, Stowell RC and Ordway DE (1971b), Development of an integrated system for flow visualization in air using neutrally-buoyant bubbles, SAI-RR 7107, SAGE ACTION Inc, Ithaca, NY, USA
- Herman GT and Lent A (1976), Iterative reconstruction algorithms, *Comput. Bio. Med.* 6: 273-294
- Hong J, Toloui M, Chamorro LP, Guala M, Howard K, Riley S, Tucker J and Sotiropoulos F (2014), Natural snowfall reveals large-scale flow structures in the wake of a 2.5-MW wind turbine, *Nat. Commun.* 5
- Hulst HC (1957), *Light scattering by small particles*, Dover Publication New York
- Humble RA, Elsinga GE, Scarano F and Van Oudheusden BW (2009), Three-dimensional instantaneous structure of a shock wave/turbulent boundary layer interaction, *J. Fluid Mech.* 622: 33-62
- Iwan LS, Hale RW, Tan P and Stowell RC (1973), *Transonic flow visualization with neutrally-buoyant bubbles*, SAI-RR 7304, Ithaca, NY, USA
- Julien PY (1986), Concentration of very fine silts in a steady vortex, *J. Hydraul. Res.* 24: 255-264
- Kähler CJ, Scharnowski S and Cierpka C (2012), On the resolution limit of digital particle image velocimetry, *Exp. Fluids* 52: 1629-1639
- Keane RD and Adrian RJ (1990), Optimization of particle image velocimeters. Part I: Double pulsed systems, *Meas. Sci. Technol.* 1: 1202-1215
- Keane RD and Adrian RJ (1992). Theory of cross-correlation analysis of PIV images. *App. Sci. Res.* 49: 191-215

- Kerho MF and Bragg MB (1994), Neutrally buoyant bubbles used as flow tracers in air, *Exp. Fluids* 16, 393-400
- Kim I and Pearlstein AJ (1990), Stability of the flow past a sphere, *J. Fluid Mech.* 211: 73-93
- Klimas P (1973), Helium bubble survey of an opening parachute flowfield, *J. Aircraft* 10, 567-5694
- Kompenhans J, Raffel M, Dieterle L, Dewhirst T, Vollmers H, Ehrenfried K, Willert C, Pengel K, Kähler C, Schröder A and Ronneberger O (2000), Particle image velocimetry in aerodynamics: Technology and applications in wind tunnels, *J. Visual.* 2: 229-244
- Konrath R, Klein C and Schröder A (2013), PSP and PIV investigations on the VFE-2 configuration in sub-and transonic flow, *Aero. Sci Technol.* 24: 22-31
- Kühn M, Ehrenfried K, Bosbach J and Wagner C (2011), Large-scale tomographic particle image velocimetry using helium-filled soap bubbles, *Exp. Fluids* 50: 929-948
- Lecuona A, Ruiz-Rivas U and Nogueira J (2002), Simulation of particle trajectories in a vortex-induced flow: application to seed-dependent flow measurement techniques, *Meas. Sci. and Technol.* 13:1020
- Leishman JG (1996). Seed particle dynamics in tip vortex flows. *J. Aircraft* 33:823-825
- Lignarolo LEM, Ragni D, Krishnaswami C, Chen Q, Simão Ferreira CJ and Van Bussel GJW (2014), Experimental analysis of the wake of a horizontal-axis wind-turbine model, *Renew. Energ.* 70: 31-46
- Lignarolo LEM, Ragni D, Scarano F, Ferreira CS and van Bussel GJW. (2015), Tip-vortex instability and turbulent mixing in wind-turbine wakes, *J. Fluid Mech.* 781: 467-493
- Liu Z, Zheng Y, Jia L, Jiao J and Zhang Q (2006), Stereoscopic PIV studies on the swirling flow structure in a gas cyclone, *Chem. Eng. Sci.* 61: 4252-4261
- Lobutova E, Resagk C, Rank R and Müller D (2009), Extended three dimensional particle tracking velocimetry for large enclosures. *Imag. Meas. Meth. Flow Analys*, Springer Berlin Heidelberg

- Lynch KP and Scarano F (2014), Experimental determination of tomographic PIV accuracy by a 12-camera system, *Meas. Sci. Technol.* 25: 084003
- Maas HG, Gruen A and Papantoniou D (1993), Particle tracking velocimetry in three-dimensional flows, *Exp. Fluids* 15: 133-146
- Macháček M (2002), A quantitative visualization tool for large wind tunnel experiments (Doctoral dissertation), ETH Zurich
- Macháček M and Rösgen T (2003), Fluid flow visualization by three-dimensionally reconstructed tracer path lines. *J Vis*, 6:115-124
- Mei R (1996). Velocity fidelity of flow tracer particles. *Experiments in Fluids* 22: 1-13
- Meinhart CD, Wereley ST and Santiago JG (2000), A PIV algorithm for estimating time-averaged velocity fields. *J Fluids Eng*, 122:285-289
- Melling A (1997), Tracer particles and seeding for particle image velocimetry, *Meas. Sci. Technol.* 8: 1406
- Michaelis D, Bompfrey R, Henningsson P and Hollis D (2012), Reconstructing the vortex skeleton of the desert locust using phase averaged POD approximations from time resolved thin volume tomographic PIV, 16th Int. Symp. on Applications of Laser Techniques to Fluid Mechanics, Lisbon, Portugal
- Mie G (1908), Beiträge zur Optik trüber Medien, speziell kolloidaler Metallösungen. *Annu. Phys.* 330: 377-445
- Müller D, Müller B, and Renz U (2001), Three-dimensional particle-streak tracking (PST) velocity measurements of a heat exchanger inlet flow, *Exp. Fluids* 30: 645-656
- Müller RHG, Flögel H, Scherer T, Schaumann O and Markwart M (2000), Investigation of large scale low speed air conditioning flow using PIV, 9th Int. Symp. on Flow Visualization, Edinburgh, UK
- Müller RHG, Scherer T, Rotger T, Schaumann O and Markwart M (1997). Large body aircraft cabin a/c flow measurement by helium bubble tracking. *J. Flow Vis. Image Proc.* 4.3
- Nelson RC and Pelletier A (2003), The unsteady aerodynamics of slender wings and aircraft undergoing large amplitude maneuvers, *Prog. Aero. Sci.* 39: 185-248

- Pounder E (1956), Parachute inflation process Wind-Tunnel Study, WADC Technical report 56-391, Equipment Laboratory, Wright-Patterson Air Force Base, pp 17-18, Ohio, USA
- Prasad AK (2000), Stereoscopic particle image velocimetry, *Exp. in Fluids* 29: 103-116
- Prasad AK and Jensen K (1995), Scheimpflug stereocamera for particle image velocimetry in liquid flows, *App. Opt.* 34: 7092-7099
- Pröbsting S, Scarano F, Bernardini M and Pirozzoli S (2013), On the estimation of wall pressure coherence using time-resolved tomographic PIV, *Exp. Fluids* 54:1-15
- Qureshi NM, Bourgoin M, Baudet C, Cartellier A, and Gagne Y (2007), Turbulent transport of material particles: an experimental study of finite size effects, *Physical Review Letters* 99
- Raffel M, Richard H, Ehrenfried K, Van der Wall B, Burley C, Beaumier P, McAlinster K & Pengel K (2004), Recording and evaluation methods of PIV investigations on a helicopter rotor model, *Exp. Fluids* 36: 146-156
- Raffel M, Willert CE and Kompenhans J (2008). Particle image velocimetry: a practical guide. Springer, Berlin 2nd edition
- Raffel M, Willert CE, Wereley S and Kompenhans J (2013), Particle image velocimetry: a practical guide, Springer, Berlin 3rd edition
- Raffel M, Willert CE, Wereley ST and Kompenhans J (2007), Particle Image Velocimetry -A Practical Guide, 2nd Edition, Springer, Berlin Heidelberg
- Redon H (1938), U.S. Patent No. 2,134,890, Washington, DC: U.S. Patent and Trademark Office
- Rockwell D (1993), Three-dimensional flow structure on delta wings at high angle-of-attack-Experimental concepts and issues, In 31st Aerospace Sciences Meeting, 550
- Ruith MR, Chen P, Meiburg E and Maxworthy T (2003), Three-dimensional vortex breakdown in swirling jets and wakes: direct numerical simulation, *J. Fluid Mech.* 486: 331-378
- Samimy M and Lele SK (1991), Motion of particles with inertia in a compressible free shear layer, *Phys. Fluids* 3:1915-1923
- Scarano F (2001), Iterative image deformation methods in PIV. *Meas. Sci. and Technol.* 13: R1-R19

- Scarano F (2013), Tomographic PIV: principles and practice, *Meas. Sci. and Technol.* 24: 012001
- Scarano F and Poelma C (2009), Three-dimensional vorticity patterns of cylinder wakes, *Exp. Fluids* 47: 69-83
- Scarano F, Ghaemi S, Caridi GCA, Bosbach J, Dierksheide U and Sciacchitano A (2015), On the use of helium-filled soap bubbles for large-scale tomographic PIV in wind tunnel experiments, *Exp. Fluids* 56:1-12
- Schröder A, Geisler R, Elsinga GE, Scarano F and Dierksheide U (2008), Investigation of a turbulent spot and a tripped turbulent boundary layer flow using time-resolved tomographic PIV, *Exp. Fluids* 44: 305-316
- Schröder A, Geisler R, Sieverling A, Wieneke B, Henning A, Scarano F, Elsinga GE and Poelma C (2009), Lagrangian aspects of coherent structures in a turbulent boundary layer flow using TR-Tomo PIV and FTV, 8th Int. Symp. on Particle Image Velocimetry, Melbourne, Victoria, Australia
- Schröder A, Geisler R, Staack K, Elsinga GE, Scarano F, Wieneke B and Westerweel J (2011), Eulerian and Lagrangian views of a turbulent boundary layer flow using time-resolved tomographic PIV, *Exp. Fluids* 50: 1071-1091
- Soft KD (1986), *Fotograie: Grundlagen, Technik, Praxis*, Fisher Taschenbuch Verlag, Frankfurt
- Sohn MH and Chang JW (2012), Visualization and PIV study of wing-tip vortices for three different tip configurations, *Aero Sci. Technol.* 16: 40-46
- Spalart PR (1998), Airplane trailing vortices. *Ann. Rev. Fluid Mech.* 30: 107-138
- Staack K, Geisler R, Schröder A and Michaelis D (2010), 3D-3C-coherent structure measurements in a free turbulent jet, 15th Int. Symp. on Applications of Laser Techniques to Fluid Mechanics, Lisbon, Portugal
- Stanislas M, Okamoto K and Kähler C (2003), Main results of the first international PIV challenge, *Meas. Sci. Technol.* 14.10: R63
- Stanislas M, Okamoto K, Kähler CJ, Westerweel J and Scarano F (2008), Main results of the third international PIV challenge, *Exp. in Fluids*, 45: 27-71

- Sun Y, Zhang Y, Wang A, Topmiller JL and Bennet JS (2005), Experimental Characterization of Airflows in Aircraft Cabins, Part I: Experimental System and Measurement Procedure, ASHRAE transactions 111
- Taneda S (1956), Experimental investigation of the wake behind a sphere at low Reynolds numbers, *J. Phys Soc. Jpn* 11: 1104-1108
- Tescione G, Ragni D, He C, Ferreira CS and van Bussel, GJW (2014), Near wake flow analysis of a vertical axis wind turbine by stereoscopic particle image velocimetry, *Renew En.* 70: 47-61
- Thomas L, Vernet R, Tremblais B and David L (2010), Influence of geometric parameters and image pre-processing on Tomo-PIV results, 15th Int. Symp. Appl. Int. Symp. on Applications of Laser Techniques to Fluid Mechanics, Lisbon, Portugal
- Tropea C (2011), Optical particle characterization in flows, *Ann. Rev. Fluid Mech.* 43: 399-426
- Urban WD and Mungal MG (2001), Planar velocity measurements in compressible mixing layers, *J. Fluid Mech.* 431: 189-222
- Van de Hulst HC and Wang RT (1991), Glare points, *Appl. Optics* 30: 4755-4763
- Vermeer LJ, Sørensen JN and Crespo A (2003), Wind turbine wake aerodynamics. *Prog. Aero. Sci.* 39: 467-510
- Violato D, Moore P and Scarano F (2011), Lagrangian and Eulerian pressure field evaluation of rod-airfoil flow from time-resolved tomographic PIV, *Exp. Fluids* 50: 1057-1070
- Wang C, Gao Q, Wei R, Li T and Wang J (2016), 3D flow visualization and tomographic particle image velocimetry for vortex breakdown over a non-slender delta wing, *Exp. Fluids* 57: 1-13
- Westerweel J (1997), Fundamentals of digital particle image velocimetry, *Meas. Sci. Technol.* 8: 1379
- Westerweel J and Scarano F (2005), Universal outlier detection for PIV data, *Exp. Fluids* 39: 1096-1100
- Westerweel J, Elsinga GE and Adrian RJ (2013), Particle image velocimetry for complex and turbulent flows, *Annu. Rev. Fluid Mech.* 45: 409-436

-
- Wieneke B (2014), Generic a-posteriori uncertainty quantification for PIV vector fields by correlation statistics, 17th Int. Symp on Applications of Laser Techniques to Fluid Mechanics Lisbon, Portugal
- Willert C (1997), Stereoscopic digital particle image velocimetry for application in wind tunnel flows, *Meas. Sci. Technol.* 8:1465
- Willert C, Stasicki B, Klinner J and Moessner S (2010), Pulsed operation of high-power light emitting diodes for imaging flow velocimetry, *Meas. Sci. Technol.* 21: 075402
- Zhao L, Zhang Y, Wang X, Riskowski GL and Christianson LL (1999). Measurement of airflow patterns in ventilated spaces using particle image velocimetry. In An ASAE Meeting Presentation, Paper (No. 994156).

ACKNOWLEDGEMENTS

In the first place I would like to express my gratitude to my supervisor and *promoter* prof. dr. Fulvio Scarano for the opportunity he gave me to carry out this PhD research. I am also grateful to my *co-promotor* dr. Andrea Sciacchitano for his support and guidance during my studies. The collaboration with Fulvio and Andrea gave me valuable experiences throughout these years. Moreover, their enthusiasm, dedication and work strategies have inspired me and have shown me the path for a successful research project.

I extend my thanks to Uwe Dierksheide and LaVision GmbH for sharing their knowledge and equipment related to the HFSB generators during my first year of PhD.

During the entire period of my research, I had the opportunity to exchange and learn from many skilled colleagues and friends. In particular, I gratefully acknowledge dr. Daniele Ragni, who gave me his encouragement and constructive advises for the success of my project. His skills, commitment, and strong altruism made him as a source of inspiration, which enrich my growth as a researcher. Dani, thank you also for sharing with me many activities and passions as PIV, biking, the art of complaining and music!

I have also benefited from the advice and guidance of dr. Marios Kotsonis who always kindly granted me his time and comprehensive knowledge.

Special thanks go to Jacopo Serpieri, my PhD-mate, with whom I shared this journey from the first day till the very last. Jacopo, you always offered me support and hospitality as an old friend. Thank you also for keeping a sense of humour when I had lost mine.

Furthermore, I'm grateful to dr. Jan F.G. Schneiders for collaborating in many challenging and incredible experiences, from the fastest Tomo-PIV measurement ever till the wine taste in Chiaia.

Thanks also to dr. Valeria Gentile, dr. Theo Michelis, dr. Francesco Avallone and dr. Carlos Arce Leon for their help and for the nice time spent together in and out of the lab.

Thanks to the students I co-supervised, in particular Koen Morias, Rakesh Yuvaraj and Alberto Felipe Rius Vidales for their contribution to this thesis. Alberto, not surprisingly, you have become a colleague and I wish you all the success for the following years.

I want to acknowledge all members of the *large-scale* group of the Aerodynamics department for the constructive discussions and for the opportunity to exchange ideas, solutions and techniques.

This project could not have been possible without the assistance of the technicians of the Aerodynamic department: Frits Donker Duyvis, Peter Duyndam, Nico van Beeck and Henk-Jan Siemer. In particular, thanks to Frits and his valuable efforts for the development of the HFSB-hardware in TU Delft. Special thanks go to Peter, who has kindly wished me 'good morning' every day and supported me a lot in the workshop. I am very grateful to Colette Russo for her patience, assistance, and problem-solving skills.

Completing this work would have been much harder without the support and friendship provided by my officemates. You guys have taught me the true value of an international and multicultural experience! Therefore, thanks to Shaafi, Rakesh (and his spicy chicken), Shuanghou, Martin, Varun, Paul, Tiago, Zeno, Beto, Henry, Qingqing, the other Giuseppe, Haohua, Koen, Liesbeth, Jun, Kyle, Wouter, David, Yi, Weibo, Xiaodong and Alexander. I was very lucky to meet also few 'outsiders' like my tennis-mate Greta, Sere and Sara who have enriched my social life in Delft.

I'm also grateful to my former supervisor Prof. Patrick Rambaud, Prof. Jean-Marie Buchlin, Prof. Jeroen van Beeck, dr. Maria Rosaria Vetrano and Philippe Planquart from the Environmental and Applied Fluid Dynamics department at von Karman Institute. They first introduced me to academic research and in particular to experimental fluid dynamics.

I would like to thank all my bros and sis in VKI. In particular Miguel Alfonso Mendez, but also Ale, Alessia, Sara. You have always made me feel good and welcome in Brussel, even if I have left it more than 4 years ago!

I left many friends in Italy to whom I owe my heartfelt thanks. Ste, Vale, Marco, Andre and in particular dr. Berto, you have inspired and supported me in remote for more than 6 years, I own you so much...even if without you I would be more mature!

Finally, I am deeply and forever indebted to my family. This journey would not have been possible without the support of my father Nino, my mother Fatoş, and my sister, Tina. They have always offered me unconditional love and encouragement, giving me freedom to choose what I desired... even when I told them I was going to catch soap bubbles in The Netherlands.

CURRICULUM VITAE

Giuseppe Carlo Alp Caridi was born on August 25, 1985, in Nairobi, Kenya. He graduated with honours in Energy and Nuclear engineering in 2012 at Polytechnic University of Turin, Italy, with a M.Sc. thesis on the topic “Natural convection in an enclosure: comparison between water and Lead-Bismuth Eutectic”. This work was conducted at the von Karman Institute of Fluid Mechanics in Belgium under the supervision of Philippe Planquart, M.Sc., Prof. Jean-Marie Buchlin and Prof. Mario Malandrone. In this framework, Giuseppe developed his great interest in experimental fluid mechanics and in particular in optical measurements techniques.

On September 2012, Giuseppe started the Master after Master at the von Karman Institute in the Environmental and Applied Fluid Dynamics department. Here, he worked on “Characterization of a cavitating flow through optical techniques” in pressure-safety valves under the supervision of Prof. Patrick Rambaud. His thesis received the Excellence in Experimental Research award of the von Karman Institute of the year 2013.

Motivated by his passion on optical measurements techniques and PIV above all, Giuseppe decided to change field of interest from Nuclear into Aerodynamics Engineering. In October 2013, he started his PhD project ‘Development and application of helium-filled soap bubbles’ for large-scale PIV experiments in aerodynamics in the Aerodynamics department of TU Delft under the supervision of Dr. Andrea Sciacchitano and Prof. dr. Fulvio Scarano.

LIST OF PUBLICATIONS

JOURNAL ARTICLES

- Caridi GCA, Ragni D, Sciacchitano A & Scarano F (2016), HFSB-seeding for large-scale tomographic PIV in wind tunnels, *Exp. Fluids* 57: 190
- Caridi GCA, Sciacchitano A & Scarano F (2017), Helium-filled soap bubbles for vortex velocimetry, *Exp. Fluids* 58: 130
- Scarano F, Ghaemi S, Caridi GCA, Bosbach J, Dierksheide U & Sciacchitano A (2015), On the use of helium-filled soap bubbles for large-scale tomographic PIV in wind tunnel experiments, *Exp. Fluids* 56: 42
- Sciacchitano A, Caridi GCA, Scarano F (2015), A quantitative flow visualization technique for on-site sport aerodynamics optimization. *Proced. Eng.* 112: 412-417
- Schneiders JF, Caridi GCA, Sciacchitano A & Scarano F. (2016), Large-scale volumetric pressure from tomographic PTV with HFSB tracers, *Exp. Fluids* 57: 164

CONFERENCE PROCEEDINGS

- Caridi GCA, Ragni D, Sciacchitano A, Scarano F (2015). A seeding system for large-scale Tomographic PIV in aerodynamics, 11th Int. Symp. Particle Image Velocimetry, Santa Barbara, USA
- Caridi GCA, Sciacchitano A (2017), Optical Characterization of HFSB, 12th Int. Symp. on Particle Image Velocimetry, Busan, South Korea
- Scarano F, Ghaemi S, Caridi G, Bosbach J, Dierksheide U, Sciacchitano A (2014), On the use of helium-filled soap bubbles for large-scale Tomographic PIV wind tunnel experiments, 17th Int. Symp. Applications of Laser Techniques to Fluid Mechanics, Lisbon, Portugal
- Morias KLL, Caridi GCA, Sciacchitano A, Scarano F (2016), Statistical Characterization of Helium-Filled Soap Bubbles Tracing Fidelity for PIV, 18th Int. Symp. Applications of Laser Techniques to Fluid Mechanics, Lisbon, Portugal

-
- Rius Vidales, A., Caridi, G., Schneiders, J., Sciacchitano, A., Scarano, F., & Knepper, K. (2016), A large-scale tomographic PTV study of wake flow dynamics on the landing deck of a ship frigate, 11th Int. Conf. on Flow-Induced Vibration and Noise
 - Pinho J, Rambaud P, Chabane S, Buchlin JM, Caridi G (2014), Flow visualization and f-PIV of a two-phase cavitating flow through a safety relief valve at initial subcooling conditions, 17th Int. Symp. on Applications of Laser Techniques to Fluid Mechanics Lisbon, Portugal

